UCLA
UCLA Electronic Theses and Dissertations

Title

Land-atmosphere Interactions and Precipitation Seasonality in the Congo Basin

Permalink

https://escholarship.org/uc/item/5hn0g3vj

Author

Worden, Sarah Rose

Publication Date

2024

Peer reviewed|Thesis/dissertation

eScholarship.org Powered by the California Digital Library
University of California

UNIVERSITY OF CALIFORNIA

Los Angeles

Land-atmosphere Interactions and Precipitation Seasonality in the Congo Basin

A dissertation submitted in partial satisfaction

of the requirements for the degree

Doctor of Philosophy in Atmospheric and Oceanic Sciences

by

Sarah Rose Worden

2024

© Copyright by

Sarah Rose Worden

2024

ABSTRACT OF THE DISSERTATION

Land-atmosphere Interactions and Precipitation Seasonality in the Congo Basin

by

Sarah Worden
Doctor of Philosophy in Atmospheric and Oceanic Sciences
University of California, Los Angeles, 2024
Professor Rong Fu, Chair

Abstract

The Congo Basin contributes a disproportionately large amount to water, carbon, and energy in Africa and globally. However, this region has been least studied among all tropical regions, in part due to a lack of well-constrained data available on the high resolution needed to address their spatial and temporal heterogeneities. We thus cannot yet provide a creditable assessment of changes to the Congo Basin water cycle under the influence of both climate and land cover and land use changes. My dissertation aims at advancing our understanding of land-atmosphere interactions and the mechanisms controlling the rainy season onsets within the basin, both keys towards better assessing its resilience.

I first investigated the sources of moisture in the atmosphere, a necessary condition for rainfall in Chapter 3. I used remotely-sensed water vapor isotopes, in conjunction with a suite of other satellite, in-situ, and reanalysis estimates and isotope mixing model simulations, to disentangle the relative contributions of evapotranspiration (ET) versus advected oceanic

moisture to atmospheric moisture towards rainfall. I reveal that ET provides the most atmospheric moisture throughout the year, and especially for the onset of the spring rainy season. This suggests that the Congo Basin is especially vulnerable to land-use rapid expansion, which can reduce moisture availability and potentially exacerbate climatic drying in that region.

I then evaluated the water fluxes at the interface between the atmosphere and land surface in Chapter 4. My research demonstrated that water vapor isotopes, when normalized to reduce their sensitivity to large-scale changes in atmospheric moisture, co-vary with the water balance, a metric for examining the net flux of moisture into the surface. I show that on basin and sub-basin scales, the Congo Basin displays limited water deficits with insignificant variations over the 21st century, despite observed rainfall variability and other changes to its water cycle. We also confirm high ET on basin and sub-basin scales, thus providing an additional constraint on existing ET model estimates.

Built on the foundation laid in chapters 3 and 4, I next explore the fundamental mechanisms that drive the transition from dry to the rainy season over the Congo basin, a far more complex problem that those in the previous chapters. In Chapter 5, I first focus on the southern Congo Basin with one rainy season in boreal fall. I show that this transition is initiated by a decrease in moisture export towards the Sahel. Then, ET increases due to increases in surface radiation and vegetation photosynthesis. Using water vapor isotopes, I show that ET becomes the main source of atmospheric moisture prior to the start of the rainy season. I additionally show that the African Easterly Jet South and the Congo Air Boundary are key for inducing atmospheric conditions amenable for deep convection. Overall, I show that the rainy season onset is a result of combined large-scale atmospheric circulation changes and vegetation responses to the seasonal change of insolation.

In Chapter 6, I explore the mechanisms of the transition periods to the boreal spring and fall rainy seasons in the equatorial Congo, which is mostly covered by tropical rainforests. I show that the transition to both rainy seasons is initiated by changes in atmospheric moisture transport across its western boundary. While ET contributes the most to atmospheric moisture to rainfall prior to both rainy seasons, it does not change significantly during the transition periods and instead provides background moisture. Generally, thermodynamic conditions indicate an unstable atmosphere, but changes in the level of free convection (LFC) and convective inhibitive energy (CIN) must happen for deep convection to initiate. This is done via increases in boundary layer moisture orographically lifted by the African Easterly Rift, decreasing the LFC and hence CIN. Meanwhile, the African Easterly Jet North and the return branch of the Congo Basin Cell provides shear prior to the spring and fall rainy seasons, respectively. Together, this creates atmospheric conditions favorable for the initiation of deep convection.

Through the above discussed works, I have made an important first step toward a systemic and holistic understanding of the Congo Basin water cycle, setting up future studies of understanding the mechanisms controlling its change and its impacts on the vegetation and nations that lie within, an aspirational goal of my career.

The dissertation of Sarah Rose Worden is approved.

Sharon E. Nicholson

Elsa Marianne Ordway

James David Neelin

Rong Fu, Committee Chair

University of California, Los Angeles

2024

Dedicated to loved ones lost along the way

In loving memory of Benjamin Sapper, Avery Campos, and Annie-Sue Worden

Beloved cousin, friend, and dog

TABLE OF CONTENTS

1 Introduction **1**

1.1 Motivation and Science Questions 1

1.2 Outline 4

2 Methods: Data and Models **8**

2.1 Data 8

2.2 Deuterium Content of Water Vapor 11

2.3 Water Vapor Isotope Models 13

3 Where Does Atmospheric Moisture Come From over the Congo Basin? **15**

3.1 Introduction 15

3.2 Data 18

3.3 Results 20

3.3.1 Comparison of Isotope Observations With Theoretical Mixing and Rayleigh Models 20

3.3.2 The Relative Contributions of ET and Ocean Evaporation to Atmospheric Moisture 23

3.3.3 Interpretation of These Relative Contributions Based on Spatial Patterns . . . 29

3.4 Discussion 32

3.5 Conclusions 34

4 Congo Basin Water Balance and Terrestrial Fluxes Inferred from Satellite Observations of the Isotopic Composition of Water Vapor . . . 37

4.1 Introduction . . . 37

4.2.1 Data Sources . . . 42

4.2.2 Deuterium Content of Water (δD) and dd04 . . . 45

4.2.3 iCAM Model relationships between dd04 and ET-P in the Congo Basin . . . 46

4.3 Results . . . 52

4.3.1 Observationally-Based, Basin-scale Relationships Between dd04 and ET-P . 52

4.3.2 Estimates of ET and ET/P for the Entire Congo Basin . . . 54

4.3.3 Estimating ET-P in Four Quadrants . . . 57

4.3.4 Estimating ET, ET/P, and Q/A in Each Quadrant . . . 58

4.4 Discussion and Conclusions . . . 62

5 On the Mechanisms that Control the Rainy Season Transition Period in the Southern Congo Basin . . . 64

5.1 Introduction . . . 64

5.2 Data . . . 67

5.3 Methods . . . 70

5.3.1 Calculating the Onset of the Fall Rainy Season . . . 70

5.3.2 Thermodynamic and Dynamic Equations . . . 71

5.3.3 Identifying Deep Convection Using OLR . . . 73

5.3.4 Random Forest Feature Importance . . . 74

5.4 Results . . . 75

5.4.1 Pre-Transition 76

5.4.2 Early-transition 79

5.4.3 Late Transition 83

5.5 Discussion 85

5.5.1 Comparing dry-to-rainy season transitions between the Southern Congo and Southern Amazon. 85

5.5.2 Role of Biomass Burning on Affecting Water and Energy Cycles 87

5.6 Conclusion 88

6 On the Mechanisms Controlling the Transition Periods to the Rainy Seasons in the Equatorial Congo Basin 91

6.1 Introduction 91

6.2 Data 93

6.3 Methods 96

6.3.1 Calculating the Onsets and Ends of the Rainy Seasons 96

6.3.2 Thermodynamic and Dynamic Equations 99

6.4 Results 101

6.4.1 Early Transition Period, Spring 102

6.4.2 Late Transition Period, Spring 106

6.4.3 Early Transition Period, Fall 109

6.4.4 Late Transition, Fall 112

6.5 Discussion 115

6.5.1 Comparing the Transition to the Spring vs Fall Rainy Season 115

6.5.2 Comparing the Transition to the Fall Rainy Season in the Equatorial vs Southern Congo 117

6.6 Conclusion 118

7 Conclusions 121

7.1 Summary 121

7.2 Future Directions 124

7.3 Final Remarks 128

A Supplementary Materials for Chapter 4 129

B Supplementary Material for Chapter 5 135

C Supplementary Material for Chapter 6 138

LIST OF FIGURES

3.1 Map of Africa in 2015 showing the different types of vegetation. The central green area is evergreen rainforest, and the boxed area within it is the region used for analysis of the Congo Basin, 15: 30°W and -5: 5°N. Data are taken from the European Space Agency (ESA) Climate Change Initiative (CCI) Land Cover products (Defourny et al., 2017). 16

3.2 Density plot of individual free-tropospheric δD measurements over the Congo Basin in (a) February; (b) August; Blue line is a linear line of best fit. The green and gray solid lines represent mixing models with water originating from land and ocean, respectively, for different initial values of q_0 and q_F ranging between 0.0016–0.0046 and 0.02–0.052, respectively. The dashed green and gray lines represent Rayleigh models with initial values q_0 = 0.0016 and q_s= 0.02. The numbers in the bottom right corner are the fraction of δD above the upper most, land-based mixing model (f). Higher f indicates a relatively greater contribution of evapotranspiration to atmospheric moisture. 22

3.3 Climatology of (a) Free-tropospheric δD (black line), and its standard error (gray shade), as well as Tropical Rainfall Measuring Mission (TRMM) precipitation (gray line) and its standard error (blue shade). (b) Fraction of the δD samples whose values exceed those of a land-based mixing curve (f). Error is calculated assuming ±12 per mil error in δD measurements. All observed data is averaged over the Congo Basin area of study. Gray lines at March and May as well as September and November denote the two rainy seasons (MAM and SON). 24

3.4 (a) Climatology of Tropical Rainfall Measuring Mission (TRMM) precipitation (P), ERA5 integrated moisture flux convergence (MFC), and Fisher-produced evapotranspiration (ET) averaged within the Congo Basin region. Gray shading is the standard error. In general, the standard error for ET and P was too small to show up on the plots. (b) Climatology of ET/P, MFC/P, and f. 26

3.5 (a) Free tropospheric δD (shaded), integrated moisture flux convergence (contours, units of mm/day) in February. The mean standard error of gridded δD was 13.26‰. White boxes denote the absence of δD measurements for that grid box. (b) solar induced fluorescence (SIF) (shaded), precipitation (contours, units of mm/day), and reanalysis winds averaged over 800–875 hPa (vectors, unit: m/s) in February. (c) Same as (a), but for April. The mean standard error of gridded δD was 12.81‰. (d) Same as (b), but for April.. 30

3.6 Same as Figure 5 but for August (top panels) and October (bottom panels). 32

4.1 a) Satellite-based observations of above-ground biomass (AGB) averaged over 2000-2019. The black outline represents the area of the Congo Basin, and the dashed lines divide the basin into four subbasin quadrants: $\mathrm{Quad_{NW}}$, $\mathrm{Quad_{NE}}$, $\mathrm{Quad_{SW}}$, and $\mathrm{Quad_{SE}}$; b)-d) Seasonal precipitation averaged over 2003-2018 for the four quadrants. The different quadrants are separated by a vertical dashed line at 23°E and a horizontal dashed line at 2°S. Error is the standard error of the mean. 38

4.2 Linear regression of the iCAM dd04 estimates (after projecting through the AIRS observation operator) and the iCAM ET-P on a basin scale; b)-d): Multi-year, seasonal cycle, and inter-annual variations (IAVs) of model estimates of ET-P compared to regression-based ET-P. IAVs have been resampled to a seasonal

resolution to better compare; the monthly resolution and associated RMSE are described in Appendix A. 47

4.3 Multi-year record of iCAM ET-P (black) and regression-estimated ET-P (green) using the basin-scale regression equation for each quadrant: a) $\mathrm{Quad_{NW}}$; b) $\mathrm{Quad_{NE}}$; c) $\mathrm{Quad_{SW}}$; and d) $\mathrm{Quad_{SE}}$. 48

4.4 Seasonality of iCAM ET-P (black) and regression-estimated ET-P (green) using the basin scale regression equation for each quadrant: a) $\mathrm{Quad_{NW}}$; b) $\mathrm{Quad_{NE}}$; c) $\mathrm{Quad_{SW}}$; and d)$\mathrm{Quad_{SE}}$.. 49

4.5 Interannual variations (IAVs) of iCAM ET-P (black) and regression-estimated ET-P (green) using the basin-scale regression equation for each quadrant: a) $\mathrm{Quad_{NW}}$; b) $\mathrm{Quad_{NE}}$; c) $\mathrm{Quad_{SW}}$; and d) $\mathrm{Quad_{SE}}$. 50

4.6 a) Basin-scale linear regression between AIRS dd04 measurements and -Q/A-dS/dt; b) long-term record of our calculated ET-P compared to -Q/A-dS/dt as well as a scatter plot showing the linear relationship between them; c) seasonality of our calculated ET-P compared to -Q/A-dS/dt; and d) interannual variations of our calculated ET-P compared to -Q/A-dS/dt as well as a scatter plot showing the linear relationship between them. 51

4.7 ET-P multi-year record for each quadrant calculated using the basin-scale linear relationship. 56

4.8 ET-P seasonal cycle for each quadrant calculated using the basin-scale linear relationship. 57

4.9 ET-P IAV's for each quadrant calculated using the basin scale linear relationship. . . . 58

5.1 a) Aboveground biomass averaged between 2000-2019 (Xu et al., 2019). Black outline denotes the Congo Basin watershed, while the dashed line denotes the split between the northern and southern Congo; and b) climatological rainfall (calculated using monthly TRMM precipitation) for the northern and southern Congo Basin. Shades represents the standard error of the mean spatially. 66

5.2 Pentad start date of the rainy season for the southern Congo Basin for each year between 2000-2020 (calculated using monthly TRMM precipitation) for the northern and southern Congo Basin. Shades represents the standard error of the mean spatially. 71

5.3 a) Precipitation (P), vertically integrated moisture flux convergence (MFC), and evapotranspiration (ET) b) surface specific humidity and column water vapor (CWV); c) zonal vertically integrated moisture flux (MF) across the western (W) and eastern (E) rough boundaries (Methods); and d) meridional MF across the northern (N) and southern (S) rough boundaries (Methods). All are relative to the RSO (denoted as 'O' in the graph). Negative pentads (5-day averages) indicate times prior to the RSO and positive pentads indicate times after the RSO. Shades represents the standard error of the mean of the different years. Time series have been smoothed using a Savitsky-Golay filter (number of coefficients: 5, polynomial order 2).. 71

5.4: Moisture convergence term ($q\nabla.v$) and moisture transport vectors (qv) for: a-d: 925 hPa; e-h: 850 hPa; and i-l: 700 hPa. "Before" represents 30 days (6 pentads) before the pre-transition period. White shades represent topography above the pressure level at hand. 77

5.5: Surface temperature and 850 hPa horizontal winds. “Before” period is 6 pentads (30 days) before the start of the pre-transition period. 78

5.6: a) Evapotranspiration (ET), rooting-depth soil moisture, and solar-induced fluorescence (SIF); b) Insolation and pristine, clear, and all-sky surface solar radiation downwards; c) burned area and vapor pressure deficit (VPD); d) total, high, mid-high, mid-low, and low cloud area fraction; and e) cloud optical thickness (COT) and aerosol optical depth (AOD) relative to the RSO. Shades represents the standard error of the mean of the different years. Time series have been smoothed using a Savitsky-Golay filter (number of coefficients: 5, polynomial order 2). 78

5.7: Fraction of observed δD above a series of mixing (solid) and Rayleigh (dashed) models. Green indicates land-based water vapor models, while black indicates ocean-based water vapor models. f_{mix} is the fraction of observed δD above the uppermost, land-based mixing model. For a) the pre-transition; b) the early-transition; and c) the late-transition. 80

5.8: a) Surface temperature, surface latent heat flux (SLHF), and surface sensible heat flux (SSHF); b) cloud top temperature (CTT) and cloud top height (CTH); c) convective available potential energy (CAPE) and convective inhibitive energy (CIN), and fraction of $OLR < 240\ W/m^2$; d) equivalent potential temperature (θe); and e) vertical velocity (negative means upward motion) all relative to the RSO. Shades in the time series represents the standard error of the mean of the different years. Time series have been smoothed using a Savitsky-Golay filter (number of coefficients: 5, polynomial order 2). 81

5.9: a) Shaded contours: meridional surface temperature gradient; black contours: 650 hPa zonal wind speeds >6 m/s to show the evolution of the AEJ-N (top contours) and AEJ-S (bottom contours); and b) Shaded contours: zonal wind shear (650-925 hPa); grey contours: moisture divergence (q*DIV $\times 10^8$, units: $1/s$) at 650 hPa. Negative (dashed contours) indicates divergence. 82

5.10: Feature importances of the three predictors used to estimate ET using a random forest model: SSRD, soil moisture, and VPD.. 83

6.1: a) Above-ground biomass averaged between 2000-2019. Black outline denotes the Congo Basin watershed and the dashed lines at 2°S and 2°N represent the boundary of the equatorial region. b) Precipitation climatology for the equatorial region. Shades are the standard error of the mean over the grid cells within the boundary. 91

6.2: Pentad starts of the RSOs and RSEs for the equatorial Congo: a) Spring RSOs; b) Spring RSEs; c) Fall RSOs; d) Fall RSEs 97

6.3: For the transition to the spring RSO: a) Precipitation (P), vertically integrated moisture flux convergence (MFC), and evapotranspiration (ET); b) surface specific humidity and column water vapor (CWV); c) Net MF across the zonal and meridional boundaries (Methods). Positive means convergence, negative means divergence. All are relative to the RSO (denoted as '0' in the graph). Time series are smoothed using a Savitsky-Golay filter. Shades represents the standard error of the mean of the different years. 101

6.4: Moisture transport vectors (q*v) and moisture convergence (shades; positive means convergence) for a-c) average of 925-875 hPa for the “before,” early, and late transition periods; d-f) average of 850-600 hPa for the “before,” early, and late

transition periods. Vectors are scaled up by 2 in order to better visualize the changes in magnitude and direction between periods. White shading in a-c represents areas where the topography is greater than 875 hPa. Moisture transport onto land between 8°S-2°N from the Atlantic Ocean at low levels, a-c), represents the low-level winds (LLWs) described by Pokam et al. (2014). Mainly zonal moisture transport at mid levels between 4°S-4°N represents the AEJ-N. 103

6.5: Near-surface (925 hPa) diabatic heating averaged between 15-30E and 2N-8N, and near-surface (925 hPa) zonal wind (u) averaged between 10-15E and 2S-2N. Shades represents the standard error of the mean of the different years. 104

6.6: Prior to the spring RSO: a) cloud area fraction (CAF) for high, mid-high, mid-low, and low clouds; b) cloud top temperature (CTT) and cloud top height (CTH); c) convective available potential energy (CAPE); and convective inhibitive energy (CIN); d) equivalent potential temperature (θ_e; shades) and saturated equivalent potential temperature (black contours); e) vertical velocity; and f) black contours: 650 hPa zonal wind greater than 6 m/s, denoting the AEJ-N. Shaded contours represent the wind shear (u_{900}-u_{650}). Shades represents the standard error of the mean of the different years. All time series have been smoothed using a Savitsky-Golay filter. . . . 105

6.7: Fraction of observed δD above a series of mixing (solid) and Rayleigh (dashed) models. Green indicates land-based water vapor models, while black indicates ocean-based water vapor models. fmix is the fraction of observed δDabove the uppermost, land-based mixing model. For a) the "before" period (15-11 pentads prior to the spring RSO); b) the early-transition; and c) the late-transition. 106

6.8: Evolution of a) relative humidity (RH) averaged between 950-800 hPa; b) the level of free convection (LFC); c) zonal wind shear between 650 and 925 hPa; and d) $\Delta MSE = MSE_{925\ hPa}$-$MSE_{Sat;\ 750\ hPa}$. All are relative to the spring RSO, averaged between 14-26°E to avoid topography errors in the calculations, and smoothed using the Savitsky-Golay filter. Shades represents the standard error of the mean of the different years. 107

6.9: Relative humidity (shades) and vectors of u and $\omega*10^2$ for a) 10-4 pentads prior to the spring RSO; b) 3-0 pentads prior to the spring RSO. Zonal wind (u) for c) 10-4 pentads prior to the spring RSO; d) 3-0 pentads prior to the spring RSO. White shading denotes the topography of the region. 108

6.10: For the transition to the fall RSO: a) Precipitation (P), vertically integrated moisture flux convergence (MFC), and evapotranspiration (ET); b) surface specific humidity and column water vapor (CWV); c) Net MF across the zonal and meridional boundaries (Methods). Positive means convergence, negative means divergence. All are relative to the RSO (denoted as ‘’0 in the graph). All have been smoothed using a Savitsky-Golay filter. Shades represents the standard error of the mean of the different years. 109

6.11: Moisture transport vectors (q*v) and moisture convergence (shades; positive means convergence) for a-c) average of 925-875 hPa for the “before” (19-15 pentads prior to the fall RSO), early, and late transition periods; d-f) average of 850-800 hPa for the “before,” early, and late transition periods and g-i) averaged of 775-600 for the “before”, early, and late transition periods. Winds have been multiplied by a scale factor of 2. White shades in a-c) mask topography greater than 900 hPa. White shades

in d-f) mask topography greater than 850 hPa. Moisture transport between 5°S and 5°N into (out of) the basin represents the lower (return) branch of the Congo Basin Cell in a-c) (g-i). Area of convergence between 4°S and 8°S in a-c) represents the rough location of the Congo Air Boundary (CAB). Mainly-zonal moisture transport between 6°N-15°N represents the AEJ-N. 111

6.12: Near-surface (925 hPa) zonal temperature gradient: $T_{land}$is averaged between 10°-15°E and 5°S-5°N and $T_{ocean}$is averaged between 5°W-5°E and 5°S-5°N. Blue line shows the near-surface (925 hPa) zonal wind (u) averaged between 10°-15°E and 5°S-5°N. Shades represents the standard error of the mean of the different years. 112

6.13: Prior to the fall RSO: a) cloud area fraction (CAF) for high, mid-high, mid-low, and low clouds; b) cloud top temperature (CTT) and cloud top height (CTH); c) convective available potential energy (CAPE); and convective inhibitive energy (CIN); d) equivalent potential temperature θ_E; shades) and saturated equivalent potential temperature (θ_{e_s}); e) vertical velocity; and f) black contours: 650 hPa zonal wind greater than 6.5 m/s, denoting the AEJ-N. Shaded contours represent the wind shear (u_{900}-u_{650}). Shades represents the standard error of the mean of the different years. All time series have been smoothed using a Savitsky-Golay filter. 113

6.14: Fraction of observed δD above a series of mixing (solid) and Rayleigh (dashed) models. Green indicates land-based water vapor models, while black indicates ocean-based water vapor models. fmix is the fraction of observed δD above the uppermost, land-based mixing model. For a) the pre-transition; b) the early-transition; and c) the late-transition. 114

6.15: Evolution of a) relative humidity averaged between 950-800 hPa; (RH); b) level of free convection (LFC), c) zonal wind shear between 650 and 925 hPa; d) $\Delta MSE = MSE_{925\ hPa}$-$MSE_{Sat;\ 750\ hPa}$. All are prior to the fall rainy season. All are averaged between 14-26E to account for effects of topography in the eastern part of the region. All have been smoothed using a Savitsky-Golay filter. Shades represents the standard error of the mean of the different years. 115

6.16: Relative humidity (shades) and vectors of u and $\omega*10^2$ for a) 9-3 pentads prior to the fall RSO; b) 2-0 pentads prior to the fall RSO. Zonal wind (u) for c) 9-3 pentads prior to the fall RSO; d) 2-0 pentads prior to the fall RSO. White shading denotes the topography of the region. 116

A.1 Basin-scale ET-P IAVs from ICAM. Monthly scale. 130

A.2 Quadrant-Scale ET-P IAVs from ICAM on a monthly scale: a) $Quad_{NW}$; b) $Quad_{NE}$; c) $Quad_{SW}$; and d) $Quad_{SE}$ 131

A.3 Comparison of regression-based ET-P (black line) to ET-P calculated using different ET and P datasets. Shaded blue represents the maximum and minimum ET-P from the different datasets, and dark blue line represents the mean ET-P from the different datasets for: a) basin-scale; b) $Quad_{NW}$; c) $Quad_{NE}$; d)$Quad_{SW}$; and e) $Quad_{SE}$ 132

A.4 Like Figure S3, except for the IAVs instead of the multi-year record for: a) basin-scale; b) $Quad_{NW}$; c) $Quad_{NE}$; d) $Quad_{SW}$; and e) $Quad_{SE}$. 133

A.5 Comparison of regression-based ET (black line) to ET from different datasets. Shaded blue represents the maximum and minimum ET from the different datasets, and dark blue line represents the mean ET from the different datasets. Basin-scale. 134

B.1 Moisture transport and moisture convergence at 650 hPa for a) the "before" period; b) the pre-transition; c) the early-transition, and d) the late transition period.. 136

B.2 Surface specific humidity from ERA5 for a) the pre-transition period; b) the early-transition period; and c) the late-transition period. The sharp diagonal gradient in surface humidity denotes the rough position of the Congo Air Boundary (CAB). 137

C.1 q*u averaged between a) 925-875 hPa across the western boundary; b) 850-600 hPa across the western boundary; c) 925-875 hPa across the eastern boundary; and d) 850-600 hPa across the eastern boundary. Positive values across the western boundary indicates moisture entering the basin; positive values across the eastern boundary indicate moisture leaving the basin. For the transition to the Spring RSO. A Welch's t-test was computed between the "before" and early transition, as well as between the early and late transition period. p values less than 0.05 indicate that the means of the early and late periods are statistically different from that of the before and early periods, respectively. Shades represents the standard error of the mean of the different years. 139

C.2 Land-ocean zonal temperature (black line) gradient of near-surface (925 hPa) temperature: T_{ocean} is averaged between 5°S-5°N and 5°W-5°E. Tland is averaged between 5°S-5N and 10-15°E. Zonal wind (blue line) averaged between 5°S-5°N and 10°-15°E. Shades represents the standard error of the mean of the different years. Prior to the spring RSO. 140

C.3 q*v averaged between a) 925-875 hPa across the northern boundary of the equatorial region; b) 850-600 hPa across the northern boundary; c) 925-875 hPa across the southern boundary of the equatorial region; and d) 850-600 hPa across the southern

boundary. Positive values across the northern boundary indicate moisture leaving the basin; positive values across the southern boundary indicate moisture entering the basin. A Welch's t-test was computed between the "before" and early transition, as well as between the early and late transition period. p values less than 0.05 indicate that the means of the early and late periods are statistically different from that of the before and early periods, respectively. For the transition to the Spring RSO. Shades represents the standard error of the mean of the different years. 141

C.4 Specific humidity at 1000 hPa prior to the fall rainy season during the a) "before," (19-15 pentads prior to the Fall RSO) b) Early, and c) Late transition periods. 142

C.5 q*u averaged between a) 925-875 hPa across the western boundary of the equatorial region; b) 850-800 hPa across the western boundary; c) 775-600 hPa across the western boundary of the equatorial region; d) 925-875 hPa across the eastern boundary; e) 850-800 hPa across the eastern boundary; and f) 775-600 hPa across the eastern boundary. Positive values across the western boundaries indicate moisture entering the basin; positive values across the eastern boundary indicate moisture leaving the basin. For the transition to the Fall RSO. A Welch's t-test was computed between the "before" and early transition, as well as between the early and late transition period. p values less than 0.05 indicate that the means of the early and late periods are statistically different from that of the before and early periods, respectively. 143

LIST OF TABLES

2.1 List of data, their sources, the chapters they are used in, the time resolution used, and the reference. 11

4.1 Basin-scale mean ET and ET/P for the different ET datasets. TRMM P is used to calculate ET/P. 54

4.2 ET, ET/P, and Q/A averaged over time and space for each quadrant. Precipitation comes from TRMM. “Regression-based” indicates measurements calculated using the regression-based ET-P estimates. PT-JPL indicates measurements calculated using ET from Fisher et al. (2008).. 61

ACKNOWLEDGMENTS

Funding:

I thank the following grants and organizations for their financial contributions to the material presented in this dissertation.

National Aeronautics and Space Administration (NASA) Future Investigators in NASA Earth and Space Science and Technology (FINESST) Award #80NSSC20K1654. NASA INCA grant #NNX16AN12G. National Science Foundation grant #1917781. The UCLA Joint Institute for Regional Earth System Science and Engineering (JIFRESSE) summer internship. The Grantham and HideTide foundation for their support of Dr. Sassan Saatchi's research on the global carbon cycle and climate change at UCLA.

Scientific Contributions:

I would like to thank my collaborators and co-authors for their time, energy, and effort in contributing to the work presented in this dissertation. This dissertation was made possible through collaborative efforts in data processing, scientific input, funding acquisition, writing, and editing. Thank you to: Rong Fu, David Neelin, Elsa Ordway, Sharon Nicholson, Sassan Saatchi, Sharon Nicholson, Ulli Seibt, John Worden, Mingjie Shi, Junjie Liu, Anthony Bloom, Sudip Chakraborty, Paul Levine, and Robert Dickenson. I'd like to especially thank my research advisor, Rong Fu, for all the time and effort she has spent on this research and being fundamental to my development as a scientist.

I thank my science friends and organizations for their support during my PhD journey. From my graduate education, I would like to thank the Society for Gender Equity in Geoscience, the Center for Diverse Leadership in Science, and the UCLA Atmospheric and Oceanic Science Chi Epsilon Pi Meteorological Honors Society.

Personal

I would like to thank my family and friends for their unconditional support and understanding as I completed this degree. I'd like to thank my parents Pam and John Worden, brother Matthew Worden, my grandparents Janice and Marshall Karlin, as well as the rest of my extended family. Additionally, thank you to my wonderful fiancé James Hamilton, my friends from all walks of life, and my cats Pocahontas and Aurora. All have been here for me during times of both personal and professional struggles during this degree, and I wouldn't have been able to complete it without them.

VITA

2014-2019: BS in Physics, BA in Music Performance, University of California Los Angeles

2019-2021: MS in Atmospheric and Oceanic Sciences, University of California, Los Angeles

PUBLICATIONS

Worden, S., Fu, R., Chakraborty, S., Liu, J., & Worden, J. (2021). Where does moisture come from over the Congo Basin? Journal of Geophysical Research: Biogeosciences*,* 126, e2020JG006024. https://doi.org/10.1029/2020JG006024

Worden, S., Fu, R., Bloom, A.A., Shi, M., Worden, J., & Levine, P. Congo Basin Atmospheric Water Balance From Satellite Observations of the Isotopic Composition of Water Vapor. *AGU Water Resources*. [In Revision].

Worden, S., and Fu., R. On the Mechanisms Controlling the Rainy Season Transition Period in the Southern Congo Basin. *Climate Dynamics* [In Revision]

Worden, S., and Fu, R. On the Mechanisms Controlling the Rainy Season Transition Periods in the Equatorial Congo Basin [in preparation]

Worden S., Ordway, E., Fu, R., Sassan, S., Bloom, A.A., Levine, P., & Smith, T. Five Key Factors Affecting the Equatorial African Carbon Cycle in the 21st century. [in preparation]

Worden S., Saatchi S. Carbon and Water Fluxes are Decoupled in the Wet Amazon. [in preparation]

CHAPTER 1

Introduction

1.1 Motivation and Science Questions

The Congo Basin hosts the third largest center of precipitation over global land, contributing about 30% of total rainfall in Africa (Brummett et al., 2009). Rainfall feeds the Congo River, the world's second largest river by discharge volume, and sustains the world's second largest contiguous rainforest and the tropic's largest peatland complex (Dargie et al., 2017, Laraque et al., 2013a). However, understanding of the water cycle within this region is limited, with large uncertainties due to political instability, civil conflicts, and lack of resources and infrastructure for research (e.g. Alsdorf et al., 2016). For example, rainfall stations have declined sharply from thousands of stations in the mid-20th century to a near complete cessation of functioning in the 21st century, with slow rebuilding of services (Washington et al., 2013, Nicholson et al., 2018b, Nicholson et al., 2019). Meterological studies within Africa have thus historically focused on areas within the Sahel, south Africa, and east Africa, with the Congo climate regime being the most understudied in the African continent (Washington et al., 2013). While emerging research has shown that complex interactions between large-scale atmospheric circulation, mesoscale convective processes, and moisture availability from ocean and terrestrial sources control rainfall, these mechanisms are poorly understood (e.g., Nicholson, 2018, Nicholson 2022, Dezfuli, 2017, Pokam Mba et al., 2022).

Therefore, climate models perform poorly in this region, due to a lack of in-situ data to constrain estimates, and model biases in and heavy parameterization of processes controlling rainfall such as moisture flux convergence, complex topography, land use heterogeneity, and

mesoscale convection (Washington et al., 2013, Dosio et al., 2021). These models cannot well capture historical or present-day rainfall patterns, such as observed precipitation trends, rainfall amount, and rainfall distributions (Zebaze et al., 2019, Haensler et al., 2013, Washington et al., 2013, Crowhurst et al., 2020). This hinders confidence in their ability to predict future rainfall, especially as large differences between global and regional climate model rainfall changes exist (Dosio et al., 2021). Global climate models project increases in rainfall amount and rainfall intensity over the equatorial region while regional models project little change to rainfall amount (Dosio et al., 2021, Sonkoué et al., 2018). The IPCC AR6 report thus notes "low confidence" in projected mean rainfall change over the region, with consequences for understanding how climate change will impact vegetation and the nations that lie within (Cabeza et al., 2022).

Therefore, a holistic understanding of the mechanisms controlling rainfall in the Congo Basin is needed to improve process understanding of model representations of its water cycle. Furthermore, the Congo Basin shows variability in its water cycle, such as droughts, increased dry season lengths, and decadal precipitation changes (e.g., Zhou et al., 2014, Saeed et al., 2013, Fung et al., 2005, Nicholson, 2022, Hua et al., 2016; 2018, Jiang et al., 2019). Before we can fully understand the impacts of this variability on the water cycle, we need to fully understand its controls. Currently, disagreements exist in literature as to the relative importance of evapotranspiration versus advected oceanic moisture in contributing to atmospheric moisture for rainfall over the Congo Basin (e.g., Balas et al., 2006, Dai, 2013, Pokam et al., 2014, Dyer et al., 2017, Risi et al., 2013, van der Ent et al., 2010, Sori et al., 2017; 2022). As moisture availability in the lower troposphere is key to rainfall frequency and intensity over the tropics (Bretherton et al., 2004, Holloway and Neelin 2009, Taylor et al., 2018), understanding the sources of moisture for rainfall and moisture fluxes over the Congo Basin is key towards better model projections

and understanding the mechanisms controlling observed rainfall variability. Furthermore, complex interactions between moisture, large-scale atmospheric circulation systems, and mesoscale convective systems have been systematically studied during the rainy seasons, of which a biannual regime exists within the equatorial region (between ~$2°S - 2°N$) and annual regimes exist within the northern and southern parts of the water shed (e.g., Dezfuli, 2017, Nicholson, 2022, Pokam Mba et al., 2022, Cook and Vizy 2022). However, less attention has been paid to the mechanisms controlling the transition periods to these rainy seasons, which is needed to fully understand seasonal rainfall variability within the basin.

Studies typically use reanalysis and satellite-remote sensing estimates in combination with modeling to investigate the Congo Basin water cycle and moisture fluxes (e.g., Weerasinghe et al., 2020, Nicholson et al., 2019b, Risi et al., 2013, van der et al., 201, Sori et al., 2017, 2022), with large uncertainties in these estimates due to lack of in-situ observations (e.g., Weerasinghe et al., 2020, Nicholson et al., 2019b). In regards to atmospheric moisture, satellite remotely-sensed water vapor isotopes, which are well-calibrated (J. Worden et al., 2012), can provide an alternative to distinguish between moisture that comes from plants (transpiration) versus the ocean (evaporation). Since the deuterium (HDO) content of transpired water is relatively unchanged from that of the original source, it is more enriched compared to evaporated water which contains less HDO (e.g., Risi et al., 2013). While atmospheric processes that change the isotopic signal must be considered, such as heavier isotopes preferentially condensing and leaving behind depleted water vapor (Galewsky et al., 2016), these deuterium measurements provide an independent observational constraint on recycling ratios that specifically consider moisture coming from anywhere, including outside of the domain of study (e.g., Worden et al., 2012, Risi et al., 2013).

Therefore, this dissertation highlights the use of remotely-sensed water vapor isotopes in conjunction with other satellite and reanalysis estimates to investigate key questions about sources of atmospheric moisture, moisture fluxes, and the mechanisms controlling the transition periods to the rainy season in the Congo Basin. Specifically, I seek to answer:

1. What is the relative contribution of evapotranspiration versus advected oceanic moisture to atmospheric moisture for rainfall over the Congo Basin?
2. Has observed rainfall variability induced water deficits within the Congo Basin?
3. What are the mechanisms controlling the transition periods to the rainy seasons within the Congo Basin?

1.2 Outline

This dissertation is structured as follows:

Chapter 2 provides an overview for the data and models used in this dissertation in chapters 3, 4, 5, and 6. The first part describes the remotely-sensed data, including precipitation, temperature, specific humidity, water vapor mass mixing ratio, changes in terrestrial water storage, relative humidity, outgoing longwave radiation, cloud top temperature, cloud top height, cloud area fraction, surface solar radiation, aerosol optical depth, insolation, cloud optical thickness, solar induced fluorescence (SIF), burned area, soil moisture, evapotranspiration, and deuterium measurements. We then describe the reanalysis used in this dissertation, including horizontal winds, vertical velocity, vertically integrated moisture flux, vertically integrated moisture flux convergence, divergence, specific humidity, and temperature. We briefly describe the ground-based data used in this dissertation: river discharge from a station in Kinshasa-Brazzaville. The second part describes the water vapor isotope models used in this dissertation, based on S. Worden et al. (2021).

Chapter 3 focuses on the relative contribution of evapotranspiration (ET) versus advected oceanic moisture, within the equatorial African region, as based on S. Worden et al. (2021). Here we use the water vapor isotopes in combination with reanalysis, SIF, and the water vapor isotope models to examine this contribution. We find that SIF, an indicator of photosynthesis, covaries with δD in early rainy seasons, suggesting that ET is an important contributor to atmospheric moisture in both the spring and fall rainy seasons. However, the relative contribution of ET to the free tropospheric moisture varies between the two rainy seasons. Observed δD relative to a range of observationally constrained, isotopic mixing models representative of water vapor coming from land suggests that $83 \pm 9\%$ of the free tropospheric moisture come from ET in February, and $45 \pm 13\%$ in April, versus $59 \pm 12\%$ in August and 31 ± 12 in October. Reanalysis indicates that this difference between seasons is due to increased advection of ocean air during the fall season, thus reducing the relative contribution of ET to the Congo Basin in the fall. In addition, ET is the primary atmospheric moisture source in the winter and summer dry seasons, consistent with estimates reported in literature. Our results highlight the importance of ET from the Congo rainforest as an important source of moisture for initiating the rainy seasons.

Chapter 4 focuses on using water vapor isotopes in combination with water balance estimates to calculate ET-P and ET on both basin and sub-basin scales to provide new insights into the water balance of the region, as based on S. Worden et al. 2024 (in revision). Our findings show that atmospheric water deficits (ET-P>0) are largest and occur most frequently in four quadrants of the Congo Basin between 2003-2007, but decline thereafter. By differencing our new water balance estimates with gravity-based terrestrial water storage changes and precipitation observations, we confirm that (1) ET is the largest moisture source in the Congo Basin (temporally and spatially averaged ET/P > 70%) and (2) river outflow is largest in the

Western Congo, corresponding to more rivers and higher flow rates. Our results confirm the importance of ET in modulating the Congo water cycle relative to other water sources. Moreover, a stable water balance (no trends) during this time is consistent with contemporaneous observed increases in Congo biomass and suggest limited sensitivity of the coupling between Congo water and carbon cycles to climate-induced water variability.

Chapter 5 focuses on the mechanisms controlling the transition period to the rainy season in the southern Congo Basin watershed as based on Worden and Fu 2024a (in revision). We show that the transition from the dry to the rainy season over the southern Congo is initiated by a decrease in moisture export towards the Sahel, about three to four months before the rainy season onset (RSO), referred to as the pre-transition period. During this period, ET is low due to low surface solar radiation, resulting from low insolation, and high amounts of low-level clouds. In the early transition period one to three months before the RSO, column water vapor and surface specific humidity increase due to increased oceanic moisture. Meanwhile, ET starts increasing for the first time due to increases in surface radiation and vegetation photosynthesis, despite a lack of soil moisture increases. Finally, in the late transition period about one month before the RSO, ET continues to increase, contributing equally to atmospheric moisture needed for deep convection as advected oceanic moisture. Additionally, the formation of the African Easterly-Jet South and the southward movement of the Congo Air Boundary increase vertical wind shear and provide large-scale dynamic lifting of the warm and humid air from the Congo. The frequency of deep convection increases rapidly, leading to the start of the rainy season. Therefore, the RSO over southern-hemispheric Congo basin is a result of combined large-scale atmospheric circulation change and vegetation response to the seasonal change of insolation.

Chapter 6 focuses on the mechanisms controlling the rainy season transition periods in the equatorial Congo Basin, which experiences biannual rainy seasons in boreal spring (starting on average February 25) and fall (starting on average August 19). This is based on Worden and Fu 2024b (in preparation). The spring and fall transition periods both start with an increase in low-level atmospheric moisture from the Atlantic Ocean. While ET contributes the most to atmospheric moisture prior to both the spring and fall transition periods, it does not change significantly and instead provides background moisture. Meanwhile, despite high CAPE and a conditionally unstable atmosphere prior to both rainy seasons, conditions must further change to make atmospheric conditions favorable for deep convection. This is done by increases in low-level zonal moisture transport in the late transition (3 pentads prior to the spring RSO and 9 pentads prior to the fall RSO) that is orographically uplifted by the East African Rift. This lowers the level of free convection and hence connective inhibitive energy prior to both rainy seasons. Meanwhile, the African Easterly Jet North and the return branch of the Congo Basin Cell provide shear prior to the spring and fall rainy seasons, respectively. Therefore, atmospheric conditions become favorable for deep convection and the rainy seasons start.

Chapter 7 closes by revisiting my motivating science questions and summarizing the work presented in this dissertation. I discuss future research directions and long-term goals related to the Congo Basin water cycle. Ultimately, this dissertation increases understanding of the Congo Basin water fluxes and their role in the water cycle, and to my knowledge, provides the first fundamental understanding of the mechanisms controlling the transition periods to its rainy seasons.

CHAPTER 2

Methods: Data and Models

In this chapter, we provide an overview of the data and the water vapor isotope models used in this dissertation. More details can be found in specific chapters where relevant, which is noted in this section.

2.1 Data

A summarization of the data and their sources can be found in Table 2.1.

Data	**Source**	**Chapter**	**Time Resolution Used**	**Reference**
Precipitation	TRMM 3B43, 3B42	3, 4, 5, 6	Monthly, Daily	Huffman et al., 2007
Precipitation	PERSIANN-CDR	4	Monthly	Ashouri et al., 2015
Precipitation	CHIRPS V2.0	4	Monthly	Funk et al., 2015
Precipitation	iCAM v2.0	4	Monthly	Danabasoglu et al., 2020
Evapotranspiration	GLEAM v3.6, v3.7	4, 5, 6	Monthly, Daily	Martens et al., 2017
Evapotranspiration	PT-JPL	3, 4	Monthly	Fisher et al., 2008
Evapotranspiration	MODIS MOD16A3GF_006	4	Yearly	Running et al., 2021
Evapotranspiration	ERA5	4	Monthly	Hersbach et al., 2020
Evapotranspiration	GLDAS v2.1 NOAH025_M	4	Monthly	Beaudoing and Rodell, 2019
Evapotranspiration	iCAM	4	Monthly	Danabasoglu et al., 2020
HDO, H2O	TES v006_Litev01.00	3,5,6	Monthly, Daily	Worden et al., 2012
HDO, H2O	AIRS	4	Monthly	Worden et al., 2019
HDO, H2O	iCAM v2.0	4	Monthly	Danabasoglu et al., 2020

Changes in terrestrial water storage (dS/dt)	GRACE/GRACE-FO (JPL, CSR, GFZ)	4	Monthly	Landerer et al., 2019, Wiese et al., 2019, Watkins et al., 2015, Save et al., 2016, Save et al., 2020, Loomis et al., 2019
River discharge (Q/A)	SO-Hybam	4	Monthly	Burnett et al., 2020
Aboveground Biomass	Xu et al., (2021)	4,5,6	Yearly	Xu et al. (2021)
Column Water Vapor	AIRS	5,6	Daily	Aumann et al., 2019
Atmospheric layer mass mixing ratio	AIRS V7	5,6	Daily	Aumann et al., 2019
Surface mass mixing ratio	AIRS V7	5,6	Daily	Aumann et al., 2019
Surface relative humidity	AIRS V7	5,6	Daily	Aumann et al., 2019
Atmospheric layer temperature	AIRS V7	5,6	Daily	Aumann et al., 2019
Surface Temperature	AIRS V7	5	Daily	Aumann et al., 2019
Outgoing Longwave Radiation	AIRS V7	5	Daily	Aumann et al., 2019
Total Cloud Top Temperature	CERES Syn1deg Ed 4.1	5,6	Daily	Doelling, et al., 2013, Doelling et al., 2016, Su, et al., 2005, Rutan et al., 2015
Total Cloud Top Height	CERES Syn1deg Ed 4.1	5,6	Daily	Doelling, et al., 2013, Doelling et al., 2016, Su, et al., 2005, Rutan et al., 2015
Cloud Area Fraction (Total,	CERES Syn1deg Ed 4.1	5,6	Daily	Doelling, et al., 2013, Doelling et al., 2016, Su, et

High Mid-high, Mid-low, Low)				al., 2005, Rutan et al., 2015
Surface Solar Radiation Downwards (All sky, clear sky, pristine sky)	CERES Syn1deg Ed 4.1	5	Daily	Doelling, et al., 2013, Doelling et al., 2016, Su, et al., 2005, Rutan et al., 2015
Insolation	CERES Syn1deg Ed 4.1	5	Daily	Doelling, et al., 2013, Doelling et al., 2016, Su, et al., 2005, Rutan et al., 2015
Aerosol Optical Depth	MODIS MOD08_D3_6_1	5	Daily	Chu et al., 2002, Wan 2008, Platnick et al., 2016
Cloud Optical Thickness	MODIS MYD08_D3_6_1	5	Daily	Meyer et al., 2015
Continuous Solar Induced Fluorescence	OCO-2	5	Daily	Zhang et al., 2018
Solar Induced Fluorescence	GOME-2 V26 740 nm	3	Monthly	Joiner et al., 2013
Burned Area	GFED 4.1	5	Daily	Randerson et al., 2018, Giglio et al., 2013
Rooting-depth soil moisture	GLEAM 3.7	5	Daily	Martens et al., 2017
Zonal Winds	ERA5	3,5,6	Daily	Hersbach et al., 2020
Meridional Winds	ERA5	3,5,6	Daily	Hersbach et al., 2020
Vertical Velocity	ERA5	5,6	Daily	Hersbach et al., 2020
Vertically Integrated Moisture Flux Convergence	ERA5	3, 5,6	Daily	Hersbach et al., 2020
Vertical integral of eastward water vapour flux	ERA5	5,6	Daily	Hersbach et al., 2020

Vertical integral of northward water vapour flux	ERA5	5, 6	Daily	Hersbach et al., 2020
Divergence	ERA5	5,6	Daily	Hersbach et al., 2020
Specific Humidity	ERA5	5,6	Daily	Hersbach et al., 2020
Temperature	ERA5	6	Daily	Hersbach et al., 2020

Table 2.1: List of data, their sources, the chapters they are used in, the time resolution used, and the reference.

2.2 Deuterium Content of Water Vapor

The deuterium content of water is expressed as the relative ratio of the number of HDO molecules to the total number of H_2O molecules in parts per thousand (‰) relative to the isotopic composition of ocean water as shown below:

$$\delta D = 1000 \times \left(\frac{R - R_{std}}{R_{std}}\right) \qquad \text{Eq 2.1}$$

where R is the ratio of the number of HDO molecules to the total number of H_2O molecules and R_{std} is the corresponding ratio in a reference standard, taken here to be the Vienna Standard Mean Ocean Water: $R_{std} = 3.11 \times 10^{-4}$ (e.g., Wright et al., 2017 and references therein). The isotopic composition of water vapor in the free troposphere is due to a mixture of air parcels originating from different sources (Galewsky, 2018; Galewsky & Hurley, 2010; Galewsky et al., 2016).

Chapters 3, 5, and 6 uses free-tropospheric δD measurements from the National Aeronautics and Space Agency (NASA) Aura Tropospheric Emission Spectrometer (TES) satellite instrument. The analysis period of these measurements is 2005–2011 when the quality of TES δD data are suitable for our analysis. We use the monthly mean TES version 6 (v006_Litev01.00) Level 2 volume mixing ratios of δD in this study. The following quality flags

were used when retrieving the data from the TES satellite: “Species Retrieval Quality = 1,” “Degrees of Freedom for Signal > 1,” and “Average Cloud Optical Depth < 0.4” in order to ensure good quality data as suggested by Worden et al. (2012). The accuracy of these data is ~6 per mil with a precision of 20 per mil (Worden et al., 2012) for the vertical range used in this analysis (~900–420 hPa, or about 1–6 km above sea level). We use the average δD over this vertical range.

Chapter 4 uses free-tropospheric δD measurements of single pixel tropospheric retrievals of HDO and H_2O between 230-912 hPa from the Atmospheric Infrared Sounder (AIRS) radiances using the optimal estimation. We use AIRS data in this chapter instead of those from the Tropospheric Emission Spectrometer (J. Worden et al., 2007) due to its longer record and greater sampling. The AIRS data is bias corrected as suggested by Herman et al. (2021) due to smoothing and systematic errors, as well as instrument noise.

We can use the isotopic composition of an air mass to trace its source to either vegetation or ocean because δD values contributed by ocean evaporation are distinctively different from those by rainforest ET. Rainwater will generally be more isotopically enriched (or heavier) than the source vapor because heavier isotopes preferentially condense (Risi et al., 2020; Tremoy et al., 2014; Worden, et al., 2007). Since the deuterium content of transpired water is relatively unchanged from that of the original source, for example, the isotopically heavier rainwater (Risi et al., 2013), it will be more enriched than the vapor evaporated from its oceanic source. Therefore, by examining the differences in deuterium content of the water vapor over a heavily vegetated surface, one can separate water coming from the ocean from water coming from plants (Wright et al., 2017).

The observed values of free-tropospheric deuterium content also depend on the type of convection. Some form of mixing between the surface and free troposphere is required to transport surface fluxes into the air parcels observed by the satellite. For example, shallower convection detrains near the mid-troposphere, enriching δD of the midtropospheric water vapor (Lacour et al., 2018). Deeper convection, while also mixing air between the surface and free troposphere, is associated with other processes beside condensation that affect the isotopic composition of vapor such as rainfall evaporation (Lacour et al., 2018; Worden et al., 2007). The latter is a confounding factor in our conclusions. For example, Nlend et al. (2020), using a back trajectory method, suggests that δD of rainfall is primarily controlled by upstream mesoscale convective systems instead of ET in West-Central Africa. On the other hand, other research such as from Moore et al. (2014) and Bailey et al. (2017) suggest that the free-tropospheric signal is primarily related to moisture convergence and hence the balance between evaporation and precipitation, even during times of deep convection. Our interpretation of the moisture sources is less influenced by these uncertainties during the months before and after the peak of each rainy season when deep convection is expected to influence δD.

2.3 Water Vapor Isotope Models

We compare our δD parcels with two water vapor isotope models, a mixing model and a Rayleigh model, to identify which air parcels are likely influenced by land versus ocean (Noone, 2012). A mixing model describes what happens to a mixture of two air masses with different water vapor isotopic compositions:

$$\delta_{mix} = q_0(\delta_0 - \delta_F)\frac{1}{q} + \delta_F \quad \text{Eq 2.2}$$

where q_0 and δ_0 are the specific humidity and its δD value of the dry air mass in the upper troposphere, and q_f and δ_f are the specific humidity and δD value of the air mass at the

surface. $q = q_0 + q_f$ is the specific humidity of the mixed air mass between dry air mass in the upper troposphere and humid air mass from its surface source (Noone, 2012). This model considers two possible moisture sources for the air mass sampled by TES δD measurements: air with water vapor transpired from the rainforest, and air with water vapor evaporated from the ocean. Generally, the isotopic composition of vapor sourced from vegetation over the tropical land (δD for vapor from ET) is between -75 ‰ and 0 ‰ while the isotopic composition of vapor sourced from the ocean (δ_F for vapor from ocean) is lower than -75 ‰ (Risi et al., 2013).

We also examine the observed δD values in relation to a Rayleigh model, which describes the change of δD with water vapor mixing rate as liquid water evaporates in equilibrium with temperature:

$$\delta_{ray} \cong (\alpha - 1) \ln\left(\frac{q}{q_0}\right) + \delta_0 \quad \text{Eq 2.3}$$

where α is set to equal the temperature-dependent equilibrium fractionation factor between liquid and water vapor (Majoube, 1971). Under the Rayleigh distillation model, as an air mass moves upward (or toward cooler conditions), condensate is completely removed immediately after it forms under the assumption of pseudo adiabatic process (Galewsky & Hurley, 2010; Wright et al., 2017). During deep convection, air parcel moisture is more isotopically depleted than expected from Rayleigh models because of a combination of processes that occur during convection such as rainfall evaporation and entrainment of isotopically depleted air (Worden et al., 2007).

CHAPTER 3

Where Does Atmospheric Moisture Come From over the Congo Basin?

3.1 Introduction

The Congo Basin, located in the equatorial Africa, hosts the world's second largest, contiguous rainforests (Figure 3.1). While its annual rainfall (1,500–2,500 mm) is lower than that of the Amazon (1,800–3,200 mm) (Alsdorf et al., 2016), its rainy seasons in boreal spring (March-April-May, denoted MAM) and boreal fall (September-October-November, denoted SON) limit the dry seasons to about 3–4 months in summer (June-July-August, denoted JJA) and winter (December-January-February, denoted DJF), and thus help to sustain the rainforests (e.g., Staver et al., 2011; Mayer & Khalyani, 2011). These two rainy seasons are associated with the north-south migration of the rain belt over tropical Africa that crosses the Congo Basin (Nicholson & Dezfuli, 2013); however, the complex interactions between large-scale atmospheric circulation, mesoscale convective processes, and moisture availability from ocean and terrestrial sources drive their onset and demise (e.g., Jackson et al., 2009, Pokam et al., 2012, Nicholson and Grist 2003). These mechanisms that control the variability and changes of the rainy seasons over the Congo Basin are thus poorly understood (e.g., Alsdorf et al., 2016), leading to large uncertainties in representing its current and future rainfall in climate models (e.g., James et al., 2018; Washington et al., 2013).

Observations have shown that a decrease of rainfall and reduced terrestrial water storage in the Congo Basin have likely led to a decrease in vegetation greenness as well as widespread water deficits between 2003 and 2012 (e.g., Reager et al., 2016; Samba & Nganga, 2012; Zhou et al., 2014). Furthermore, the boreal summer dry season length has likely increased since the

Figure 3.1: Map of Africa in 2015 showing the different types of vegetation. The central green area is evergreen rainforest, and the boxed area within it is the region used for analysis of the Congo Basin, 15:30°W and −5:5°N. Data are taken from the European Space Agency (ESA) Climate Change Initiative (CCI) Land Cover products (Defourny et al., 2017).

1980s, mainly due to an earlier ending of the spring rainy season (Jiang et al., 2019). Enhanced water stress could subsequently alter the composition and structure of the evergreen rainforests over the Congo Basin, which are already vulnerable to abrupt transitions to savanna ecosystem as annual rainfall over much of the Congo Basin is low relative to other rainforests (Alsdorf et al., 2016; Jiang et al., 2019; Staver et al., 2011). These changes in both rainy seasons and rainforest composition thus highlight the need for understanding the mechanisms that control rainy season variability, especially whether and how reduced and degraded rainforests could affect the rainy seasons over the Congo Basin through a change in the supply of moisture from evapotranspiration (ET), as well as changes in latent and sensible heating. For example, numerical model simulations have shown that deforestation, as well as the alteration of the composition of the Congo rainforest toward more drought resistant species, can lead to decreased

ET, clouds and rainfall (Bell et al., 2015). Understanding the source of moisture for rainfall over Congo Basin should therefore allow us to better project future changes in the water cycle and its interaction with vegetation over the Congo Basin.

Moisture availability in the lower troposphere is central to rainfall frequency and intensity over the tropics in general (e.g., Bretherton et al., 2004; Holloway & Neelin, 2009; Schiro et al., 2018; Sobel et al., 2004), including the Congo region (Taylor et al., 2018). Previous studies have attributed rainfall variability on interannual to interdecadal timescales over the Congo Basin to sea surface temperature anomalies (SSTA) over the tropical Pacific, Atlantic, and Indian oceans through their influences on moisture transport (Balas et al., 2007; Dai, 2013; Diem et al., 2014; Hoerling et al., 2006; Hua et al., 2016; Nicholson & Dezfuli, 2013; Pokam et al., 2014; Tamoffo et al., 2019). Other studies, using methods such as global models or back trajectories, have found large recycling ratios (over 50%) in the Congo Basin, indicating ET is an important source of moisture for the area (e.g., Risi et al., 2013; van der Ent et al., 2010). It is important to distinguish that here we consider the fraction of water vapor in the atmosphere over the Congo Basin originating from land ET anywhere (e.g., Risi et al., 2013; van der Ent et al., 2010; Yoshimura et al., 2004), rather the typical recycling ratio that calculates the fraction of water vapor originating from land ET only within the domain (e.g., Eltahir & Bras, 1996; Trenberth, 1999).

Determining the contributions of free-tropospheric moisture from ocean evaporation versus ET from vegetation in the Congo Basin is therefore key for developing a better understanding of the relative influences on precipitation from external SSTA, internal land vegetation, and land-use changes. However, most recycling rates heavily rely on model or reanalysis to determine the contribution of ET to precipitation (e.g., Risi et al., 2013; van der Ent et al., 2010).

Measurements of the isotopic composition of rainfall and rivers, when combined with reanalysis-based wind fields and satellite observations of rainfall have been shown to be useful for quantifying the sources of precipitation for different regions of Africa. For example, Levin et al. (2009) has used in situ measurements of oxygen 18 ($\delta^{18}O$) and δD from rivers, as well as Tropical Rainfall Measuring Mission (TRMM) precipitation and wind fields, to show that oceanic moisture is the primary source of precipitation for Kenya, while ET is the primary source of precipitation for Ethiopia. However, in situ measurements of isotopes are virtually unavailable over the Congo Basin. Satellite measurements of δD are sensitive to their oceanic versus terrestrial sources over the global tropics and can therefore be used to identify moisture sources and processes controlling atmospheric humidity (e.g., Brown et al., 2008; Risi et al., 2010; Worden et al., 2007). We use such satellite observations of δD, rainfall, and photosynthesis, along with reanalysis to determine the relative importance of the ET versus moisture transport to the Congo Basin atmospheric moisture using an approach similar to Wright et al. (2017). These data therefore allow us to test a hypothesis that ET is the primary moisture source for the Congo Basin rainy seasons.

3.2 Data

Free-tropospheric δD measurements are from the National Aeronautics and Space Agency (NASA) Aura Tropospheric Emission Spectrometer (TES) satellite instrument. The analysis period of this study is 2005–2011 when the quality of TES δD data are suitable for our analysis. We use the monthly mean TES version 6 (v006_Litev01.00) Level 2 volume mixing ratios of δD in this study. The following quality flags were used when retrieving the data from the TES satellite: “Species Retrieval Quality = 1,” “Degrees of Freedom for Signal > 1,” and “Average Cloud Optical Depth < 0.4” in order to ensure good quality data as suggested by

Worden et al. (2012). The accuracy of these data is ~6 per mil with a precision of 20 per mil (Worden et al., 2012) for the vertical range used in this analysis (~900–420 hPa, or about 1–6 km above sea level). For this study, we use the average δD over this vertical range.

Measurements of solar induced fluorescence (SIF) provide a nearly direct estimate of photosynthesis, a prerequisite for transpiration (e.g., Frankenberg et al., 2011). We can therefore use SIF to indicate the occurrence of transpiration, one of the main components of ET. A caveat is that transpiration also depends on plant water use efficiency, vapor pressure deficit, and radiation (e.g., Boese et al., 2017) so that we might not expect a one-to-one relationship between SIF and ET. We use SIF estimates from the GOME-2 V26 740 nm data products (Joiner et al., 2013) as their observational period overlaps with most of the TES record (2007–2011). The precipitation estimates taken from TRMM are from the 3B43 gridded monthly average estimate at a horizontal resolution of 0.25°×0.25°. TRMM precipitation estimates are generated using a combination of microwave and radar sensors on the instrument that are calibrated with gauge data from the Global Precipitation Climatology Center (GPCC) (Huffman et al., 2007).

ET data comes from a combination of reanalysis and the Moderate Resolution Imaging Spectroradiometer (MODIS) as described in Fisher et al. (2009). While there are a variety of choices of ET and precipitation, we are using these data primarily for qualitative comparisons to give an understanding of what is likely known. A full error analysis of ET and precipitation products is beyond the scope of this study, but described in the literature (Fekete et al., 2004; Fisher et al., 2009; Munier & Aires, 2018; Pan et al., 2020; Rauniyar et al., 2017).

We also use the Fifth Generation of the European Center for Medium-Range Weather Forecasts (ECMWF) Reanalysis (ERA5) monthly means of daily means of the longitudinal (u)

wind component, latitudinal (v) wind component, and vertically integrated moisture flux divergence on a 0.25° × 0.25° grid (Hersbach et al., 2020). The reanalysis is a four-dimensional (i.e., space and time) data assimilation product that combines observations with model forecasts to estimate the dynamic and thermodynamic structures of the global atmosphere. Although the quality of reanalysis in general has been open to debate (Dee et al., 2011; Pan et al., 2020; Thorne & Vose, 2010), using this data in conjunction with observation-based data allows us to corroborate information of the moisture source that cannot be directly provided by observations.

3.3 Results

3.3.1 Comparison of Isotope Observations With Theoretical Mixing and Rayleigh Models

We compare observed δD to mixing and rainfall in February and August, the transition months to the boreal spring and fall rainy season, respectively, in Figure 3.2. The solid curves represent mixing models with different initial δD values that originate from land (green) and ocean (gray) and mix with air representative of the upper troposphere (e.g., Samuels-Crow et al., 2014). The initial values of modeled δD (δ_F) were -50 ‰ and -80‰ for land-based and ocean-based models, respectively, chosen based on representative values of δD from land and ocean. We chose this initial condition of −50‰ for a land-based model to ensure that observations above mixing models with this boundary condition originate from a terrestrial source. Furthermore, the uppermost, land-based mixing model is the only model that does not intersect with the ocean-based mixing models. Therefore, any observed δD located above the uppermost land-based mixing line in Figure 3.2 is most likely from ET. Any δD value shown between the land-based and ocean-based mixing lines likely comes from some mixture of the two sources.

We assess if our assumptions for the isotopic mixing models and Rayleigh models significantly affect our estimates of the relative contribution of ET versus moisture transport from ocean to the atmospheric moisture. For example, Risi et al. (2013) suggests that convection and large-scale circulation can influence continental recycling estimates based on these free-tropospheric deuterium data. Our approach for setting the bounding conditions for these models is based on Noone (2012): we first found the range of specific humidities at 421 mb (q_0) and near the surface at 1,000 mb (q_F) in Equations 2 and 3 as observed by TES by (a) finding their mean and standard deviation and (b) choosing 10 values between the standard deviation about the mean and the standard deviation added to the mean. Then, we determined how the fraction of δD above the uppermost, land-based, mixing (solid green) model line (hereby denoted as *f*) changed between February and August for the different values of q_0 and q_F obtained. The mean difference between *f* estimated by these initial values in February and that in August is 0.199 ± 0.005, where the error is the standard deviation. Though there is a chance that the range of our initial values do not capture the true initial values, the small range of uncertainty of the *f* difference suggests that our results are not too sensitive to initial values. Therefore, while we show a range of mixing models in Figure 2, hereafter, we only consider the mixing model with the mean values of observed q_0 and q_F when calculating *f*.

In February (Figure 3.2a), $83\% \pm 9\%$ of the data lies above the upper-most, land-based (solid green) mixing line, indicating that this water vapor largely originated from land and then was transported into the free troposphere. We should consider this fraction to be a lower bound on the amount of ET contributing to the Congo Basin atmospheric moisture because rainfall processes as well as vapor originating from oceans will decrease δD. The density contours of δD further suggests a strong contribution from terrestrial sources, as most of the parcels are

concentrated between ∼−60‰ and −100‰, values well above the mixing and Rayleigh models for the ocean (dark gray lines) but within the ranges of land-based mixing models. Finally, a linear line of best fit shows an increasing trend toward more enriched δD values as specific humidity increases, consistent with a strong contribution from a terrestrial source (e.g., Risi et al., 2013). In August, $59\% \pm 15\%$ of the data lies above the land mixing line (Figure 3.2b), indicating that ET contributes to more than half of the moisture in the atmosphere during the

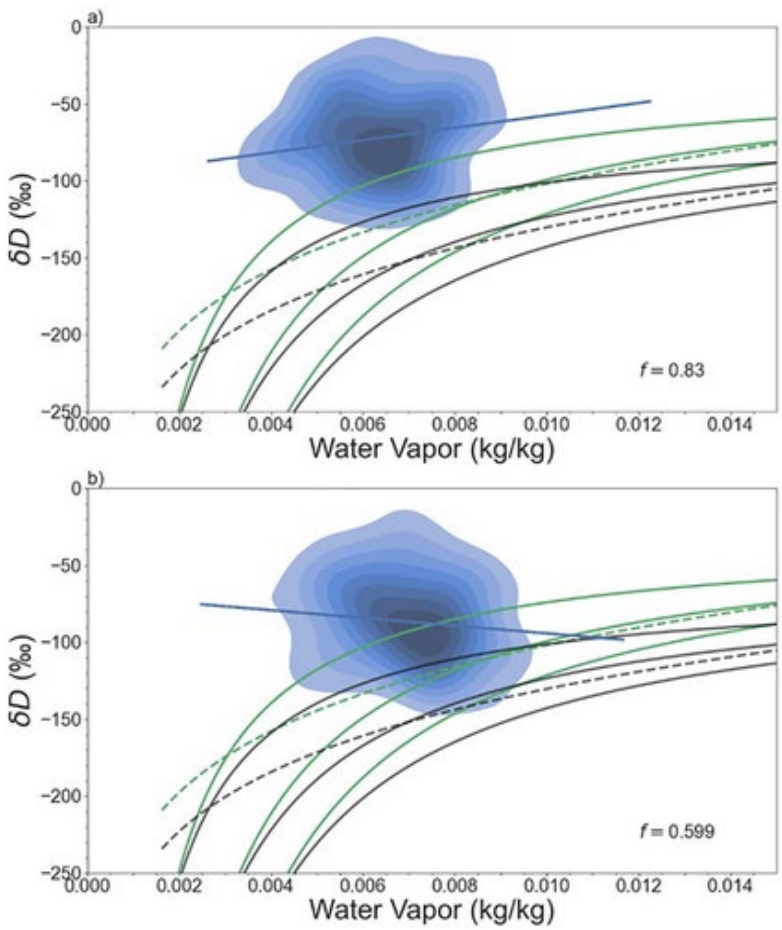

Figure 3.2: Density plot of individual free-tropospheric δD measurements over the Congo Basin in (a) February; (b) August; Blue line is a linear line of best fit. The green and gray solid lines represent mixing models with water originating from land and ocean, respectively, for different initial values of q_0 and q_F ranging between 0.0016–0.0046 and 0.02–0.052, respectively. The dashed green and gray lines represent Rayleigh models with initial values q_0 = 0.0016 and q_s= 0.02. The numbers in the bottom right corner are the fraction of δD above the upper most, land-based mixing model (f). Higher f indicates a relatively greater contribution of evapotranspiration to atmospheric moisture.

transition month to the fall rainy season, though less than that in the spring. The density contours of δD further overlap mixing and Rayleigh models from both ocean and land sources, also suggesting a mixed contribution from terrestrial and oceanic sources. Finally, a linear line of best fit reveals declining δD values with increasing specific humidity, consistent with reduced continental recycling (Risi et al., 2013). While it is challenging to uniquely identify what combination of moisture sources and rainfall and mixing processes affects the observations below the ocean mixing line using this method, Figure 3.2 highlights the change in relative importance of ET and oceanic moisture from transport as moisture sources for the boreal spring and fall rainy seasons in the Congo Basin.

3.3.2 The Relative Contributions of ET and Ocean Evaporation to Atmospheric Moisture

Comparison of the isotopic data to the mixing and Rayleigh models (Figure 3.2) shows that ET likely contributes more moisture in the transition month to the spring rainy season (February) than in the transition month to the fall rainy season (August). To investigate the relative contributions of ET to moisture throughout the year, we examine δD, precipitation, and f the fraction of the observational samples for which δD exceeds the upper-most land-based mixing model (the top solid green line in Figure 3.2) in Figure 3.3.

Precipitation and δD (Figure 3.3a) show opposing trends in general: increased rainfall corresponds with depleted δD values in rainy seasons and vice versa in dry seasons. This could indicate one of three possibilities: (a) condensation plus rainfall evaporation decreases the deuterium content as discussed previously; (b) increased transport of ocean evaporation into the Congo Basin during peak times could deplete δD measurements and signify an increased contribution of ocean evaporation to atmospheric moisture; or (c) some combination of both are

responsible for depleted δD measurements. It is important to note that in the cases of (a) or (c), ET could still have a relatively significant contribution to atmospheric moisture, but precipitation also has a substantial impact on deuterium content.

Compared to the two rainy seasons, the relationship between precipitation and δD is less consistent during the two dry seasons. During the summer dry season, precipitation is generally low, while δD is enriched compared to the rainy seasons, but lower compared to the winter dry

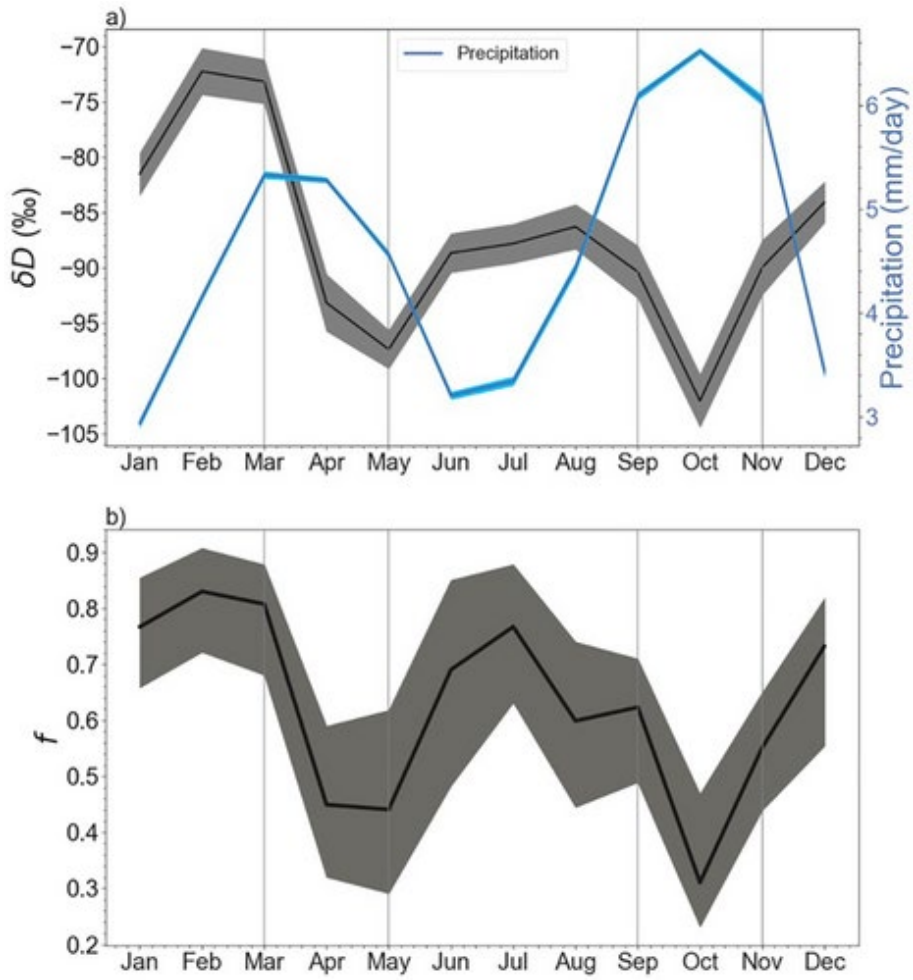

Figure 3.3: Climatology of (a) Free-tropospheric δD (black line), and its standard error (gray shade), as well as Tropical Rainfall Measuring Mission (TRMM) precipitation (gray line) and its standard error (blue shade). (b) Fraction of the δD samples whose values exceed those of a land-based mixing curve (f). Error is calculated assuming ±12 per mil error in δD measurements. All observed data is averaged over the Congo Basin area of study. Gray lines at March and May as well as September and November denote the two rainy seasons (MAM and SON).

season. Because precipitation is lower, this could indicate that rainout has less impact on depleting δD during the summer dry season and instead it is possible that ocean evaporation advected into the region plays a larger role in contributing to moisture in the summer dry season compared to the winter dry season. During the winter dry season, δD is enriched maximally, despite increased precipitation from January to February. This could indicate that ET is the main contributor to moisture for the winter dry season and the onset of the spring rainy season in February.

In general, f follows a similar seasonal pattern to δD in Figure 3.3a: f is higher during the two dry seasons in winter and summer and lower during the two rainy seasons in spring and fall (Figure 3b). Maximum f (0.83 ± 0.09) occurs during February, suggesting that increasing vapor from the land areas with high ET is the main reason for increasing free tropospheric specific humidity (q_0) prior to and during the onset of the spring rainy season. In contrast, f is lower during August (0.59 ± 0.15) than during February, suggesting that increasing advected ocean evaporation contributes to the increasing q_0 during the transition to fall rainy season.

However, throughout the winter and early spring, f remains above ~ 0.6 , meaning that most of the observed δD measurements during those months must come from land. This indicates that ET is the main source of moisture for the dry seasons. As the rainy seasons reach their peaks, f reduces to 0.45 ± 0.13 in mid-spring (April), and 0.31 ± 0.12 in mid-fall (October). Throughout the rainy seasons, f only remains above ~ 0.6 in March and September. As these are the beginning months of the spring and fall rainy season, respectively, these f values indicate that ET is still an important contributor to moisture for the rainy seasons. But, f and δD both decrease in the next couple of months likely due to a combination of (a)

increasing transport from ocean presumably driven by increased latent heating and (b) increasing δD depletion from rainout.

Unfortunately, the δD observations cannot directly quantify the relative contribution of ocean and land sources without further knowledge from other observations. Reanalysis and remotely sensed data, on the other hand, can provide quantitative information on the Congo Basin moisture budget. Due to a lack of observational data, many previous studies have used reanalysis to analyze the moisture sources and dynamics of the Congo Basin. However, monthly reanalysis estimates of tropical precipitation and ET are known to be erroneous due to lack of

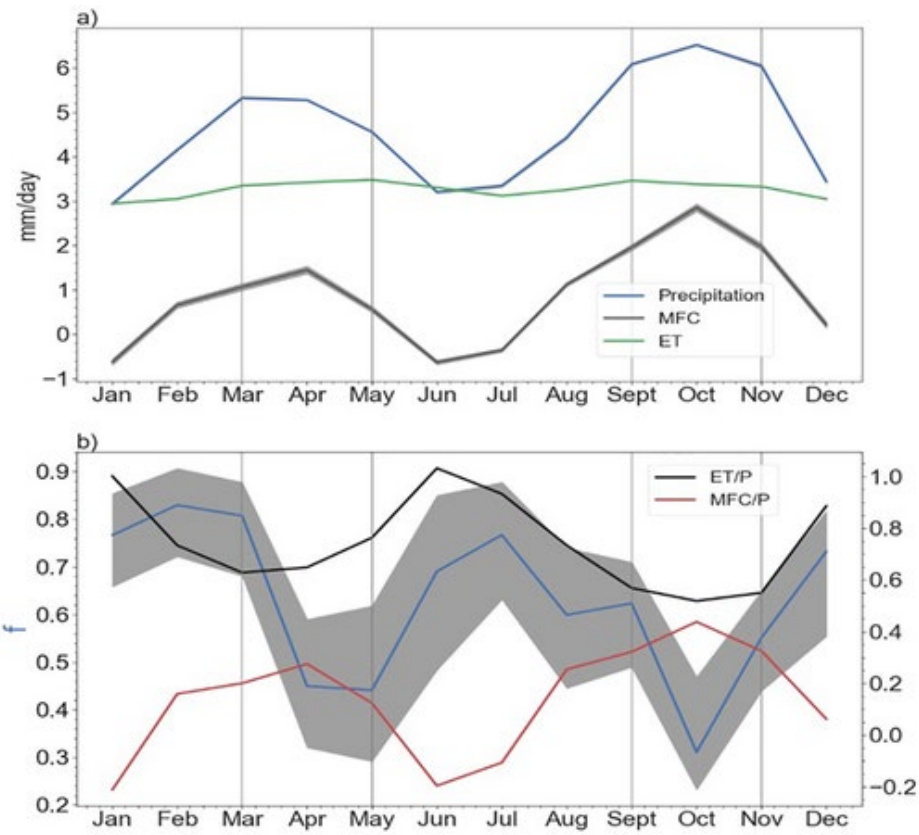

Figure 3.4: (a) Climatology of Tropical Rainfall Measuring Mission (TRMM) precipitation (P), ERA5 integrated moisture flux convergence (MFC), and Fisher-produced evapotranspiration (ET) averaged within the Congo Basin region. Gray shading is the standard error. In general, the standard error for ET and P was too small to show up on the plots. (b) Climatology of ET/P, MFC/P, and f.

observational constraints in tropical Africa (e.g., Fekete et al., 2004; Hua et al., 2019). As we do not have independent data sets to validate the current ET datasets and provide the most accurate ET and precipitation data sets over the Congo for this study, we choose to use moisture flux convergence (MFC) from ERA 5 reanalysis as well as precipitation from TRMM, and ET from a MODIS-based product (Fisher et al., 2009) for the purpose of examining the seasonality of the moisture budget (e.g., Shi et al., 2019). We examine the seasonal cycles of the moisture budget components, as well as calculate the fractional contributions of ET and MFC to precipitation, to compare their relative contributions to precipitation in Figure 3.4.

Figure 3.4a shows that precipitation varies between 3.0 and 5.4 mm/day over the winter-spring period, and between 3.0 and 6.6 mm/day in summer-fall period, respectively. ET from the MODIS-based data set contributes about 3.0 mm/day of the moisture to atmospheric moisture during winter and summer dry seasons and increases slightly to 3.3 mm/day in spring and fall rainy seasons. The net moisture transport generally contributes much less to the atmospheric moisture than ET: from negative (moisture export) 0.5 mm/day in winter to positive (moisture import) 1.5 mm/day in spring, and from negative 0.5 mm/day in summer to positive 2.6 mm/day in fall. Note that there is a general imbalance of 0.5 mm/day between precipitation estimated by TRMM and the sum of ET and net moisture transport estimated by MODIS and ERA5, although their seasonal variations are consistent.

Figure 3.4b shows the contributions of ET and MFC to precipitation within our Congo domain, as indicated by ET/P and MFC/P. ET/P shows consistently high values throughout the year and MFC/P is always lower than that of ET/P (e.g., Burnett et al., 2020; Crowhurst et al., 2020). These data support our conclusion that there is a larger relative contribution of ET

to the moisture for the spring versus fall rainy seasons. We also compare the seasonal cycle of f to that of ET/P (Figure 4b). f represents the fractional ET contribution from both our Congo domain and upstream regions to the free tropospheric moisture within our Congo domain, whereas ET/P represents the local ET contribution to precipitation all within our Congo domain. In addition, f represents a lower bound of the contribution of land to atmospheric water vapor due to choosing a high δD threshold for moisture from land as well as the potential δD depletion from precipitation. However, we believe it is still useful to compare as their common component is ET and ET/P is widely cited in literature as a local precipitation-recycling indicator. The seasonal variations of f and ET/P can be similar during the dry seasons when they are dominated by the change of local ET as moisture transport from ocean and precipitation are moderate. During the peak rainy seasons, variations of f and ET/P are dominated by a significant increase of precipitation and moisture transport from ocean. However, in the early spring rainy season (February-March), the variations of f and ET/P are distinctively different. This could be for a var iety of reasons. For example, it is possible that the difference between f and ET/P originates from scale differences: f is a metric of the relative contribution of ET to atmospheric moisture from anywhere, whereas ET/P represents the fraction of precipitation that originates from ET in the same grid box. ET/P could decrease as the increase in P outpaces the local increase in ET during February-March, but the increase in P could be outpaced by the increase both regional and local ET, as represented by f. Furthermore, the disagreements could be due to the quality of the data. Studies show seasonal ET cycles from models, reanalysis, and other remotely sensed products that vary greatly in their magnitude of seasonality (e.g., Burnett et al., 2020; Crowhurst et al., 2020). The decreased sensitivity of remotely sensed ET during the wet seasons (Fekete et al., 2004; Pan et al., 2020), or the uncertainties of ET estimates based on MODIS in evergreen

tropical rainforests (Paca et al., 2019) could lead to underestimates of the seasonal variations of ET.

3.3.3 Interpretation of These Relative Contributions Based on Spatial Patterns

As discussed previously, the deuterium-based data provides a lower bound estimate on how ET contributes seasonally to atmospheric moisture over the Congo. In this section, we discuss additional evidence based on analysis of moisture flux convergence and winds as well as satellite-based photosynthesis measurements. To examine the role of winds in bringing in moisture to the region, we investigate the spatial patterns of moisture flux convergence (MFC), precipitation, 800–875 hPa averaged wind, δD, and SIF over the Congo Basin for the following months: (a) during the transition month (February) to the spring rainy season, and the peak month of the spring rainy season (April) and (b) during the transition month (August) to the fall rainy season the peak month of the fall rainy season (October).

Figure 3.5a shows that in February, enriched δD ($\delta D > -75‰$) is concentrated within the Congo Basin, with the exception of enriched values to the northeast where high mountainous ranges penetrate further into the atmospheric boundary layer and push high δD values from the atmospheric boundary layer into the free troposphere. δD is highest in the middle and east of the Congo Basin ($20° - 30°E$), corresponding with relatively high SIF and rainfall (Figure 3.5b). This covariation of δD values and SIF indicates that transpiration is one of the main components of ET contributing to atmospheric moisture during this time as photosynthesis co-varies with transpiration (e.g., Boese et al., 2017 and references therein). The increase of rainfall does not contribute to the increase of δD, as it would preferentially remove δD in the atmosphere. The

covariance between SIF and rainfall suggests that vegetation photosynthesis also increases with an increase of rainfall.

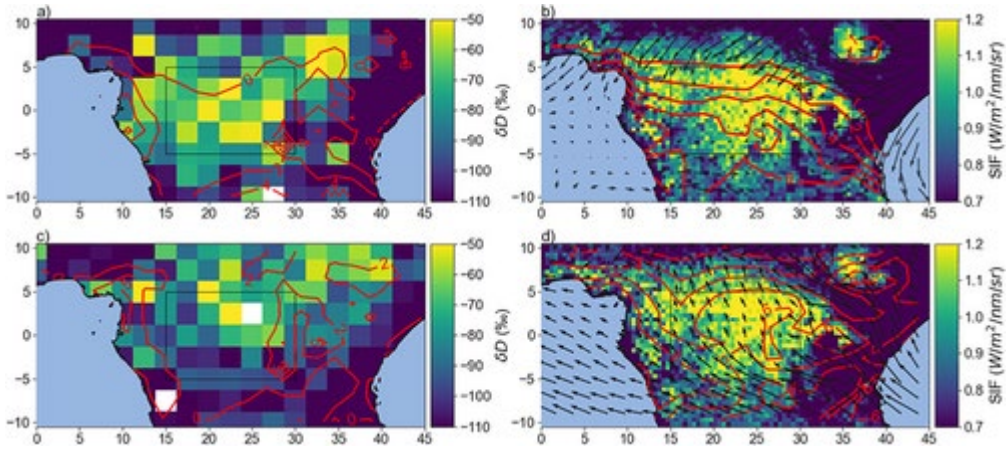

Figure 3.5: (a) Free tropospheric δD (shaded), integrated moisture flux convergence (contours, units of mm/day) in February. The mean standard error of gridded δD was 13.26‰. White boxes denote the absence of δD measurements for that grid box. (b) solar induced fluorescence (SIF) (shaded), precipitation (contours, units of mm/day), and reanalysis winds averaged over 800–875 hPa (vectors, unit: m/s) in February. (c) Same as (a), but for April. The mean standard error of gridded δD was 12.81‰. (d) Same as (b), but for April.

Furthermore, no winds from either the Atlantic Ocean or Indian Ocean bring depleted δD into the Congo Basin (Figure 3.5b), and there is little moisture flux convergence the basin (Figure 5a). These conditions all point toward ET being the primary source of moisture in the spring rainy season, generally consistent with Sorí et al. (2017). While March δD values (not shown) remain similar to its distribution in February, δD values in April (Figure 3.5c), the peak of the boreal spring rainy season, show that enriched δD values occur mostly in the northern part of the basin, which corresponds with relatively higher SIF. However, in general, δD is more depleted than in February. This is likely due to a combination of (a) winds bringing in moisture from the Indian Ocean and (b) the rainout process as described in Section 3, as indicated by high rainfall within a larger portion of the basin. This does not necessarily mean that the contribution of ET to atmospheric moisture decreases, only that its relative contribution drops as moisture

from the ocean or the monsoon region increases. Overall, Figure 3.5 shows enriched δD, high corresponding SIF, and lack of moisture transport by winds, in February, indicating that ET is the main moisture contributor for the transition to spring rainy season, while in April, the presence of winds from the Indian Ocean combined with depleted δD indicate a higher relative contribution of advected ocean evaporation.

In August (Figure 3.6a), one month prior to the boreal fall rainy season, δD values are more depleted than in February, with the majority of observations ranging from ~ -100 ‰ to -70 ‰. Enriched δD values in the southern part of the basin correspond with relatively high SIF. While the highest SIF is located in the northern part of the basin, δD values there are depleted likely because winds carry moisture from the Atlantic Ocean into that part of the region, which mixes with the enriched δD from plants. In October, during the peak of the boreal fall rainy season (Figure 3.6d), highest SIF concentrates in the eastern part of the basin, mostly likely as a result of increased precipitation. Since Figure 3.6d indicates a lack of low-level westerlies reaching the Congo Basin from the Atlantic, moisture is most likely brought in by strong meridional flow related to the African Easterly Jet (AEJ) from areas with mesoscale convective systems (Cook & Vizy, 2016; Pokam et al., 2012). These winds bring depleted δD to the Congo Basin (Figure 3.6c), which partially offsets the positive influence of ET on δD. Rainfall processes also likely decrease δD compared to δD in August. Overall, in Figure 3.6, depleted δD values (compared to February) spatially correspond to moisture transport from the Atlantic Ocean in August, while rainout and possible moisture brought in by the AEJ deplete δD over the entire Congo Basin in October.

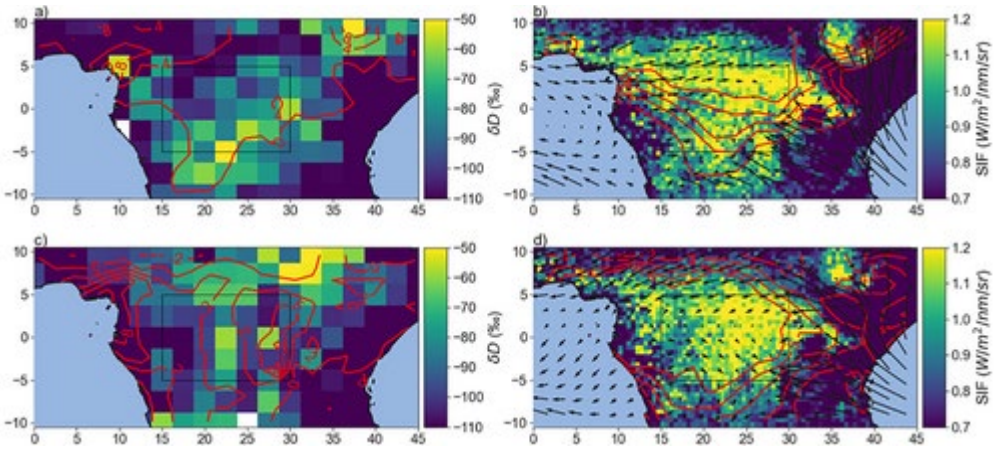

Figure 3.6: Same as Figure 5 but for August (top panels) and October (bottom panels).

3.4 Discussion

Recycling ratios from previous studies indicate significant contributions of ET (greater than 50%) to atmospheric moisture throughout the year (e.g., Nicholson et al., 1997; Risi et al., 2013); however, while it is desirable to compare our assessment of the role of ET in contributing to atmospheric moisture to that suggested by previous studies that calculate continental recycling ratios, a direct comparison is not currently feasible. This is because the recycling rate in literature is mostly defined either as the fractional contribution of ET to precipitation or by local ET versus moisture advected from outside regions, whereas δD is linked to the ratio of water vapor from ET to the total water vapor in the atmosphere (Risi et al., 2013). In addition, δD is influenced by ET both locally and along the path of the air mass, including ET from areas outside the Congo Basin when wind, and thus moisture advection, is strong. Therefore, we can only compare previous studies that quantify the ET contribution to water vapor considered from regions both inside and outside the Congo Basin domain (e.g., Risi et al., 2013; van der Ent et al., 2010; Yoshimura et al., 2004). For example, Risi et al. (2013) used a combined δD observations by TES and a water vapor tagging approach in a climate model. Their result suggests that ET provides more than half of the atmospheric moisture (about 65%) in

the winter and summer dry seasons in the Congo region. Our estimates are qualitatively consistent with their result for these two dry seasons, although they suggest that the ET contribution could be somewhat higher than their model values based on comparison with the TES data. Furthermore, Pokam et al. (2012) suggests that ET influences spring rainy season changes more than fall rainy season changes. Our results clarify that this stronger influence in spring is likely because ET is the primary source of atmospheric moisture during the spring rainy season; therefore, changes in ET likely impact rainfall in spring.

Is it possible that the relatively higher ET contribution to atmospheric moisture for spring versus fall is not just due to increased contribution from advected ocean evaporation to atmospheric moisture for the fall rainy season? Previous studies have found a higher ET contribution to the moisture budget during the spring rainy season compared to that of the fall rainy season, which could also help explain why ET contributes more moisture for the spring rainy season. On the other hand, Burnett et al. (2020) calculated basin-scale ET in the Congo using water-balance methods, positing that increased radiation, as well as the availability of soil moisture, can explain increased ET in the spring: Higher direct photosynthetically active radiation (PAR) fractions combined with higher net solar radiation increase water use efficiency, while increased terrestrial water storage increases the amount of water available for transpiration. Crowhurst et al. (2020), using global climate models, also calculated ET over a similar domain and found that it was higher in the spring rainy seasons compared to the fall rainy season. They attributed changes in leaf area index and vapor pressure deficit to changes in transpiration between the spring and fall rainy season.

How does the relative contribution of ET to atmospheric moisture over Congo Basin compare to that over the Amazon basin? δD values are on average more enriched over the Congo Basin than over the Amazon rainforest. In the Congo Basin, δD values are on average $-88‰$ annually, $-87‰$ during the boreal spring rainy season, and the summer dry season, $-94‰$ during the boreal fall rainy season, and $-79‰$ during the boreal winter dry season (Figure 3a). In contrast, δD values over the Amazon are on average $-130‰$ annually, $-139‰$ during the wet season (October-May), and $-126‰$ during the dry season (June-September). These differences are broadly consistent with a higher recycling rate in the Congo than in the Amazon as suggested by some studies (e.g., Nicholson et al., 1997; Risi et al., 2013). The recycling rate over the Amazon ranges from about 30% (e.g., Staal et al., 2018) based on reanalysis data to about 50% (Salati et al., 1979) based on isotopic composition of the stream flows. A higher ET contribution to atmospheric moisture in the Congo Basin versus the Amazon basin, as suggested by δD data, is also qualitatively consistent with the ET estimated from water balances using rainfall and runoff data. The annual ET is estimated to contribute to 75%–85% of the annual rainfall in Congo Basin versus 50%–62% in the Amazon basin (Alsdorf et al., 2016; Fernandes et al., 2008; Molion, 1975). Therefore, ET is central in determining the climate variability and change of the water cycle in Congo Basin which has a rainfall regime drier than the Amazon. Our results imply that the loss of rainforests due to land use, biomass burning, and climatic drying in Congo (Bell et al., 2015; Staal et al., 2016) will likely have a greater impact on rainfall in the Congo than in the Amazon basin, especially for the spring rainy season.

3.5 Conclusions

Most previous studies of the Congo Basin rainy seasons have focused on clarifying the impacts of moisture transport from oceans on rainfall variability and changes. In contrast, the

role of vegetation and its modulation from land-use and deforestation have been far less clear due to lack of adequate observations. Using a suite of satellite measurements, including the deuterium content of water vapor and SIF, we show that plant-transpired water, lifted into the free troposphere, is a primary moisture source for the atmosphere during boreal winter (DJF) and summer (JJA). However, both moisture advected from oceans and water transpired from the Congo rainforests are important moisture sources during the rainy seasons (March-May and September-November).

Specifically, the climatology of δD points toward ET being the main initial contributor to atmospheric moisture during February, the transition month to the spring rainy season but less so in August, the transition month to the fall rainy season. *f*, the fraction of the observational samples for which δD exceeds that of the uppermost land-based mixing model line (Figure 3.2), is $83\% \pm 9\%$ in February versus $59\% \pm 15\%$ of total water vapor samples in the Congo domain in August. Enriched δD in February corresponds with relatively high SIF and a lack of winds bringing moisture in from the Atlantic Ocean, while relatively depleted δD in August is due to winds bringing in moisture from the Atlantic Ocean and mixing with the enriched δD from areas with high SIF within the Congo Basin. As the rainy season reaches its peak in both spring and fall, δD decreases and the fraction of the observed water vapor samples most likely from ET reduces to $45\% \pm 13\%$ in April and $31\% \pm 12\%$ in October as expected from deep convection and precipitation, and increased moisture transport from the ocean. In general, the climatological seasonal cycles of ET, precipitation and moisture flux convergence (MFC) derived from satellite observations and reanalysis are consistent with the δD results in that both show a higher ET contribution to atmospheric moisture during dry seasons than during

the wet seasons. However, neither of these estimates of ET can capture the high ET contribution in the winter/early spring as shown by the δD data.

Our results imply the need to evaluate the possible change of photosynthesis and ET seasonality as a potential contributor to changes to the spring rainy season, in addition to other potential external forcings, such as SSTA, and changes to moisture transport and the African Easterly Jet. For example, observations have shown an earlier than normal onset and demise of the spring rainy season (Jiang et al., 2019; Taylor et al., 2018) over this region due to increased rainfall in February and decreased rainfall in May-June. Furthermore, our results raise several questions: Would the spring rainy season disappear or substantially weaken if ET were substantially reduced by rainforest loss? Are the mechanisms for the onset of spring rainy season significantly different from those of the fall rainy season? What roles do shallow convection versus lower tropospheric circulation play in lifting plant transpired water vapor from the surface to the free troposphere? Why does ET contribute more to the atmospheric moisture in the Congo than in the Amazon basin? Further study is needed to better elucidate these different mechanisms and discover how they might change with climate and land use.

CHAPTER 4

Congo Basin Water Balance and Terrestrial Fluxes Inferred from Satellite Observations of the Isotopic Composition of Water Vapor

4.1 Introduction

The Congo Basin, home to the world's second largest tropical rainforest and river by discharge volume, as well as the largest peatland complex in the tropics, is a crucial region for the Earth's water and carbon cycles (e.g., Alsdorf et al., 2016, Dargie et al., 2017). The basin accounts for approximately 30% of Africa's total rainfall and nearly half of its freshwater discharge to the Atlantic Ocean (e.g., Brummett et al., 2009, Laraque et al., 2013a, N'kaya et al., 2022). Previous studies have documented decadal changes in rainfall, changes in its rainy season onsets and length, and declines in terrestrial water storage within the basin since the beginning of the 21st century (e.g., Zhou et al., 2014, Jiang et al., 2019, Nicholson et al., 2022). As carbon and water cycles in the tropics are tightly coupled (e.g., Green et al., 2017, Gentine et al., 2019), these changes to the water cycle can have significant effects on vegetation in the Congo Basin (e.g., Zhou et al., 2014, Saeed et al., 2013, Fung et al., 2005). The difference between evapotranspiration minus precipitation ($ET - P$) , provides a measure of the net water flux leaving the soil to the atmosphere (e.g., Fung et al., 2005, Feng et al., 2015, Shi et al., 2022). Consequently, $ET - P$ estimates are directly sensitive to the coupling between the atmosphere and terrestrial vegetation (e.g., Dong et al., 2020, Guan et al., 2015, Davis et al., 2019, Hakamada et al., 2020) with positive values ($ET - P > 0$) indicating soil moisture deficits and subsequent plant stress (e.g. Aragão et al. 2007, Guan et al. 2015; Zemp et al. 2017; Tao et al. 2022).

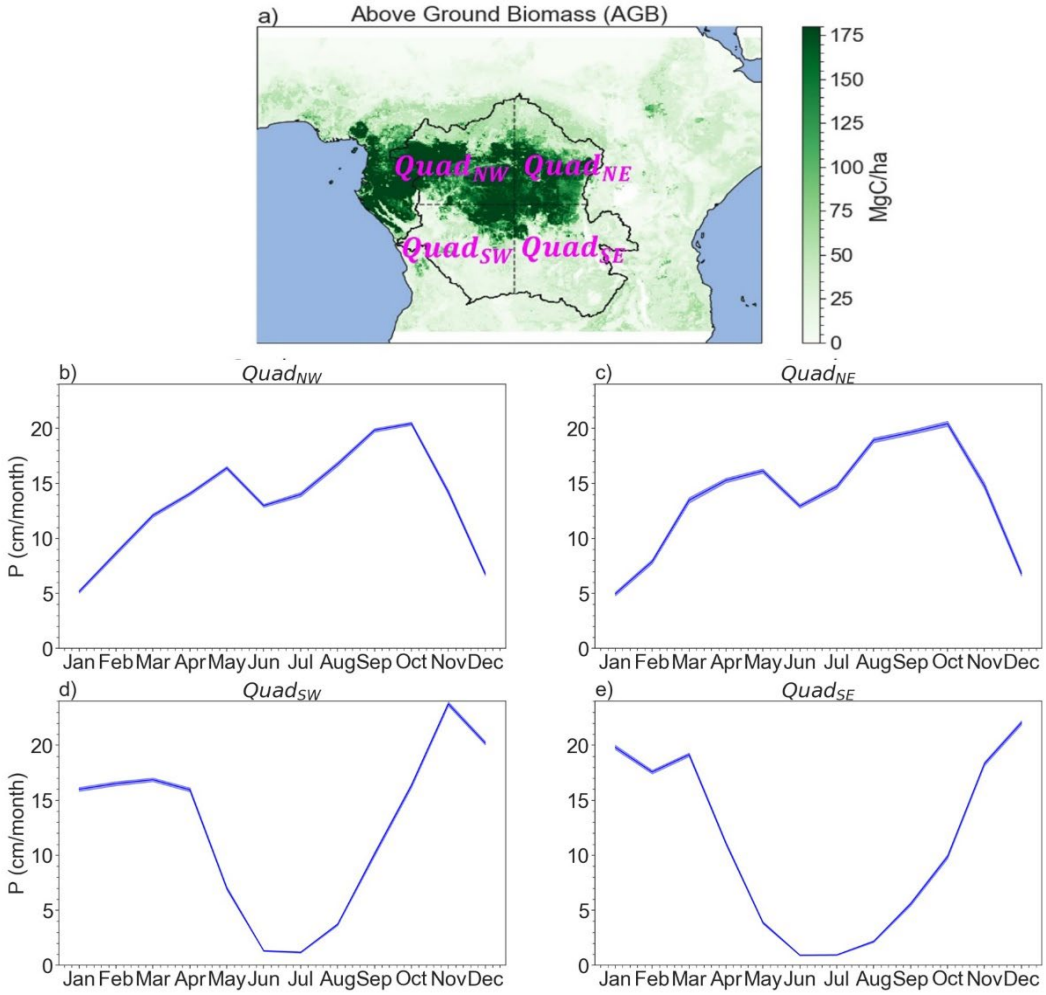

Figure 4.1: a) Satellite-based observations of above-ground biomass (AGB) averaged over 2000-2019. The black outline represents the area of the Congo Basin, and the dashed lines divide the basin into four subbasin quadrants: $Quad_{NW}, Quad_{NE}, Quad_{SW}, and\ Quad_{SE}$; b)-d) Seasonal precipitation averaged over 2003-2018 for the four quadrants. The different quadrants are separated by a vertical dashed line at $23°E$ and a horizontal dashed line at $2°S$. Error is the standard error of the mean.

However, dataset uncertainties and sampling remain a challenge for accurately closing the Congo terrestrial water balance and its corresponding fluxes (e.g., Azarderakhsh et al., 2011, Sheffield et al., 2009, Moreira et al., 2019), especially as the water balance represents the difference between two large fluxes:

$$ET - P = -\frac{Q}{A} - \frac{dS}{dt} \quad \text{Eq 4.1}$$

Where ET is evapotranspiration, P is precipitation, Q is the volumetric river discharge, A is the area of the basin studied, S is the water storage anomaly within the basin expressed as an equivalent water height, and t is time.

Satellite-based estimates of P and ET in the Congo Basin are subject to large uncertainties due to cloud cover and rainfall interference (e.g., Chambers et al., 2007, Wan 2008, Shi et al., 2022), leading to large disparities between datasets (e.g., Nicholson et al., 2018b, Weerasinghe et al., 2020). As a result, many studies have turned to the water balance as an alternative, combining river discharge and changes in terrestrial water storage to estimate $ET - P$ (e.g., Azarderakhsh et al., 2011, Rodell et al., 2004, Rodell et al., 2011, Sheffield et al., 2009, Moreira et al., 2019, Shi et al., 2022, Burnett et al., 2020). While changes in terrestrial water storage recently available via GRACE gravity estimates (Wahr et al., 2004) are mainly precision-limited and provide information on below-ground water fluxes, they have relatively coarse resolution compared to other P and ET estimates (e.g., Wahr et al., 2004, Reager et al., 2016, Landerer et al., 2012). Additionally, the uncertainty of in-situ river discharge measurements across the Congo Basin, is unknown. (e.g., Burnett et al., 2020, Alsdorf et al., 2016). Consequently, water balance estimates using these surface-based measurements typically are of the entire Congo Basin (Burnett et al. 2020).

However, we should expect that water balance in the Congo Basin exhibits significant spatial and temporal variation because P varies substantially across the basin at seasonal to decadal time scales (e.g., Nicholson et al. 2022). The northern hemisphere region experiences bi-annual rainy seasons with a very weak summer dry season in June, July, and August, while the southern hemisphere region experiences a single rainy season in the boreal fall (September-October-November) and winter (December-January-February) (Figure 4.1). The southern

hemisphere receives less rainfall during the dry season and more rainfall during the peak of the rainy season, resulting in a greater seasonal variation than that of the northern hemisphere. P seasonality and interannual variations also differ between the western and eastern basin (e.g., Mba et al., 2022, Balas et al., 2007), particularly as mesoscale convective systems that provide much of the rainfall for the basin increase in frequency toward the equator and the interior of the continent (Jackson et al., 2009).

River flows within the seven identified sub-basin drainage systems also exhibit significant spatial and temporal variation (e.g., N'kaya et al., 2022). The Northwest quadrant ($Quad_{NW}$) contains parts of the Lower Congo, Middle Congo, Oubangui, and Sangha and Ruki sub-basins, and fully contains the Sanga River. The Northeast quadrant ($Quad_{NE}$) contains parts of the Oubangui, Middle Congo, Ruki, Upper Congo, and a small part of the Tanganyika sub-basins. The Southwest quadrant ($Quad_{SW}$) contains parts of the Kasai, Ruki, Lower Congo, and "Below Kinshasa-Brazzaville" Congo sub-basins, and fully contains the Kasai river. The Southeast quadrant ($Quad_{SE}$) contains parts of the Kasai, Lomami, Upper Congo, and Tanganyika sub-basins (Alsdorf et al., 2016, N'kaya et al., 2022). However, contemporary discharge data only exists for three out of the six drainage systems. The Cuvette Centrale in the northwestern basin, which hosts the tropic's largest peatland complex in the world (Dargie et al., 2017), lacks in situ measurements in general. Many studies rely on indirect approaches such as remote sensing and modeling to estimate river discharge for many of these drainage systems (e.g., N'kaya et al., 2022, Alsdorf et al., 2016, Tshimanga and Hughes 2014). Therefore, observation-based data limitations have prevented the systematic evaluation of these spatial and temporal differences in the water budget and their relationship with biomass within the Congo Basin.

We employ a newly developed approach (J. Worden et al., 2019, Bailey et al., 2017, Shi et al., 2022) for quantifying $ET - P$ using satellite observations of the isotopic composition of water vapor. We improve upon prior estimates of ET-P averaged over the entire Congo Basin using gravity and river discharge data (e.g. Burnett et al., 2020). Those estimates are limited to the entire basin, whereas the satellite isotope measurements can resolve spatial gradients in the atmospheric water balance (Shi et al., 2022). We show using the isotopically-enabled version of the Community Atmospheric Model Version 5 (iCAM) climate model (Section 4.2.3) that these data can resolve $ET - P$ in four quadrants of the Congo basin (we describe this as "quadrant scale"). In addition, both the gravity-based terrestrial water storage and isotope data are essentially precision limited (Aumann et al., 2019, Rodell et al., 2004) for the spatial scales considered here, allowing for improved confidence in the monthly to interannual to decadal variation of atmospheric water balance in these regions. We use these water balance estimates to calculate new time and space-averaged, quadrant-scale ET and net river discharge estimates additionally using measurements of quadrant-scale P and terrestrial water storage (TWS) changes. We can then use these estimates to examine space and time variability in key moisture fluxes within the basin as well as compare our ET estimates to other ET estimates that are calculated using modeling and/or reanalysis. While we cannot deduce whether our estimated $ET - P$, ET, and net river discharge are more accurate than existing products because of a lack of validation data, we can compare those products to our estimates to check for consistency.

4.2 Data and Methods

In this section, we first discuss the sources of data for our study (4.2.1). We then demonstrate how we can use satellite observations of water vapor isotopes (or deuterium content of water vapor) to quantify $ET - P$ using simulations from iCAM (Sections 4.2.2-2.3).

4.2.1 Data Sources

We list our data sources for ET, P, changes in terrestrial water storage ($\frac{dS}{dt}$), river discharge, and aboveground biomass (AGB). We use multiple different sources for ET and P to compare to our calculated $ET - P$ and ET products as well as explore the spread in ET and P products over the Congo Basin. The data sources for the water vapor isotopes are described in section 4.2.2. The data sources for model verification of our methodology are described in section 4. 2.3

ET: We use the following ET datasets in our study:

(1) We use the Global Land Evaporation Amsterdam Model (GLEAM) v3.6b total ET, which is based on satellite data and the Priestly Taylor model (e.g., Miralles et al., 2011, Martens et al., 2017) to separately estimate the different components of ET.

(2) We use the Global Land Data Assimilation System (GLDAS) L4 v2.1 GLDAS_NOAH025_M ET product available between 2000-2022 at monthly time steps (Rodell et al., 2004, Beaudoing and Rodell, 2019).

(3) We use the Priestly Taylor- Jet Propulsion Laboratory (PT-JPL) ET data that is created by combining reanalysis and the Moderate Resolution Imaging Spectroradiometer (MODIS) observations (Fisher et al, 2008).

(4) We use the MODIS MOD16A3GF_006_ET_500m total yearly ET product, which is based on the Penman-Monteith equation (Running et al., 2021).

(5) We use the Fifth Generation of the European Center for Medium-Range Weather Forecasts (ECMWF) Reanalysis (ERA5) monthly mean of daily means of the surface latent heat flux, which is then converted to ET. The reanalysis combines observations

with model forecasts to estimate dynamic and thermodynamic atmospheric quantities (Hersbach et al., 2020).

P: We use the following P datasets in our study:

1) We use the Tropical Rainfall Measuring Mission (TRMM) 3B43 gridded, monthly P estimates that are generated using a combination of microwave and radar sensors calibrated with gauge data from the Global Precipitaiton Climatology Center (GPCC) (Huffman et al., 2007). We use TRMM Pestimates to evaluate $ET - P$ and ET in this study as this dataset performs well in this region (Nicholson et al., 2018b); a comparison of other P products to TRMM P is found in Appendix A.
2) We use the Climate Hazards Group InfraRed Precipitation with Station data (CHIRPS), Version 2.0 monthly P available from 1981 to near-present (Funk et al., 2015).
3) We use the Precipitation Estimation from Remotely Sensed Information using Artificial Neural Networks-Climate Data Record (PERSIANN-CDR), monthly P produced using the PERSIANN algorithm on infrared satellite data and trained on National Centers for Environmental Prediction (NCEP) P data (Ashouri et al., 2015).

Gravity-Based Water Storage Anomalies: In addition, basin-scale water storage anomalies (S) come from the GRACE satellite (Landerer et al., 2012) calculated by Burnett et al. (2020) using the arithmetic mean of the GRACE solutions on 1° grids from GeoForschungsZentrum Potsdam (GFZ), Jet Propulsion Laboratory (JPL), and Center for Space Research at the University of Texas at Austin (CSR) (e.g., Wahr et al., 2006; Sakumura et al., 2014, Burnett et al., 2020). Quadrant-scale water storage anomalies come from the same centers, GFZ, JPL, and CSR, and are the GRACE/GRACE-FO Mascon Ocean, Ice, and Hydrology Equivalent Water Height RL06

V2 at 0.5° spatial resolution available between 2002-2021 (Landerer et al., 2019, Wiese et al., 2019, Watkins et al., 2015, Save et al., 2016, Save et al., 2020, Loomis et al., 2019).

Water storage anomalies (S) from GRACE are converted to $\frac{dS}{dt}$ using a centered-difference approach at the monthly timescale (Burnett et al., 2020, Landerer et al., 2010):

$$\frac{dS}{dt_n} = \frac{(S_{n+1} - S_{n-1})}{2\Delta t} \qquad \text{Eq. 4.2}$$

Where Δt is 1 month. The uncertainty of the dS/dt is calculated as half the difference between the highest and lowest dS/dt values from the three GRACE S solutions in any given month (Lee et al., 2011, Burnett et al., 2020).

River Discharge: River discharge estimates come from the SO-HYBAM river discharge (Q) measurements from a station located at Kinshasa-Brazzaville. The area of the Congo Basin (A) is found using the HydroSHEDS 15 arcsec boundary for the Congo Basin, which produces a total basin area of 3705220 km^2 (Lehner et al., 2008, Burnett et al., 2020). Error in river discharge measurements is poorly characterized within this region (e.g., Burnett et al., 2020, Alsdorf et al., 2016, Kitambo et al., 2022). Prior studies have noted a range of uncertainties between 5-20% for these discharge measurements (O'Loughlin et al., 2020, Burnett et al., 2020). We assume a 20% error in the Q/A measurements to be consistent with Burnett et al. (2020) as we use some of their provided estimates in our study; however, this is likely to be conservative especially as the observed gauge is quite inland and can provide a good representation of the upstream discharge (e.g., Alsdorf et al., 2016).

AGB: AGB is estimated by Xu et al. (2021) using a combination of lidar, global modeling, and satellite data. The following steps were taken to produce these estimates: 1)

Ground inventory plots (>100,000 in number) are integrated with airborne and satellite data, with models used to relate lidar-derived metrics and radar backscatter to AGB estimates from ground plots; 2) Spatially aggregated samples of woody vegetation AGB mean and variance at 10-km spatial resolution are developed using satellite and airborne lidar as training data; and 3) AGB is estimated by using the training data in spatial-temporal machine learning models. The satellite data used in the process come from the Ice, Cloud, and land Elevation Satellite (ICESAT), the Shuttle Radar Topography Missions (SRTM), the Advanced Land Observing Satellite (ALOS), Landsat, the Moderate Resolution Imaging Spectroradiometer (MODIS), and QuikSCAT (QSCAT). More details on this product can be found in Xu et al. (2021).

4.2.2 Deuterium Content of Water (δD) and dd04

Bailey et al. (2017) and Shi et al. (2022) have demonstrated the use of satellite observations of tropospheric water vapor deuterium content in estimating $ET - P$. This can be achieved by normalizing the deuterium content to a representative water vapor value in the free troposphere. Covariation between the normalized deuterium content and $ET - P$ holds in tropical regions with significant mixing between the surface and atmosphere.

To calculate δD, we use single pixel tropospheric retrievals of HDO and H_2O between 230-912 hPa from the Atmospheric Infrared Sounder (AIRS) radiances using the optimal estimation. We use AIRS data instead of those from the Tropospheric Emission Spectrometer (J. Worden et al., 2007) due to its longer record and greater sampling. The AIRS data is bias corrected as suggested by Herman et al. (2021) due to smoothing and systematic errors, as well as instrument noise. We first normalize the deuterium content of water vapor to a reference water vapor concentration of 4 $mmol\ mol^{-1}$ by (1) regressing the observed HDO profile against the observed H_2O profile; and (2) calculating the HDO value that matches a reference H_2O of 4

mmol/mol (Bailey et al., 2017). From the resulting HDO and H_2O values, we obtain a proxy for atmospheric water balance that we refer to as $dd04$.

4.2.3 iCAM Model relationships between dd04 and ET-P in the Congo Basin

In this section, we demonstrate the linear relationship between $dd04$ and $ET - P$ in the Congo Basin on basin and quadrant-scale using the isotopically enabled version of the Community Atmosphere Model 2 (iCAM; Danabasoglu et al., 2020, Shi et al. 2022). We demonstrate the linear regression between modeled $dd04$ and $ET - P$ on a basin-scale in Figure 4.2a. To compare to the AIRS $dd04$ data, we calculate an "AIRS view" of the iCAM model $dd04$, as recommended in the TROPESS AIRS HDO/H2O Level 2 User Guide and Validation Document (J. Worden et al., 2019). We thus project the iCAM model HDO and H_2O profiles through the AIRS observation operator provided with the AIRS data. Additionally, we use iCAM and AIRS HDO/H2O data between 230-912 hPa, as we find that the iCAM regression performs better using this pressure range compared to the suggested AIRS pressure range for this data in the User Guide, 400-825 mb (not shown). As illustrated in Figure 4.2, the modeled $ET - P$ and $dd04$ exhibit a well-correlated relationship ($R = 0.876$). Using this basin-scale linear regression, we find $ET - P$ using iCAM measurements via the following equation:

$$ET - P = 0.31 \times dd04 + 64.29 \quad \text{Eq 4.4}$$

In Figure 4.2 (b-d), we compare the $ET - P$ iCAM record from 2003 to 2017, its seasonality, and interannual variations to those calculated using Equation 4.4. Note that the RMSE for Figure 4.2d applies to the IAVs rescaled temporally to the seasonal level to better visually compare the predicted versus actual $ET - P$ IAVs. The RMSE value for the monthly IAV's can be found in Appendix A. This $ET - P$ / $dd04$ relationship exhibits the strongest performance during dry season months, but the weakest performance during wet season months

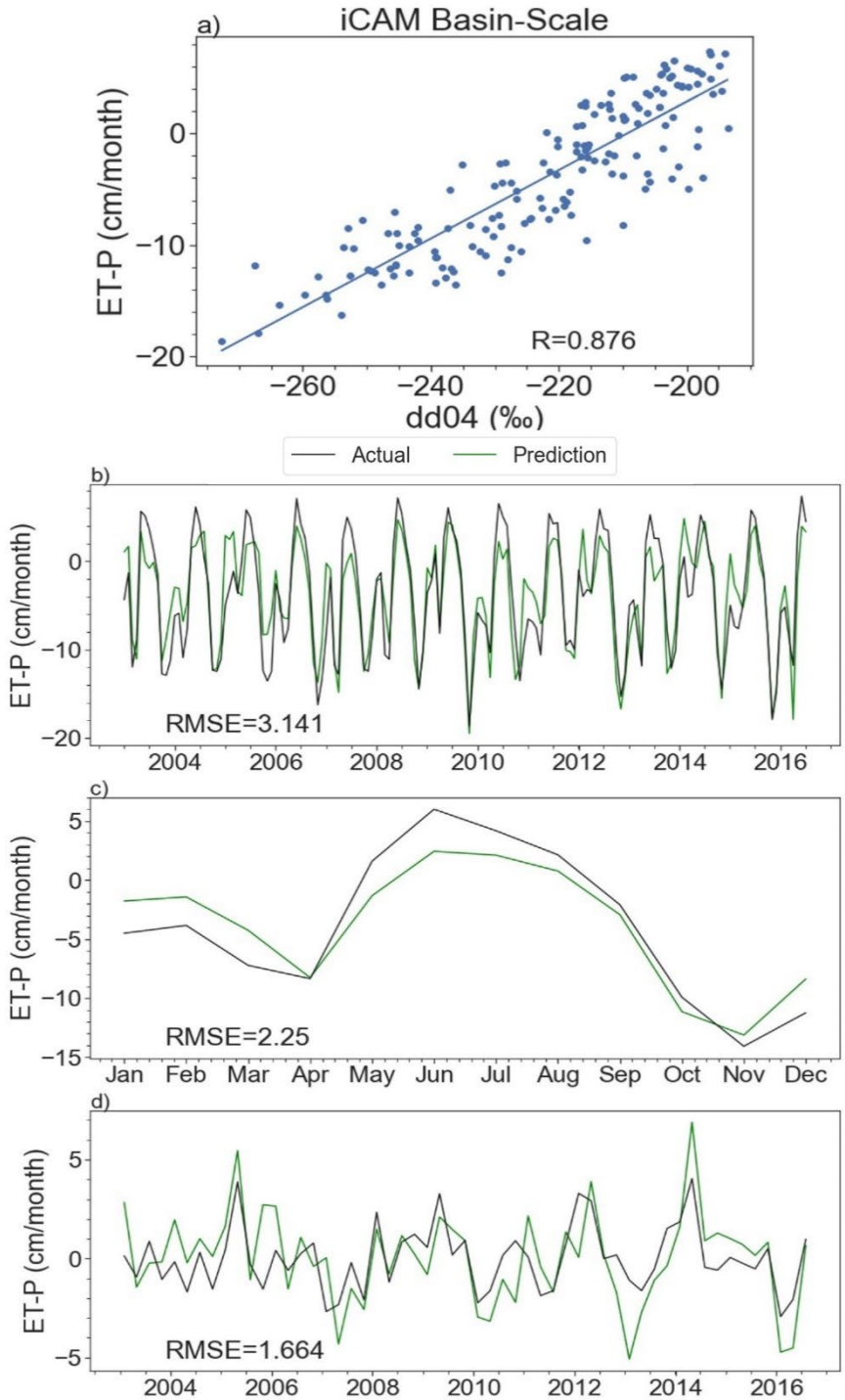

Figure 4.2: Linear regression of the iCAM $dd04$ estimates (after projecting through the AIRS observation operator) and the iCAM ET-P on a basin scale; b)-d): Multi-year, seasonal cycle, and inter-annual variations (IAVs) of model estimates of ET-P compared to regression-based ET-P. IAVs have been resampled to a seasonal resolution to better compare; the monthly resolution and associated RMSE are described in Appendix A.

(Figure 4.2c). This weaker performance could be due to additional isotopic processes that are

more frequent during rainy seasons and can change measured δD (e.g., Galewsky et al., 2016) and masks the original isotopic signal. For example, heavier water vapor isotopes preferentially condense, thus depleting δD during rainfall events. Furthermore, large-scale convergence of air masses during deep convection can bring in relatively depleted water vapor that overtakes any enrichment from surface ET. More descriptions of how these processes can affect the isotopic composition of water vapor, or possible confounding factors of this relationship can be found in Galewsky et al. (2016) and Bailey et al. (2017).

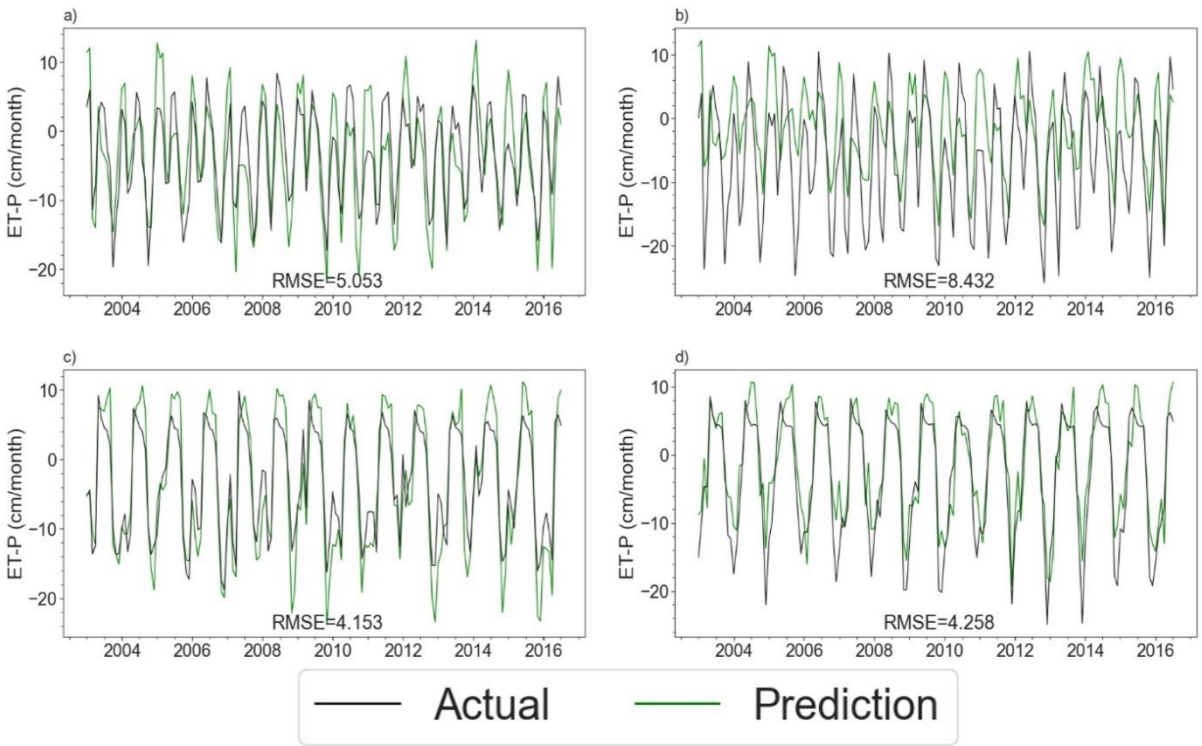

Figure 4.3: Multi-year record of iCAM ET-P (black) and regression-estimated ET-P (green) using the basin-scale regression equation for each quadrant: a) $Quad_{NW}$; b) $Quad_{NE}$; c) $Quad_{SW}$; and d) $Quad_{SE}$.

As discussed previously, basin-scale river discharge estimates limit water balance estimates based on gravity and river discharge data to the entire basin. Similar to the approach taken by Shi et al., (2021) in the Amazon, the new deuterium-based estimates of $ET - P$ offer an opportunity to improve on the spatial knowledge of $ET - P$, ET, and $\frac{Q}{A}$estimates in the Congo.

We first calibrate the basin-scale, deuterium-based $ET - P$ with the terrestrial water storage and river discharge data. Then, using these same regression coefficients, with $dd04$ averaged over

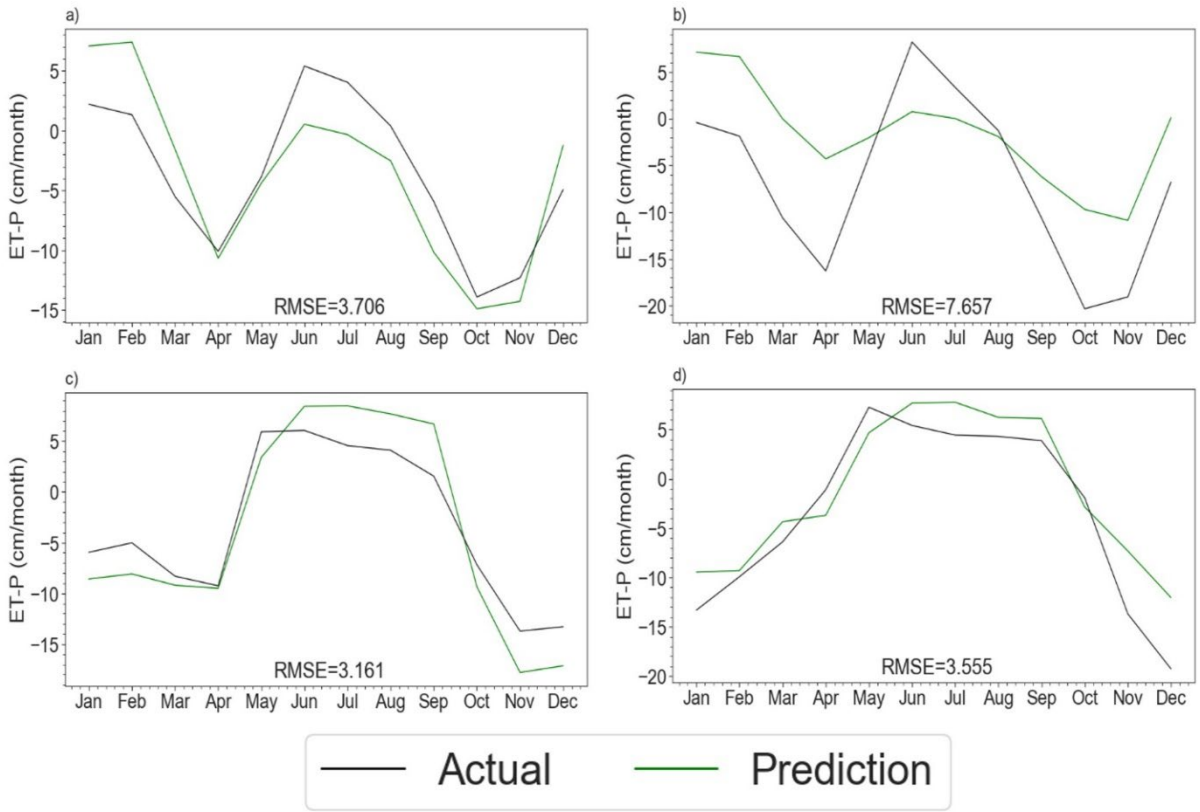

Figure 4.4: Seasonality of iCAM ET-P (black) and regression-estimated ET-P (green) using the basin scale regression equation for each quadrant: a) $Quad_{NW}$; b) $Quad_{NE}$; c) $Quad_{SW}$; and d) $Quad_{SE}$.

the four quadrants (Figure 4.1a), we estimate $ET - P$ in the four quadrants. We use these same regression coefficients, instead of re-calculating these coefficients for each quadrant, because the river discharge measurements are only available on a basin scale. We choose to limit this calculation to four quadrants as the basin-scale linear regression coefficients do not perform well at estimating $ET - P$ on smaller than quadrant scale (not shown).

To evaluate the uncertainty of this method, we calculate the RMSE between modeled and actual $ET - P$ within the basin using iCAM data, following the methodology outlined in Shi et

al. (2022), as lack of data in this region prevents us from evaluating this uncertainty empirically. Figures 4.3, 4.4, and 4.5 show the difference between $ET - P$ over each quadrant using iCAM, as well as the calculated RMSE between the predicted $ET - P$ and modeled $ET - P$ for the long-term record, seasonal, and interannual variations, respectively. To improve visual ease of comparison, we scale the interannual variability to seasonal values; the monthly IAVs are shown in Appendix A. The regressions perform best in capturing the interannual variability and show better overall performance in the southern hemisphere than in the northern hemisphere. The

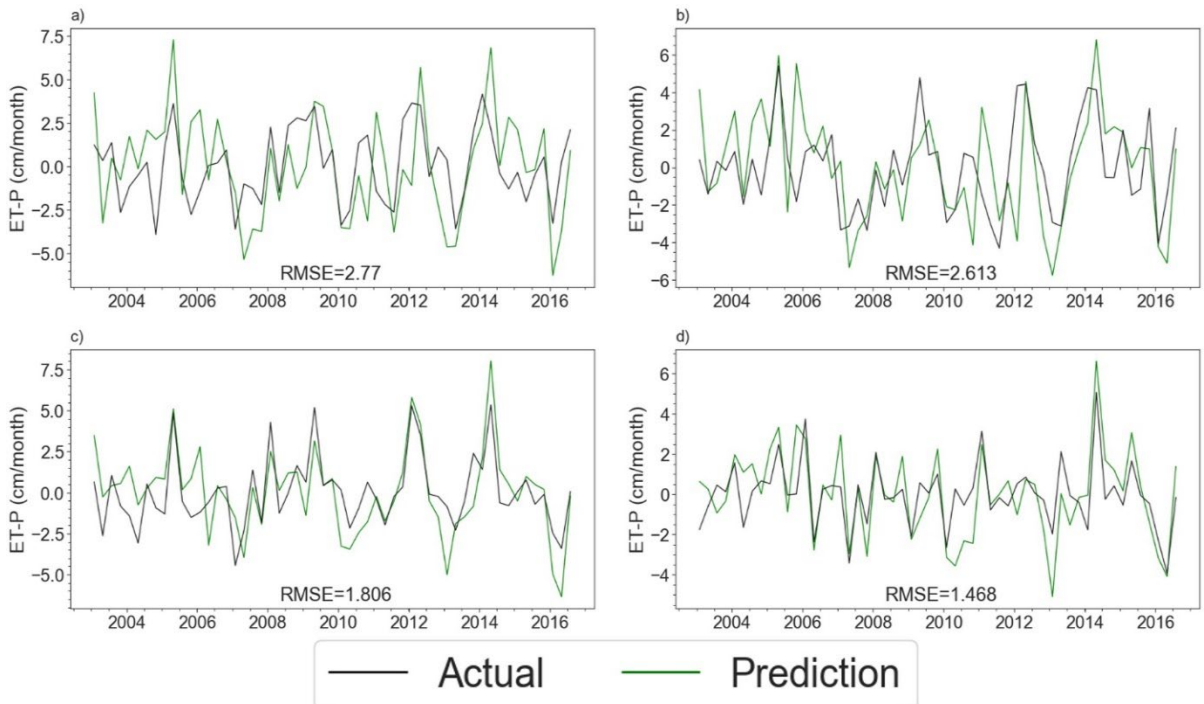

Figure 4.5: Interannual variations (IAVs) of iCAM ET-P (black) and regression-estimated ET-P (green) using the basin-scale regression equation for each quadrant: a) $Quad_{NW}$; b) $Quad_{NE}$; c) $Quad_{SW}$; and d) $Quad_{SE}$.

regression is less effective in $Quad_{NE}$, which has the highest RMSE errors (Figures 4.3, 4.4, and 4.5). It is possible that these higher errors are introduced because mesoscale convective systems are more prominent within this region (e.g., Jackson et al., 2009), which could introduce large

scale changes in δD from convective processes such as rainfall re-evaporation without large

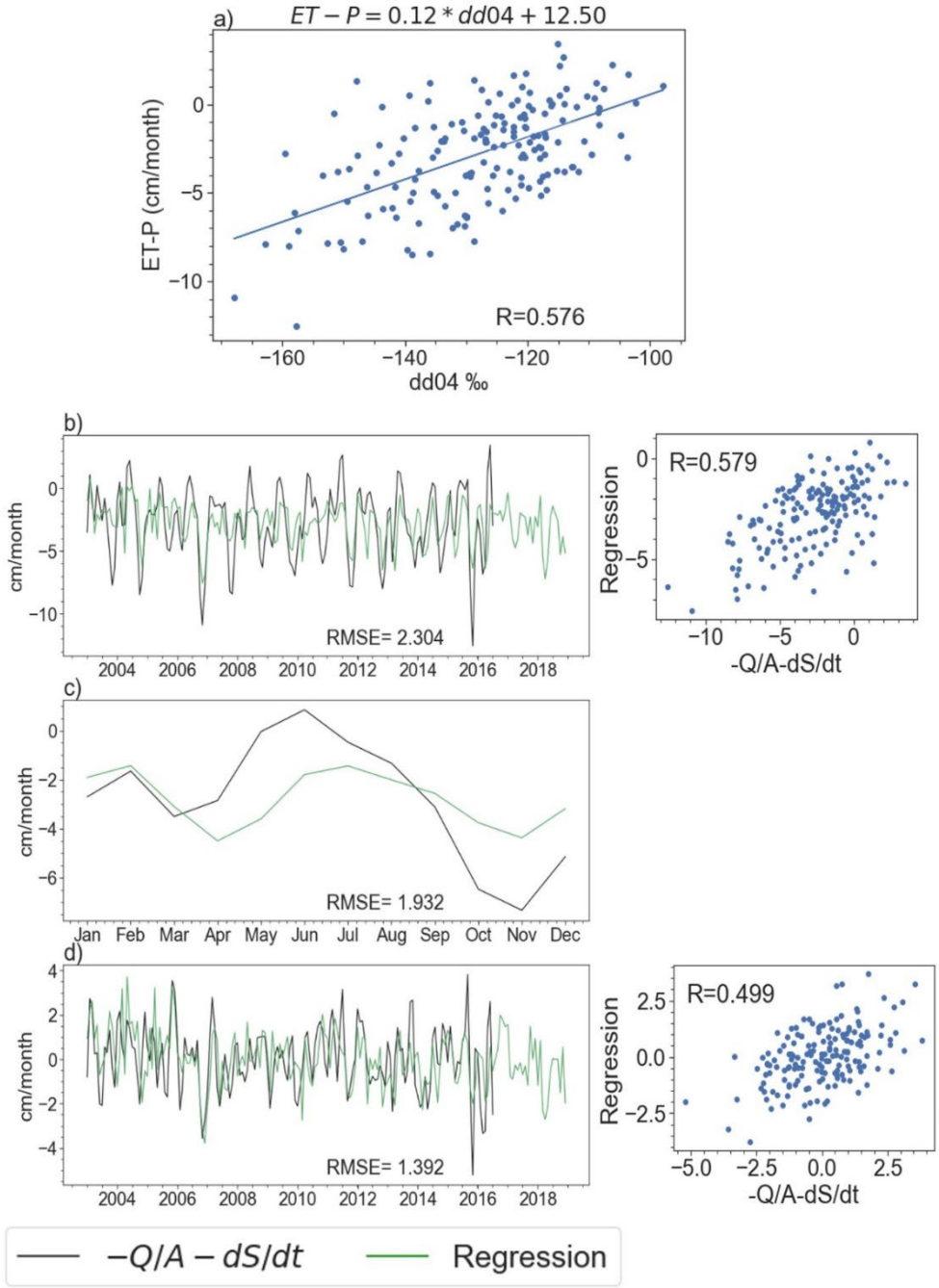

Figure 4.6: a) Basin-scale linear regression between AIRS $dd04$ measurements and $-\frac{Q}{A} - \frac{dS}{dt}$; b) long-term record of our calculated $ET - P$ compared to $-\frac{Q}{A} - \frac{dS}{dt}$ as well as a scatter plot showing the linear relationship between them; c) seasonality of our calculated $ET - P$ compared to $-\frac{Q}{A} - \frac{dS}{dt}$; and d) interannual variations of our calculated $ET - P$ compared to $-\frac{Q}{A} - \frac{dS}{dt}$ as well as a scatter plot showing the linear relationship between them.

scale changes in atmospheric humidity (Bailey et al., 2017). Additionally, model error could add to these uncertainties.

4.3 Results

4.3.1 Observationally-Based, Basin-scale Relationships Between $dd04$ and $ET - P$

We can expect that a linear relationship between $dd04$ measurements and $ET - P$ exists because the sensitivity of water vapor isotopes to large-scale water cycle processes can be used to distinguish evaporation versus precipitation dominated environments. These environments determine large scale moisture flux diverge or convergence, such that when normalizing the isotope ratio to a fixed specific humidity, water vapor isotopes should be able to distinguish between these two regimes (Bailey et al., 2017). Previous studies thus show that this relationship exists most strongly within the tropics, but also persists globally (Shi et al., 2021, Singh et al., 2023).

However, because there is a considerable range of ET and P products in the Congo Basin, as discussed in several studies (Nicholson and Klotter 2021, Sun et al., 2018, Negrón Juárez et al., 2009, da Motta Paca et al., 2019, Pan et al., 2020, Weerasinghe et al., 2020, Appendix A), using ET and P directly from these data to estimate water balance is less reliable. Instead, we utilize the surface water balance (right hand side of Equation 4.1) to quantify a linear relationship. Basin-scale $\frac{dS}{dt}$ and $\frac{Q}{A}$ data are taken from a public dataset generated by Burnett et al., (2020); their sources are described in the previous section.

Using these basin-scale measurements, we calculate $ET - P$ using the following equation:

$$ET - P = 0.12 * dd04 + 12.12 \quad \text{Eq. 4.5}$$

Figure 4.6 illustrates the linear relationship between $-\frac{Q}{A}-\frac{dS}{dt}$ and $dd04$ derived from AIRS, along with the multi-year record, seasonality, and IAVs of our calculated $ET-P$. A comparison between our results and other remotely-sensed and reanalysis ET and P products is available in Appendix A. We calculate both the accuracy and precision errors of our estimated $ET-P$ using the AIRS $dd04$ estimates. We assume that the accuracy errors in the GRACE terrestrial water storage estimates, as well as the errors in the AIRS $dd04$ estimates are small compared to the river discharge error, which is unknown and has been assigned an estimated error of 20% (Shi et al., 2022, Burnett et al., 2020, Landerer and Swenson 2012). Therefore, we assume that the error in the Q/A estimates dominates the error in $-\frac{Q}{A}-\frac{dS}{dt}$. However, this error in $-\frac{Q}{A}-\frac{dS}{dt}$ will change based on the season. As there are certain times within the year when $\frac{dS}{dt}=0$, we choose a final accuracy error of $0.2\times\frac{Q}{A}$ to apply to our $ET-P$ estimates. Therefore, we report a time-averaged accuracy error of 0.56 cm/month. For the precision error, we calculate the error using first principles:

$$(ET-P)_{err}=\sqrt{Q_{err}^2+\frac{dS}{dt}^2_{err}} \quad \text{Eq. 4.6}$$

The precision error for basin-scale $ET-P$ is 0.91 cm/month.

Our calculated ET-P (Figure 4.6b) compares well with $-\frac{Q}{A}-\frac{dS}{dt}$ (hereafter referred to as discharge/gravity water balance) although it does not generally capture extreme discharge/gravity water balance values. We examine both the seasonality and IAVs to determine the cause. Our calculated seasonal $ET-P$ (Figure 4.6c) remains below zero throughout the year, whereas the seasonal discharge/gravity water balance goes above zero during May-June. While the overall seasonal change agrees are consistent between the deuterium and gravity based

measurements, the deuterium based $ET - P$ does not capture the same extreme highs and lows as the discharge/gravity water balance estimates. On the other hand, the interannual variability of the deuterium-based water balance is consistent with the discharge/gravity water balance, generally matching the sign of the anomalies and how they change over time: both over short-time scales (within a year) and over long-term time scales, i.e., over the whole record. For example, both datasets show higher values in the earlier part of the record, lower values near 2007, and similar variations near zero thereafter. Furthermore, discharge/gravity water balance IAVs indicate large atmospheric water balance variability between 2015-2017, during which an extreme El Niño event (Santoso et al., 2017) induced severe drought within the basin via increases in both soil moisture and atmospheric water stress (Rifai et al., 2019). Our calculated $ET - P$ IAVs match the direction but not the magnitude of the anomalies.

4.3.2 Estimates of ET and ET/P for the Entire Congo Basin

	Mean ET (cm/month)	Mean ET/P
Regression-Based	9.71 ± 0.94	0.77 ± 0.02
ET_{wb} (Burnett et al., 2020)	9.75 ± 0.94	0.76 ± 0.02
MODIS	10.25 ± 0.04	0.83 ± 0.01
Fisher et al., 2008	8.34 ± 1.3	0.67 ± 0.02
GLEAM	9.47 ± 1.93	0.77 ± 0.02
GLDAS	9.60 ± 0.04	0.77 ± 0.01
ERA5	11.12 ± 0.04	0.90 ± 0.01

Table 4.1: Basin-scale mean ET and ET/P for the different ET datasets. TRMM P is used to calculate ET/P.

We next estimate basin-scale ET estimates using our regression-based water balance estimates. Simply adding P to our calculated $ET - P$ yields an unrealistic ET seasonality, as we find that P dominates the atmospheric water balance variability (Appendix A). Only when we

additionally average in time does our calculated ET compare well with other existing ET estimates. We compare our calculated ET to the following datasets: MODIS ET, water-balance calculated ET from Burnett et al. (2020), GLDAS ET, PT-JPL ET from Fisher et al. (2008), and GLEAM ET (Table 4.1).

We calculate the errors for the following ET datasets using the time-averaged standard error of the mean: MODIS, GLEAM, ERA5, PT-JPL (Fisher et al., 2008), and GLDAS ET products. The error in ET_{WB} and regression-based ET is calculated using first principles, with the regression-based ET error in particular calculated by:

$$ET_{err} = \sqrt{(\frac{RMSE_{ET-P}}{\sqrt{n}}^2 + P_{err}^2)} \quad \text{Eq. 4.7}$$

Where the RMSE is the RMSE between the iCAM ET-P and iCAM regression-based $ET - P$, n is the length of the time series, and P_{err} is the standard error of the mean of the TRMM P estimates. We additionally use this to calculate the error on ET on quadrant scales.

Our calculated ET, 9.71 cm/month, compares well with water-balance ET, GLEAM ET, and GLDAS ET with a range of $9.47 - 9.75$ cm/month. MODIS and ERA5 ET are higher, 10.25 cm/month and 11.12 cm/month, respectively. ET estimates from Fisher et al., 2008, which combines MODIS and reanalysis ET products, has the lowest ET estimate at 8.34 cm/month.

We also compare the contribution of ET to P (ET/P) using TRMM P and ET from the previously mentioned data sets. We use the following to calculate the error in $\frac{ET}{P}$:

$$(\frac{ET}{P})_{err} = \sqrt{\frac{ET_{err}}{ET}^2 + \frac{P_{err}}{P}^2} \quad \text{Eq. 4.8}$$

Where ET_{err} is the error in the ET products as described above. We use this to additionally calculate the error in ET/P on quadrant scales.

Our analysis reveals a large contribution (67-90%) of ET towards P, consistent with previous studies (e.g., Sorí et al., 2022, S. Worden et al., 2021, Risi et al 2013). This suggests that the contribution of atmospheric moisture flux convergence (MFC) to P $\left(\frac{MFC}{P}\right)$, should range between 10-33%. While no MFC observations exist over the Congo Basin, ERA5 reanalysis estimates suggest that MFC contributes about 18% contribution of MFC to P on a basin-scale. MODIS ET best closes this moisture flux budget (83% contribution of ET to P), but our calculated ET estiates, GLEAM, and GLDAS also perform well in closing this budget.

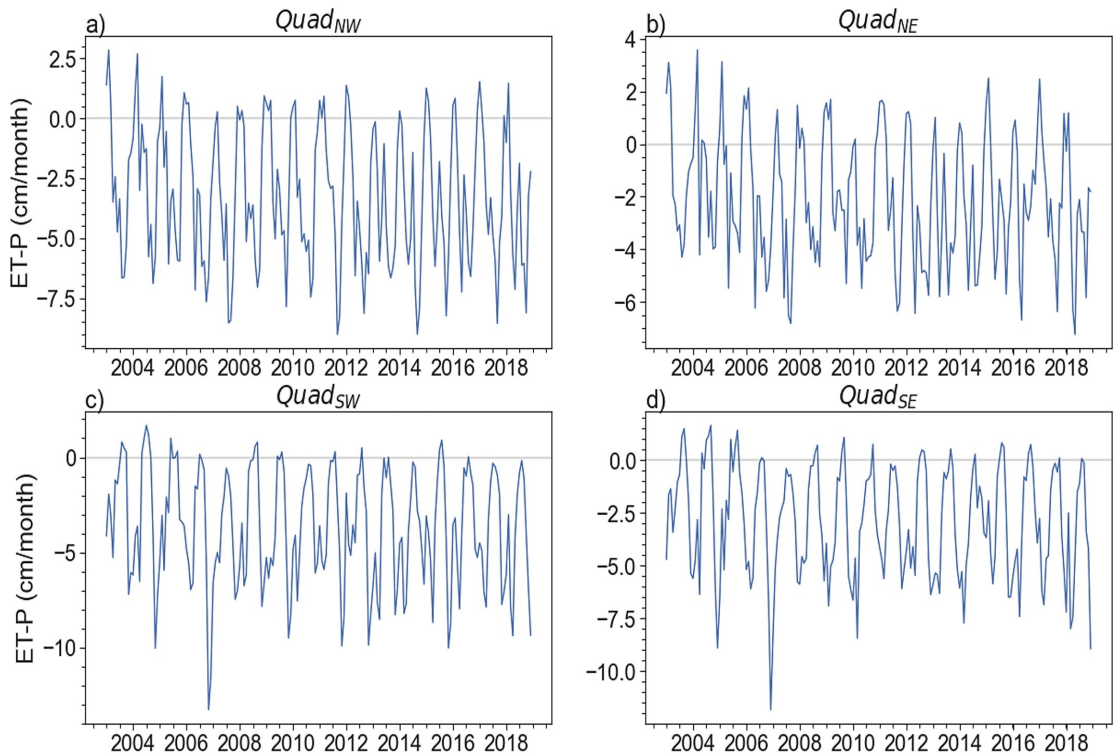

Figure 4.7: $ET - P$ multi-year record for each quadrant calculated using the basin-scale linear relationship.

4.3.3 Estimating $ET - P$ in Four Quadrants

We next calculate quadrant-scale $ET - P$ using quadrant-averaged $dd04$ measurements in the basin-scale linear regression equation (Equation 4.5). Because we do not have river

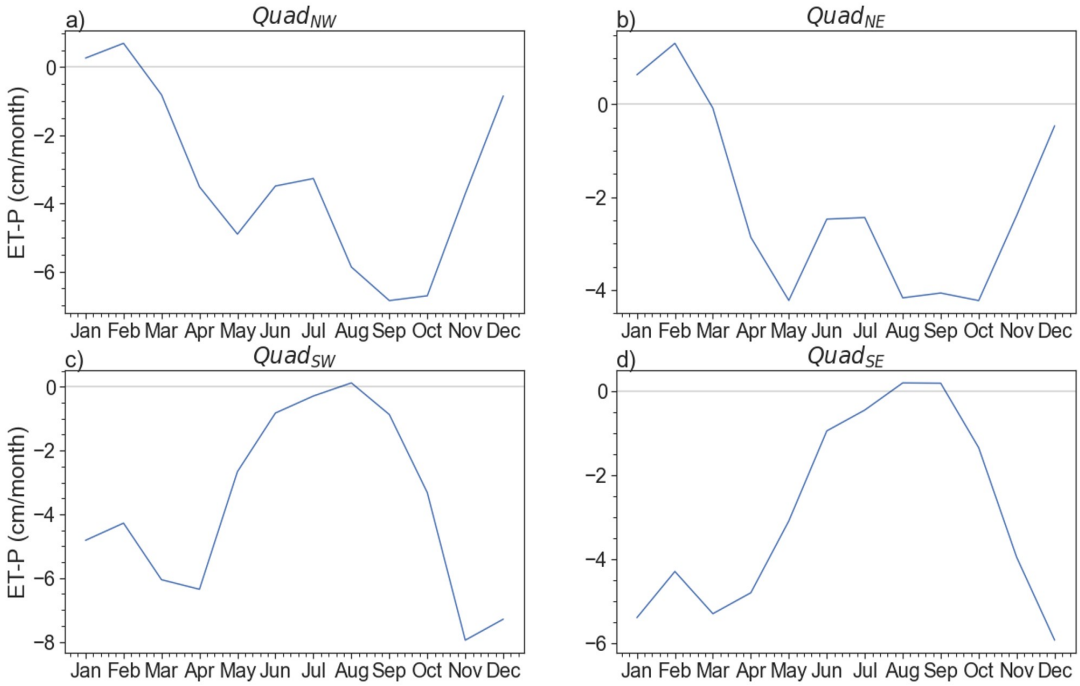

Figure 4.8: $ET - P$ seasonal cycle for each quadrant calculated using the basin-scale linear relationship.

discharge at these scales, we estimate the accuracy in $ET - P$ by applying the RMSEs shown in the iCAM model (Section 4.2.3) for our $ET - P$ multi-year record, seasonality, and IAVs (Figures 7, 8, and 9).

Seasonally, $ET - P$ is greater than zero in January and February in the northern hemisphere, consistent with low P (less than 5 cm/month, Figure 4.1b). However, P is only slightly greater during December when the seasonal $ET - P$ is less than zero, indicating an increase in ET during January and February as the Congo transitions to its spring rainy season. In the southern hemisphere, seasonal P drops to near-zero during JJA (Figure 4.1b); seasonal $ET -$

P also near or above zero (Figure 4.8 c, d) indicates that ET decreases significantly during the JJA dry season as well. This is consistent with observed decreases in solar-induced fluorescence (SIF), a proxy for photosynthesis and hence ET (Frankenberg et al., 2011), over the Southern Congo during this period (Jiang et al., 2023).

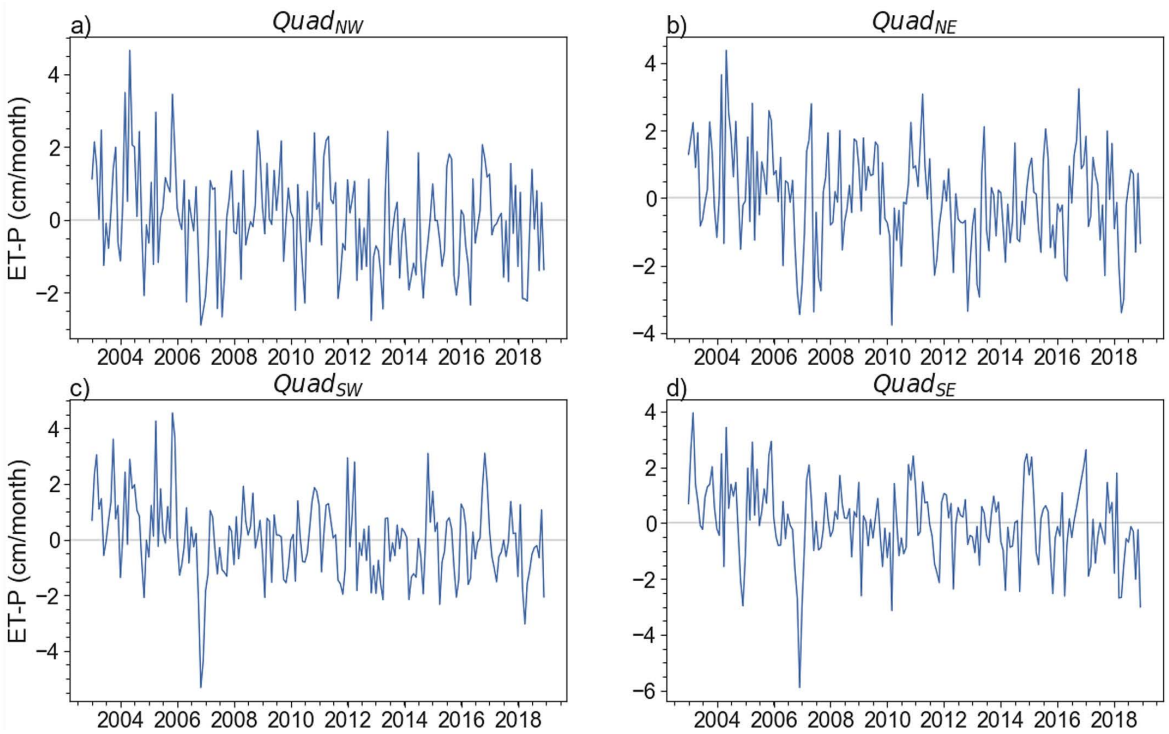

Figure 4.9: $ET - P$ IAV's for each quadrant calculated using the basin scale linear relationship.

4.3.4 Estimating ET, ET/P, and Q/A in Each Quadrant

We next calculate quadrant-scale ET, ET/P, and Q/A using the deuterium-based $ET - P$ estimates. We compare our estimates to other ET products. Such estimates are useful for examining quadrant-scale variabilities in the Congo Basin moisture fluxes that could indicate different moisture regimes, and hence different responses to climatic changes such as the observed decline in April-June rainfall (Nicholson et al., 2022). We calculate ET by adding P to $ET - P$ for each quadrant. Similarly, we calculate net river discharge (Q/A) by adding GRACE

dS/dt estimates to $ET - P$ for each quadrant. All calculations are averaged over both space and time.

We calculate the error in Q/A by:

$$\sqrt{ET_{err}^2 + P_{err}^2 + \frac{dS}{dt_{err}}^2} \quad \text{Eq. 4.9}$$

For the Q/A calculated using the remotely sensed and reanalysis ET products, and the error in Q/A using the regression-based ET-P products as:

$$\sqrt{(\frac{RMSE_{ET-P}}{\sqrt{n}}^2 + \frac{dS}{dt_{err}}^2} \quad \text{Eq. 4.10}$$

We first compare our time and space-averaged ET estimates to ET from MODIS, GLEAM, ERA5, PT-JPL from Fisher et al. (2008), and GLDAS. Unlike the basin scale ET estimates which show agreement across datasets, substantial disparity among the ET estimates exists between quadrants. We show that ET in $Quad_{NW}$ ranges from $9.00 - 12.14$ cm/month, ET in $Quad_{NE}$ ranges from $9.13 - 12.05$ cm/month, ET in $Quad_{SW}$ ranges from $7.90 - 10.63$ cm/month, and ET in $Quad_{SE}$ ranges from $7.44 - 10.41$ cm/month. Our regression-based ET estimates compare best with GLEAM and GLDAS ET estimates for all four quarters. These three ET estimates show higher ET in $Quad_{NW}$ and $Quad_{NE}$, and lower ET in $Quad_{SW}$ and $Quad_{SE}$. These variations generally correspond to biomass variability between the northern and southern hemisphere. For example, the fraction of biomass with values $> 100\ mgC/ha$ (high biomass overlaps with tropical rainforest parts of the basin; e.g., Verhegghen et al., 2012) are 0.36, 0.24, 0.10, and 0.08 in $Quad_{NW}$, $Quad_{NE}$, $Quad_{SW}$, and $Quad_{SE}$, respectively. Lowest ET corresponds with the lowest fraction of high-biomass vegetation in $Quad_{SE}$. However, while $Quad_{NW}$ contains the most high-biomass vegetation, including a large wetland and peatland

complex (Alsdorf et al., 2016, Dargie et al., 2017), $Quad_{NE}$ has the highest ET except for MODIS ET. It is possible that higher ET in $Quad_{NE}$ could be due to ET transported from other parts of the basin via low-level winds under 850 hPa (S. Worden et al., 2021).

We additionally calculate ET/P and MFC/P for all four quadrants to understand variations in moisture contributions to P in each quadrant. We show that ET/P in $Quad_{NW}$ ranges from $0.67 - 0.90$, ET/P in $Quad_{NE}$ ranges from $0.66 - 0.87$, ET/P in $Quad_{SW}$ranges from $0.64 - 0.86$, and ET/P in $Quad_{SE}$ ranges from $0.68 - 0.95$. Our calculated ET/P estimates most closely match ET/P estimates using GLEAM and GLDAS. These three datasets all show a similar contribution of ET to P over all four quadrants, with ET contributing slightly less to P in $Quad_{SW}$ and $Quad_{SE}$. Meanwhile, mean MFC/P is 0.12 in $Quad_{NW}$, 0.18 in $Quad_{NE}$, 0.18 in $Quad_{SW}$, and 0.23 in $Quad_{SE}$. This suggests that despite different $P$and vegetation regimes between the northern and southern quadrants, ET still significantly contributes to P everywhere within the Congo Basin.

We next calculate quadrant-scale, mean net river discharge estimates by adding quadrant-scale $\frac{dS}{dt}$ estimates to our quadrant-scale $ET - P$ estimates. The spatial limitations in GRACE gravity measurements provide additional motivation to limit our calculations to a quadrant-scale (e.g., Shi et al., 2022). The average of our quadrant-scale net river discharge estimates calculated from our regression-based $ET - P$ is equal to the basin-scale mean net river discharge, adding confidence to our results. Similar to basin-scale river discharge estimates, mean net river discharge in all four quadrants is lower than mean ET.

	$Quad_{NW}$			$Quad_{NE}$			$Quad_{SW}$			$Quad_{SE}$		
	ET	**ET/P**	**Q/A**	**ET**	**ET/P**	**Q/A**	**ET**	**ET/P**	**Q/A**	**ET**	**ET/P**	**Q/A**
Regression-based	10.20 ± 0.56	0.76 ± 0.06	2.93± 1.32	11.73 ± 0.67	0.84 ± 0.07	1.87 ± 1.35	8.70 ± 0.45	0.70 ± 0.06	3.57 ± 1.28	8.83 ± 0.43	0.73 ± 0.06	2.81 ± 1.36
MODIS	10.88 ± 0.05	0.81 ± 0.01	2.37 ± 1.30	10.43 ± 0.04	0.75 ± 0.01	3.29 ± 1.25	9.26 ± 0.04	0.74 ± 0.01	3.00 ± 1.27	10.41 ± 0.1	0.95 ± 0.01	0.65 ± 1.35
PT-JPL	9.00 ± 0.16	0.67 ± 0.02	4.18 ± 1.31	9.13 ± 0.20	0.66 ± 0.02	4.54 ± 1.27	7.90 ± 0.16	0.64 ± 0.02	4.34 ± 1.28	7.44 ± 0.17	0.68 ± 0.02	3.59 ± 1.36
GLEAM	10.38 ± 0.27	0.77 ± 0.04	2.76 ± 1.30	10.72 ± 0.29	0.77 ± 0.04	3.00 ± 1.26	9.18 ± 0.23	0.73 ± 0.04	3.15 ± 1.27	8.32 ± 0.25	0.76 ± 0.04	2.77± 1.35
GLDAS	10.93 ± 0.05	0.81 ± 0.01	2.40 ± 1.30	11.31 ± 0.07	0.82 ± 0.01	2.50 ± 1.26	8.61 ± 0.05	0.69 ± 0.01	3.71 ± 1.27	8.09 ± 0.06	0.74 ± 0.01	2.96 ± 1.35
ERA5	12.14 ± 0.05	0.90 ± 0.01	1.04 ± 1.30	12.05 ± 0.05	0.87 ± 0.01	1.62 ± 1.26	10.63 ± 0.05	0.86 ± 0.01	1.57± 1.27	10.11 ± 0.06	0.92 ± 0.01	0.91 ± 1.35

Table 4.2: ET, ET/P, and Q/A averaged over time and space for each quadrant. Precipitation comes from TRMM. "Regression-based" indicates measurements calculated using the regression-based ET-P estimates. PT-JPL indicates measurements calculated using ET from Fisher et al. (2008).

Additionally, it has a larger range of magnitude between products than our estimates of ET as they highly depend on the ET and P estimates (from TRMM), the two largest-magnitude moisture fluxes in the Congo Basin (Burnett et al., 2020). ET estimates closer to the magnitude of P estimates result in lower mean Q/A, such as Q/A estimated from ERA5 or MODIS ET (Table 4.2). The Q/A estimates that come from our regression-based $ET - P$, as well as GLEAM and GLDAS ET estimates, indicate that the western parts of the basin have the highest mean river discharge. Higher net river discharge in the western part of the basin could be due to the higher number of rivers in that area and higher estimated daily flow (Alsdorf et al., 2016, Munzimi et al., 2019). For example, out of the 60 identified rivers from Alsdorf et al. (2016), 21 rivers lie within $Quad_{NW}$, 13 within $Quad_{NE}$, 11 within $Quad_{SW}$, 13 within $Quad_{SE}$, and 2 rivers are shared between the different quadrants. Furthermore, the part of the Congo River in $Quad_{SW}$ that outlets to the Atlantic Ocean has the highest modeled daily flow rate (Munzimi et al., 2019).

4.4 Discussion and Conclusions

A range of factors, including climate change, land use and land cover change, and more, affect the atmospheric water balance, $ET - P$. These changes can directly impact ET and/or P, or affect river discharge and terrestrial water storage (e.g. Suryatmojo et al., 2013). We confirm that mean ET is the second highest moisture flux across the basin compared to P (the highest moisture flux), river discharge, and moisture flux convergence. This indicates that a significant portion of the moisture that enters the basin undergoes high recycling (Risi et al., 2013, Sorí et al., 2022, Sorí et al., 2017, S. Worden et al., 2021). Changes in ET from climate or anthropogenic activities could therefore substantively alter the Congo water balance. For example, increased land cover and land use changes to accommodate increasing logging demands, clearing for

subsistence agriculture, and a rising need for natural resources due to population growth (Bele et al., 2015, Tyukavina et al., 2018, Kleinschroth et al., 2019, Fuller et al. 2019) can significantly alter forest composition. Frequent and large-scale fires in Africa (e.g., Andela et al., 2019, Andela and van der Werf 2014), including the Congo Basin, also change forest composition via processes such as directly removing carbon (e.g., Jiang et al., 2023), altering nutrient availability (Bauters et al., 2018; 2021), inducing soil degradation (Juárez-Orozco et al., 2017), and creating edge effects that change local energy, water, and carbon fluxes (Zhao et al., 2021). The anthropogenic fingerprint on the Congo Basin can therefore significantly affect ET in the Congo Basin and hence the future of its water cycle.

We anticipate that the Congo Basin water cycle response to climate change and land cover and land use changes may differ from that of the Amazon, where the contribution of ET to P is lower, (ET/P ~ 40-50%; Swann and Koven 2017, Xu et al., 2019, Baker et al., 2021) and anthropogenic activities differ in their extent (e.g., N'kaya et al., 2022). Furthermore, a lack of observationally-based data prevents us from understanding spatial heterogeneities in this response. This represents a key gap in our understanding of water and carbon cycle changes in the Congo Basin especially considering high spatial differences in its water cycles and vegetation (e.g., N'kaya et al., 2022, Nicholson, 2022, Burnett et al., 2020, Verheggen et al., 2012), as well as human disturbance (e.g., Jiang et al., 2023, Adams et al., 2023). Our study provides new information on quadrant-scale water flux heterogeneity; however, further research is necessary to develop new, observationally-based water flux datasets that allow us to investigate water and carbon cycle heterogeneity on smaller spatial scales.

CHAPTER 5

On the Mechanisms that Control the Rainy Season Transition Period in the Southern Congo Basin

5.1 Introduction

The Congo Basin hosts the third largest center of precipitation (P) over global land, contributing about 30% of total rainfall in Africa (Brummett et al., 2009). Precipitation in that region feeds Congo River, the world's second largest river by discharge volume, and sustains the world's second largest contiguous rainforest. Rainfall varies on interannual to decadal scales about 6-10% over the central Congo basin and up to 20% of in the outskirts of the basin (Mahé 1995; Nicholson 2022). Many previous studies have focused on the mechanisms that controls rainfall during the rainy seasons in the Congo Basin, as better understanding how these mechanisms change due to natural climatic and anthropogenic influences will lead to better understanding of how the rainy seasons will evolve in the future (e.g., Cook and Vizy 2022). However, our understanding of the mechanisms that drive the transition to the rainy season onset (RSO) has been fragmented, which, in turn, has limited our understanding of the variability of and change in the timing and length of the rainy seasons.

Previous studies point to atmospheric hydrodynamics as key controlling factors in determining seasonal rainfall (e.g., Cook and Vizy, 2022). Low-level divergence within the equatorial region during the rainy seasons contradicts the Intertropical Convergence Zone paradigm controlling seasonal rainfall (Nicholson, 2018, Yang et al., 2015). Instead, mid-tropospheric moisture transport and convergence appears to support seasonal rainfall (e.g., Cook and Vizy 2022, Longandjo and Rouault 2024). Meanwhile, low-level winds transport moisture from the Atlantic and Indian Oceans to the Congo Basin, with moisture from the Indian Ocean

the dominant contributor of the two (Dyer et al., 2017, Munday et al., 2021, Sorí et al., 2022). Evapotranspiration (ET) from local or remote sources is also a main source of atmospheric moisture for rainfall, although its contribution relative to moisture transport remain debated (Van der ent et al., 2010, S. Worden et al., 2021, Sorí et al., 2022, Pokam et al., 2012). Rising motion that uplifts this moisture, a key function for developing deep convection, is associated with regional deep and shallow Walker-like, zonal-vertical cells as well as the Congo Air Boundary (CAB; Nicholson 2022, Hastenrath 2007, Cook and Vizy 2016, Neupane 2016, Washington et al., 2013, Dezfuli, 2017, Longandjo and Rouault, 2020, Howard and Washington, 2019). The midlevel African Easterly Jet North and South (AEJ-N and AEJ-S, respectively) appear to control the meridional position of the tropical rain belt (Nicholson and Grist 2003, Kuete et al., 2020, Jackson et al., 2009, Nicholson 2022).

It is likely that the role these systems play in controlling rainfall differs between the northern and southern parts of the hemisphere, especially as most recent studies conclude that a biannual rainfall regime exists along the equatorial band, with an annual regime surrounding it (e.g., Cook and Vizy 2022, Nicholson 2022, Mba et al., 2022). The annual versus biannual rainfall regime highly depends on the area chosen for rainfall (e.g., Dezfuli, 2017). In this study, we split the Congo Basin watershed into its northern and southern counterparts along the 2° S latitude (Fig. 1a), as in Dyer et al. (2017), and extends to 15° S, the southern end of the Congo basin. We show an annual rainy season in the southern Congo domain, and a biannual rainy season in the northern Congo Basin (Fig. 5.1b), which contains most of the equatorial band. These seasonal patterns are consistent with most recent literature.

The mechanisms that control rainfall over the southern Congo Basin have not been studied as much as those over the northern Congo basin (e.g, Dezfuli, 2017). Previous studies

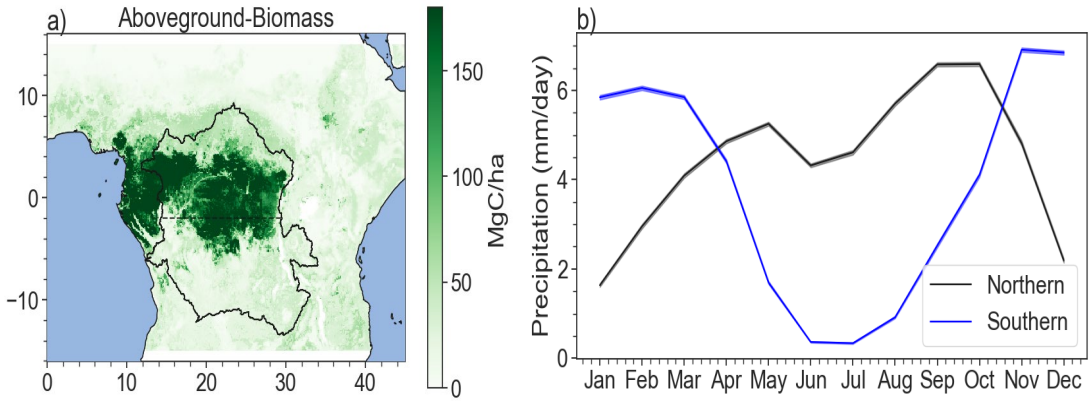

Figure 5.1: a) Aboveground biomass averaged between 2000-2019 (Xu et al., 2019). Black outline denotes the Congo Basin watershed, while the dashed line denotes the split between the northern and southern Congo; and b) climatological rainfall (calculated using monthly TRMM precipitation) for the northern and southern Congo Basin. Shades represents the standard error of the mean spatially.

have suggested that the AEJ-S, driven by the meridional temperature gradient between the Kalahari Desert and the Congo, can influence the intensity of the rain belt during August-November (Farnsworth et al., 2011). This is likely because the jet induces a mid-tropospheric convergence maximum in the right entrance quadrant of the AEJ-S, which coincides with and promotes mesoscale convective systems (MCSs) (e.g., Jackson et al., 2009). Additionally, the movement of the South Atlantic Subtropical High (St. Helena High) in July controls the formation and variability of low-level westerly/southwesterly flows, which contribute to the seasonal development of the CAB (Dezfuli 2017). The CAB brings humid air from the interior of the basin to the southern Congo, where it collides with and is lifted by relatively stable and dry air from the Indian Ocean (Levin et al., 2009, Tierney et al., 2011; Dezfuli 2017), thus promoting convection and controlling the movement of rainy belt over the southern Congo (Howard and Washington 2019, Levin et al., 2009).

Given these differences in rainfall seasonality and dynamic processes, we evaluate the thermodynamic and dynamic controls on the transition to the rainy season in the Southern Congo Basin. In addition, the sources of atmospheric moisture during the dry to rainy season transition

are unclear, especially the relative role of ET versus advected oceanic moisture within the southern Congo. Studies note that ET contributes large amounts of atmospheric moisture within the Congo Basin, although they typically investigate basin-scale or equatorial regions (e.g., Worden et al., 2021, Sorí et al., 2022, van der Ent et al., 2010). Therefore, the ET contribution within those regions is likely dominated by that from the humid, intact rainforests within its equatorial region, especially north of the equator where most of the evergreen forests are located (Burnett et al., 2020). In the southern Amazon, rainforest transpiration increases before the increase of moisture transport and the transition to the rainy season (e.g., Wright et al., 2017, Li and Fu 2004). We will investigate the role of rainforest transpiration versus oceanic moisture in changing atmospheric conditions to be more amenable to convection within the southern Congo basin during the transition period and compare the overall mechanisms of the transition period to that of the Amazon.

5.2 Data

We use satellite and reanalysis estimates in our study. We resample all data to 5-day pentads, except for the Tropospheric Emission Spectrometer (TES) data and the data we use in the random forest model due to relatively limited data points.

Satellite Data: We use the following satellite data products in our study:

-We use Tropical Rainfall Measuring Mission (TRMM) 3B43 monthly gridded P and 3B42 daily gridded P data at $0.25° \times 0.25°$ resolution between 2000-2019 that are generated using a combination of microwave and radar sensors calibrated with gauge data from the Global Precipitation Climatology Center (GPCC) (Huffman et al., 2007).

-We use the following Atmospheric Infrared Sounder (AIRS) L3 V7 daily Standard Physical Retrieval, $1° \times 1°$ gridded ascending TqJoint (as suggested by Wright et al., 2017) products

between 2003-2018: total water vapor, atmospheric-layer mass mixing ratio, surface mass mixing ratio, surface relative humidity, and atmospheric-layer temperature, surface temperature, and outgoing longwave radiation (Aumann et al., 2019, Pagano et al., 2003, Irion et al., 2018, DeSouza-Machado et al., 2018). All atmospheric-layer products utilize the H2OPressureLev or H2OPressureLay 12 standard pressure levels.

-We use the Clouds and the Earth's Radiant Energy System (CERES) Syn1deg Ed 4.1 $1° \times 1°$ gridded daily cloud top temperature, cloud top height, cloud area fraction (total, high, mid-high, mid-low, and low), downward surface solar radiation flux (all-sky, clear sky, and pristine sky), and insolation. This product incorporates derived fluxes from geostationary satellites (GEOs) to constrain global energy budget data computed by using the Fu-Liou radiative transfer model based on observed cloud and aerosol distributions. (Doelling, et al., 2013, Doelling et al., 2016, Su, et al., 2005, Rutan et al., 2015, Wright et al., 2017).

-We use the Moderate Resolution Imaging Spectroradiometer (MODIS) MOD08_D3_6_1 daily $1° \times 1°$ 550 nm gridded aerosol optical depth (AOD) between 2004-2018 collected from the Terra platform, and MYD08_D3_6_1 daily $1° \times 1°$ cloud optical thickness (COT) product between 2003-2018 collected from the Aqua platform (Chu et al., 2002, Wan 2008, Platnick et al., 2016). MODIS COT is derived using spaceborne spectral imaging to identify spectral contrast of cloud single scattering properties (Meyer et al., 2015).

-We use a 4-day averaged, $0.05° \times 0.05°$ continuous daily solar-induced fluorescence product (SIF) product between 2003-2016 estimated by combining MODIS and Orbiting Carbon Observatory-2 (OCO-2) in a neural network (Zhang et al., 2018). We re-bin this data into 5-day pentads.

-We use the Global Fire Emissions Database, Version 4.1 (GFEDv4.1) 0.25×0.25 °daily burned area product available between 2000-2015. This product is produced by combining 500 m MODIS burned area maps with active fire data from the TRMM, the Visible and Infrared Scanner (VIRS), and the Along-Track Scanning Radiometer (ATSR; Randerson et al., 2018, Giglio et al., 2013).

-We use the Global Land Evaporation Amsterdam Model (GLEAM) v3.7b $0.25 \times 0.25°$ daily land ET and soil moisture products between 2000-2019. ET products are estimated using the Priestly Taylor model, while soil moisture is estimated by assimilating soil moisture observations into a water balance model (Martens et al., 2017, Miralles et al., 2011).

- Annual, $0.1 \times 0.1°$ aboveground biomass between 2000-2019 is estimated by Xu et al. (2021) using a combination of lidar, global modeling, and satellite data. The following steps were taken to produce these estimates: 1) Ground inventory plots (>100,000 in number) are integrated with airborne and satellite data, with models used to relate lidar-derived metrics and radar backscatter to above-ground biomass (AGB) estimates from ground plots; 2) Spatially aggregated samples of woody vegetation AGB mean and variance at 10-km spatial resolution are developed using satellite and airborne lidar as training data; and 3) AGB is estimated by using the training data in spatial-temporal machine learning models. The satellite data used in the process come from the Ice, Cloud, and land Elevation Satellite (ICESAT), the Shuttle Radar Topography Missions (SRTM), the Advanced Land Observing Satellite (ALOS), Landsat, the Moderate Resolution Imaging Spectroradiometer (MODIS), and QuikSCAT (QSCAT). More details on this product can be found in Xu et al. (2021).

-We use the version 6 (v006_Litev01.00) daily Level 2 free-tropospheric deuterium (HDO) and H_2O measurements from the NASA Aura TES satellite instrument. The following quality flags

were used when retrieving the data from the TES satellite: “Species Retrieval Quality = 1,” “Degrees of Freedom for Signal >1,” and “Average Cloud Optical Depth <0.4” in order to ensure good quality data as suggested by Worden et al. (2012). The accuracy of these data is ~6 per mil with a precision of 20 per mil (Worden et al., (2012) for the vertical range used in this analysis (~900-420 hPa, or about 1-6 km above sea level). We use data between 2005-2011 when the quality of estimates is suitable for our analysis (Worden et al., 2021). We use daily HDO and H_2O measurements in this analysis instead of pentad measurements as the number of observations is limited compared to the other products.

Reanalysis Estimates: We use the fifth-generation of the European Centre for Medium-Range Weather Forecasts (ECMWF) ERA5 hourly resampled to daily gridded $0.25° \times 0.25°$ resolution atmospheric reanalysis product between 2000-2018: zonal and meridional (u and v) winds, vertically integrated moisture flux convergence, vertical integral of eastward total water vapour flux, vertical integral of northward total water vapour flux, vertical velocity, divergence, and specific humidity. The reanalysis combines observations with model forecasts to estimate dynamic and thermodynamic atmospheric quantities (Hersbach et al., 2020).

5.3 Methods

5.3.1 Calculating the Onset of the Fall Rainy Season

We calculate the onset of the fall rainy season in the southern hemispheric Congo Basin similar to that in Chakraborty et al. (2021) and Li and Fu (2004). This definition is designed to capture persistent high rainfall during the rainy season and persistent low rainfall in the dry season using the annual mean rainfall as the threshold. We first calculate the climatological pentad (5 day)-mean rainfall for each year over our domain. We then find the first pentad of each year that meets the following criterion: seven out of the previous nine pentads are less than the climatological

annual mean, and seven out of the following nine pentads are more than the climatological annual mean. Figure 5.2 shows the RSOs between the years 2000-2020 based on the TRMM pentad data. The RSO date ranges from the 51st to 62nd pentad (with Days 1-5 defined as Pentad "0"), corresponding to mid-September to early November. On average, the RSO occurs on pentad 56, or October 8, for the period of 2000-2020. We define different phases of this transition based on the changes of the key processes that drive the dry to rainy season transition as in Li and Fu (2004) and Wright et al. (2017). Climatological seasonal evolutions are based on their time relative to the RSO of each year, and averaged over 46 pentads before the RSO (the "0" within the plots) and 7 pentads after the RSO

5.3.2 Thermodynamic and Dynamic Equations

We calculate area mean equivalent potential temperature (θ_e) from AIRS gridded data at daily

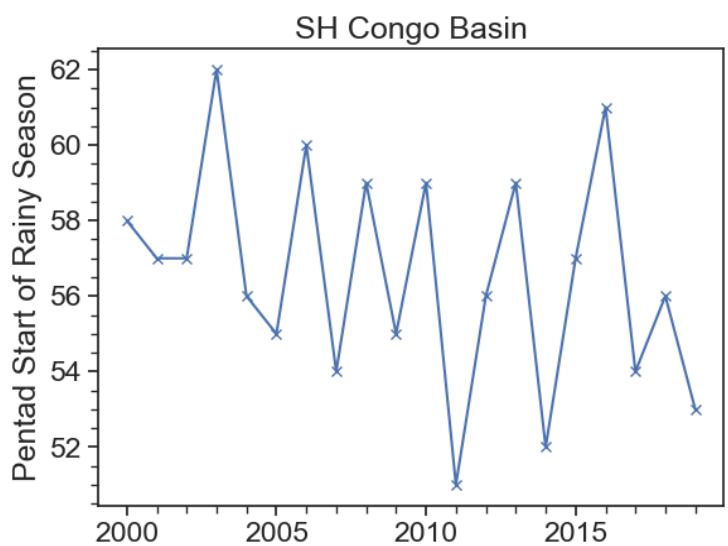

Figure 5.2: Pentad start date of the rainy season for the southern Congo Basin for each year between 2000-2020.

time resolution to examine atmospheric instability during and after the transition to the rainy season. We calculate θ_e using the following equation from Bolton (1980):

$$\theta_e = T_k \left(\frac{1000}{p}\right)^{0.2854(1-0.28\times10^{-3}*r)} \times exp\left[\left(\frac{3.376}{T_L} - 0.00254\right) \times r(1 + 0.81 \times 10^{-3} r)\right]$$

(Eq 5.1)

Where T_k is the absolute temperature (K), p is pressure (hPa), r is the mixing ratio (g/kg), T_L is the absolute temperature at the lifting condensation level (K) calculated by the following:

$$T_L = \frac{2840}{3.5lnT_k - lne - 4.805} + 55 \quad \text{Eq 5.2}$$

Where $e = \frac{p*r}{622+r}$ is the water vapor pressure. We use the AIRS mass mixing ratio, temperature, and pressure in these calculations.

We calculate vapor pressure deficit (VPD) using the saturated vapor pressure (e_s) and relative humidity (RH):

We calculate e_s as in Bolton (1980):

$$e_s = 6.112exp\left(\frac{17.67T}{T+243.5}\right) \quad \text{Eq 5.3}$$

Where T is the temperature in $°C$. We calculate VPD as:

$$VPD = e_s \times \left(1 - \frac{RH}{100}\right) \quad \text{Eq 5.4}$$

Finally, we examine moisture flux transport and convergence by the following:

We examine vertically integrated from the surface to top of atmosphere moisture flux (MF), or the vertical integral of q, specific humidity times **V=(u,v),** the zonal or meridional winds integrated from the surface to the top of the atmosphere. We examine the zonal MF (integral of q*u) across the western and eastern boundaries, and the meridional MF (integral of q*v) across the northern and southern boundaries. For simplicity, we approximate the boundaries of the southern Congo Basin to straight lines. The northern boundary is across $2°S$ and between

$14.5 - 34°E$. The southern boundary is across $15°S$ and between $14.5 - 34°E$. The western boundary is across 14.5° E and between $2 - 15°S$. The eastern boundary is across 34 E and between $2 - 15°S$.

We additionally calculate the moisture convergence term (-$q \times \nabla . V$) and moisture transport vectors (qV) at four pressure levels to represent near surface, lower-troposphere, mid-troposphere, and upper troposphere, respectively: 925 hPa, 850 hPa, 700 hPa, and 650 hPa, similar to that in Cook and Vizy (2022) and Nicholson (2022). This is because moisture transport varies substantially between near surface atmosphere, lower troposphere, and middle troposphere, including its source regions.

5.3.3 Identifying Deep Convection Using OLR

Typical deep convective clouds in the Congo Basin are higher than 12 km (e.g., Hosking et al., 2010, Sohn et al., 2015, Chakraborty et al., 2020) with cloud top temperatures (CTTs) less than $-40°\ C$ (Hart et al., 2019), and outgoing longwave radiation (OLR) below 240 K (e.g., Hosking et al., 2010, Okoola et al., 1998). We calculate the fraction of longwave radiation below 240 K in each grid cell before averaging over the southern Congo to help isolate the deep convective signal (Murakami 1980; Lau and Chan 1983; Fu et al. 1990). However, the observations of cloud top height (CTH), CTT, and OLR at each grid cell are inclusive of clear sky conditions, different cloud types, and on time scales greater than that of individual deep convection events. Therefore, while CTH, CTT, and OLR are useful metrics to indicate deep convection during individual events, we use this data only to show change of deep convection qualitatively.

5.3.4 Random Forest Feature Importance

We examine the seasonal controls on GLEAM-based ET during the transition period using a random forest regressor model from the python sklearn module. We defined the model to have 100 estimators or trees in the forests, at least 5 samples required to be at a leaf node, and controlled for randomness (n_estimators = 100, min_samples_leaf = 5, and randoms_state = 42). GLEAM-based ET is a modeled product that incorporates radiation, P, air temperature, vegetation optical depth, soil moisture, land cover fractions, soil properties, lightning frequency,

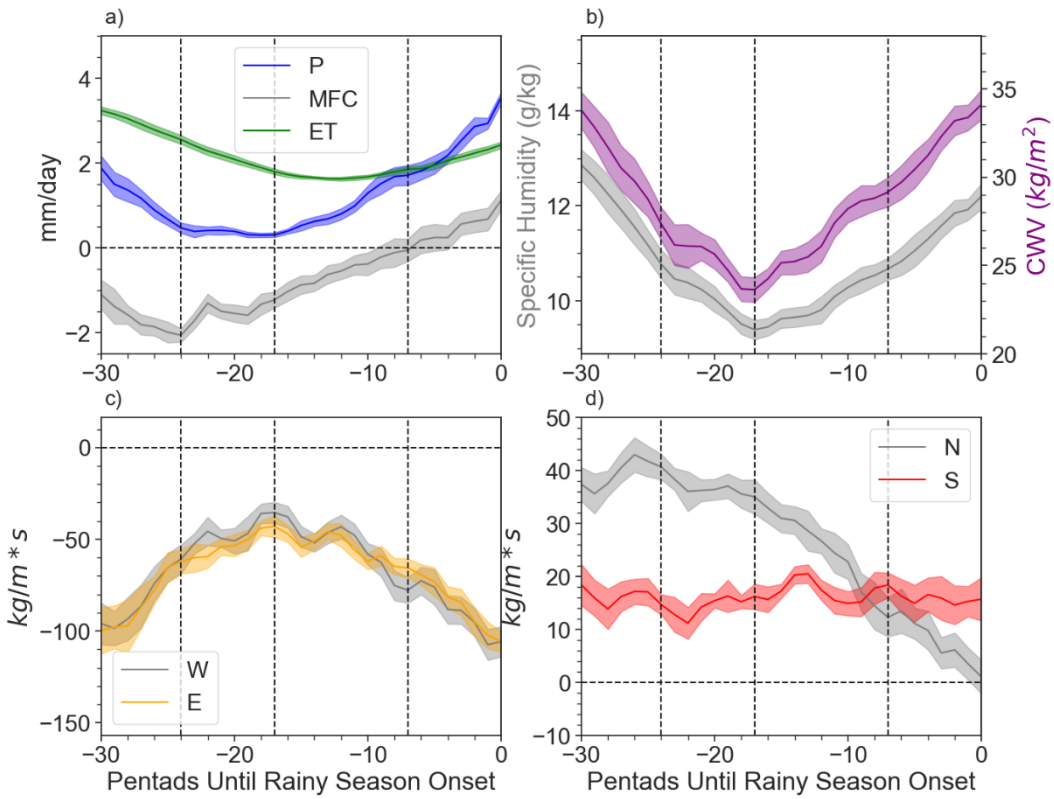

Figure 5.3: a) Precipitation (P), vertically integrated moisture flux convergence (MFC), and evapotranspiration (ET) b) surface specific humidity and column water vapor (CWV); c) zonal vertically integrated moisture flux (MF) across the western (W) and eastern (E) rough boundaries (Methods); and d) meridional MF across the northern (N) and southern (S) rough boundaries (Methods). All are relative to the RSO (denoted as 'O' in the graph). Negative pentads (5-day averages) indicate times prior to the RSO and positive pentads indicate times after the RSO. Shades represents the standard error of the mean of the different years. Time series have been smoothed using a Savitsky-Golay filter (number of coefficients: 5, polynomial order 2).

and snow-water equivalent (Martens et al., 2017). The influence that each forcing exerts on predicting ET may change throughout the year. Therefore, we test the influence of shortwave solar surface radiation (SSRD), VPD, and soil moisture on ET during entire the transition period by using a random forest model to test for feature importance. We will use this model to help identify whether ET in the Southern Congo Basin is more controlled by radiation, atmospheric demand for moisture, or water availability via soil moisture during the dry to rainy transition period (Fig. 10). We use 80% of the data as a training dataset, and test model performance using the remaining 20%. We then calculate the feature importance, based on mean decrease in impurity (Breiman 2001), on the training dataset. We test the model performance using the mean squared error (MSE) and coefficient of determination (R^2). In addition, we check for overfitting by comparing the MSE and R^2 of the train dataset to the MSE and R^2 of the test dataset.

5.4 Results

We identify three transition periods meant to capture significant developments of atmospheric moisture key towards supporting the transition to the RSO. The first period, the pre-transition season, (24-17 pentads before the RSOs), is chosen to capture the turning point in vertically integrated moisture flux convergence (MFC; negative represents divergence; Fig. 5.3a) at the beginning. The turning point in MFC from most divergent to heading towards convergence means that the atmospheric circulation is changing induce wetting conditions over the southern Congo Basin. Meanwhile, the "early-transition" period (17-7 pentads before the RSOs) is chosen to capture the turning point in atmospheric water vapor from decreasing to increasing (Fig. 5.3b), which means that the atmospheric conditions have changed from seasonal drying to seasonal moistening. Finally, the "late-transition" period (7-0 pentads before the RSOs) starts when MFC becomes convergent for the first time. In the following sections, we identify key changes in the

atmospheric dynamic and thermodynamic conditions, as well as key energy and water fluxes, in the context of each transition period to elucidate the mechanisms controlling the transition period the RSO.

5.4.1 Pre-Transition

To examine changes in atmospheric moisture as signified by the turning point in MFC, we evaluate MF (Fig. 5.3 b,c) along four boundaries of the southern Congo as described in the Methods section. In addition, we compare moisture transport and convergence in the near surface (925 hPa), lower troposphere (850 hPa), and the lower-mid troposphere (750 hPa) during the 30 days before the pre-transition ("before" period) and the early-transition period (Fig 5.4). Fig. 5.3 c and d indicates that the change in MFC is initiated by a decrease in the net amount of moisture leaving the basin through its northern boundary. Moisture transported through the northern boundary of the southern Congo in the mid-troposphere (750 hPa), while net divergent towards the Sahel, decreases in strength between the "before" period and the pre-transition period (Fig 5.3d, Fig 5.4 Fig 5.4 e,f). We can explain this change in moisture transport by examining the surface temperature gradients within the area. During the pre-transition period, surface temperature increases within the southern Congo, which then weakens the larger-scale temperature gradients between the (cooler) southern Congo and the (warmer) Sahel. Therefore, this weakens moisture transport out of the southern Congo as more moisture stays within the region. Otherwise, conditions remain representative of the season dry season. ET and SIF decrease (Fig. 5.6a), as expected from decreasing insolation (Fig. 5.6b), increases in low clouds (Fig. 5.6d) and AOD from seasonal biomass burning (Figs. 5.6b, 5.6e). Therefore, ET does not contribute much to atmospheric moisture ($f_{mix} = 0.262 \pm 0.119$, Fig. 5.7a). Increases in VPD (Fig. 5.6c) and decreases in soil moisture (Fig. 5.6a) indicate continued drying of the land

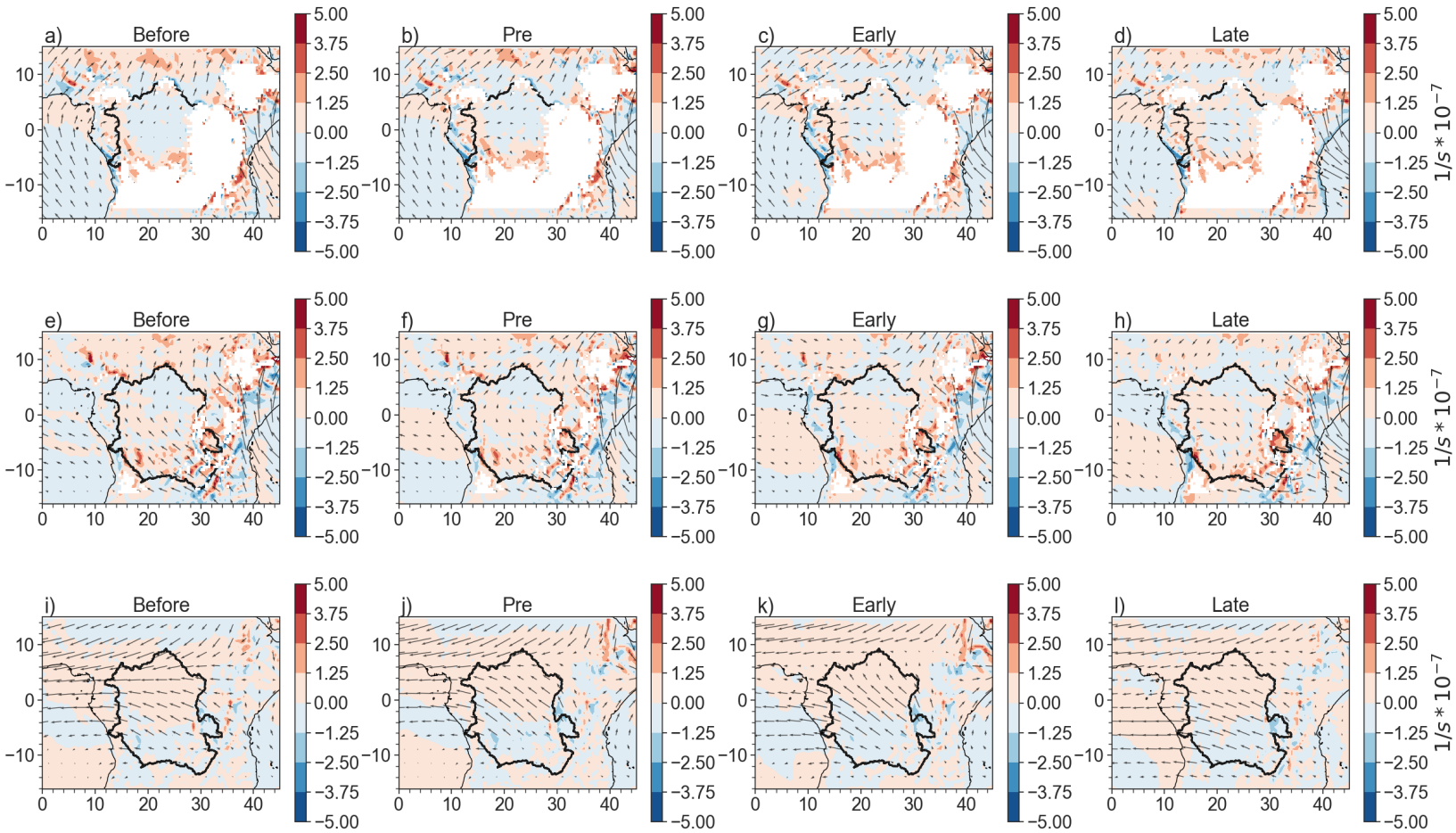

Figure 5.4: Moisture convergence term (q*∇.v) and moisture transport vectors (qv) for: a-d: 925 hPa; e-h: 850 hPa; and i-l: 700 hPa. "Before" represents 30 days (6 pentads) before the pre-transition period. White shades represent topography above the pressure level at hand.

surface. Increases in surface sensible flux and temperature (Fig. 5.8a) facilitate dry convection in the atmospheric boundary layer up to ~750 hPa (Figs. 5.8d), where a strong layer of subsidence prevents further rising motion (Fig. 5.8e) and hence deep convection. The AEJ-S has not formed yet, as indicated by a lack of strong zonal winds at 650 hPa (Fig 5.9a) and low zonal wind shear between 925 and 650 hPa (Fig. 5.9b). The high convective inhibition energy (CIN) and low convective available potential energy (CAPE; Fig. 5.8c) indicates stable thermodynamic conditions unfavorable for deep convection, leading to relatively high CTTs and low CTHs, the fraction of OLR<240 Wm^{-2} staying near zero, and decreases in atmospheric instability (Figs. 5.8b, c, d).

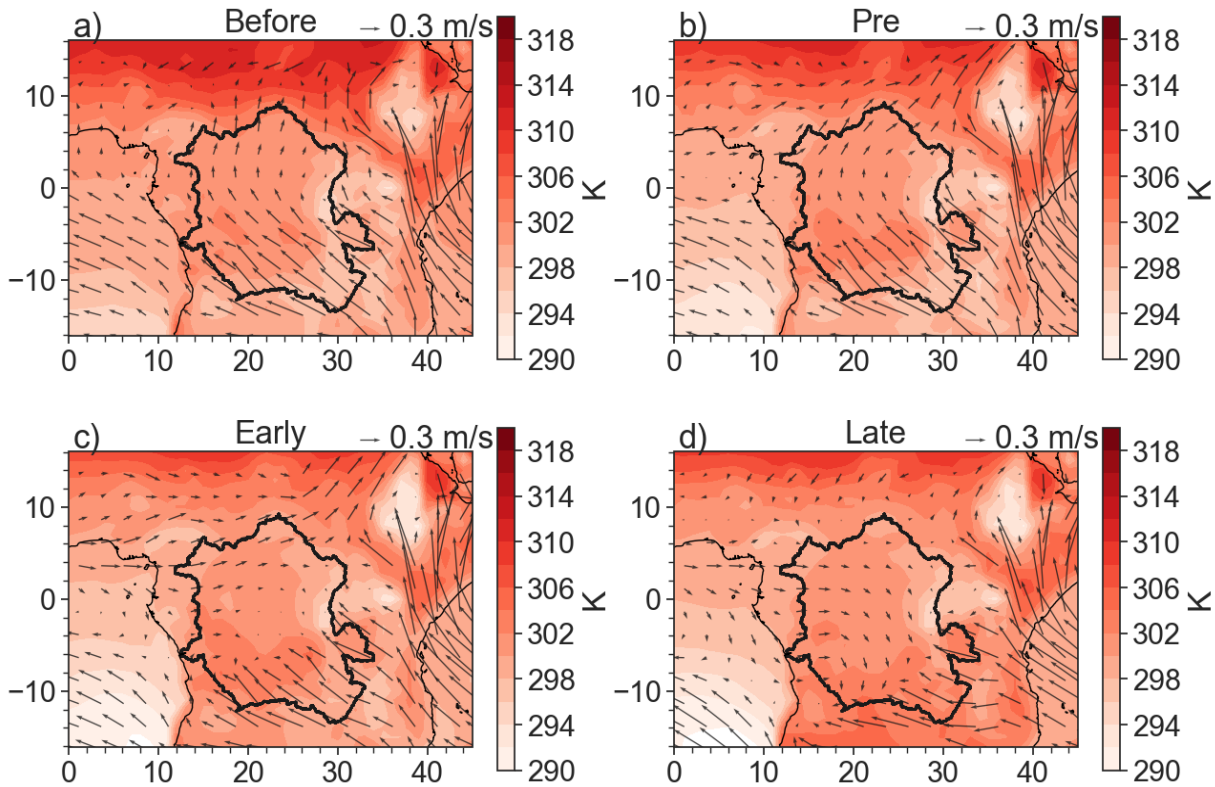

Figure 5.5: Surface temperature and 850 hPa horizontal winds. "Before" period is 6 pentads (30 days) before the start of the pre-transition period.

5.4.2 Early-transition

The early-transition period marks the beginning of the change from seasonal drying to seasonal moistening, as indicated by increases in surface specific humidity, column water vapor (CWV), and P first, followed by increases in ET toward the end of this period (Fig. 5.3 a, b). MFC is still divergent, although this divergence weakens and becomes convergent at the end of this period. This change in divergence is reflected by the following changes in moisture across the northern boundary (Fig. 3c, d). which continues to decrease. However, it is still greater than moisture entering the basin through its southern boundary such that moisture is still net divergent for most of the period meridionally. By the end of the early-transition period, more moisture enters the basin across its southern basin than the northern basin, but slightly more moisture

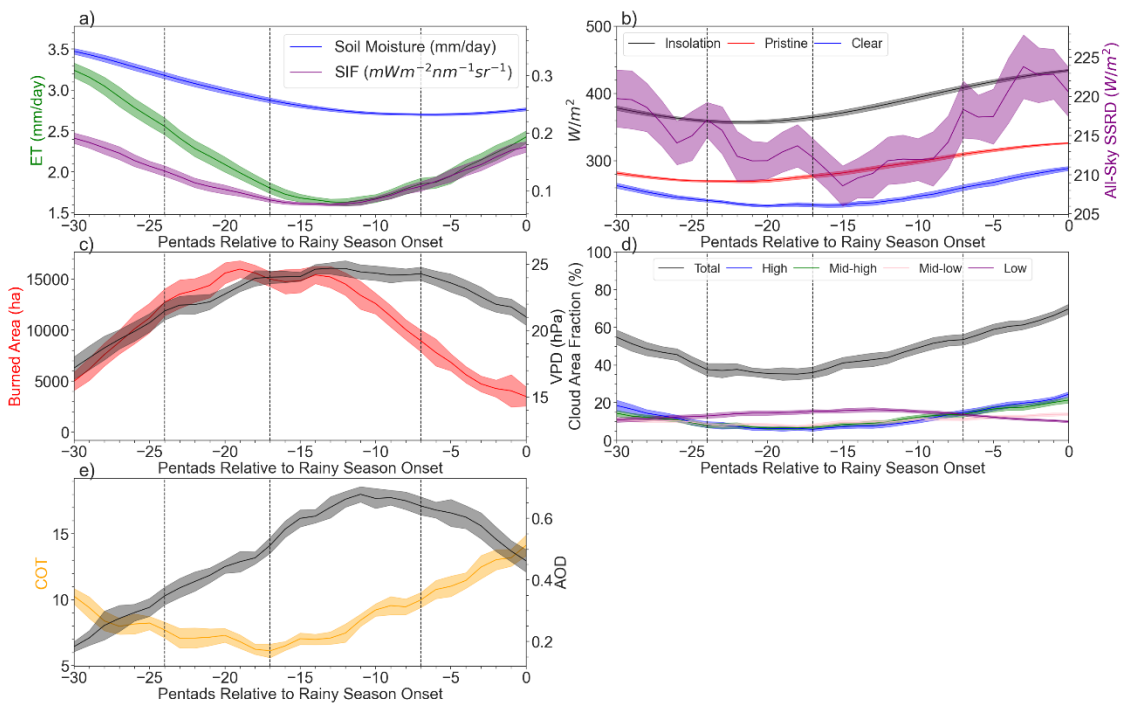

Figure 5.6: a) Evapotranspiration (ET), rooting-depth soil moisture, and solar-induced fluorescence (SIF); b) Insolation and pristine, clear, and all-sky surface solar radiation downwards; c) burned area and vapor pressure deficit (VPD); d) total, high, mid-high, mid-low, and low cloud area fraction; and e) cloud optical thickness (COT) and aerosol optical depth (AOD) relative to the RSO. Shades represents the standard error of the mean of the different years. Time series have been smoothed using a Savitsky-Golay filter (number of coefficients: 5, polynomial order 2).

leaving the basin across its western boundary compared to its eastern boundary, thus explaining the weak divergence in MFC.

At the near surface (925 hPa), the amount of moisture transport coming from the Atlantic Ocean, going through the humid northern Congo, and turning into the southern Congo, increases (Fig. 5.4b,c). This meets with the relatively dry and cold air from the Indian Ocean and southern Africa at the CAB (Fig. S2b). Therefore, the fraction of moisture traced back to plant transpiration ($f_{mix} = 0.361 \pm 0.137$) increases (Fig. 5.7b), likely from a combination of local increases in ET (Fig. 5.3a) and ET brought into the region from the near-surface (Fig. 5.4c). However, oceanic moisture is still the main contributor to atmospheric moisture during this time.

All of these changes together destabilize the lapse rate (Fig. 5.8d), especially in the lower troposphere, which, in turn, increases CAPE and reduces CIN (Fig. 5.8c) for moist convection. Because moisture divergence still dominates the mid-troposphere (Fig. 5.4k), and subsidence

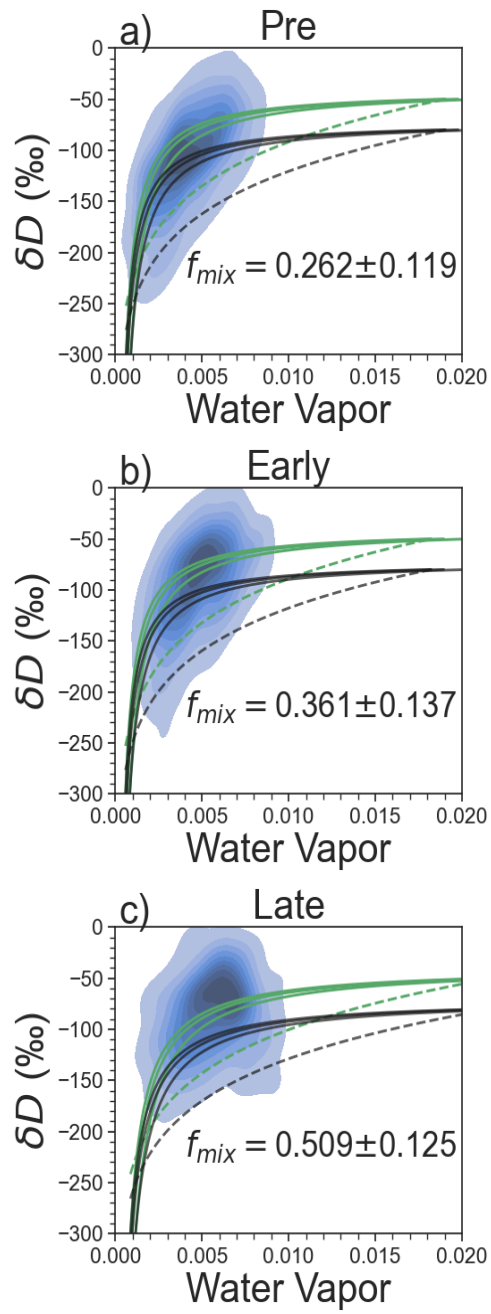

Figure 5.7: Fraction of observed above a series of mixing (solid) and Rayleigh (dashed) models. Green indicates land-based water vapor models, while black indicates ocean-based water vapor models. f_{mix} is the fraction of observed δD above the uppermost, land-based mixing model. For a) the pre-transition; b) the early-transition; and c) the late-transition.

prevents vertical uplift to the upper atmosphere (Fig. 5.8e), the increase of thermodynamic instability mainly increases and deepens shallow convection (Fig. 5.8d).

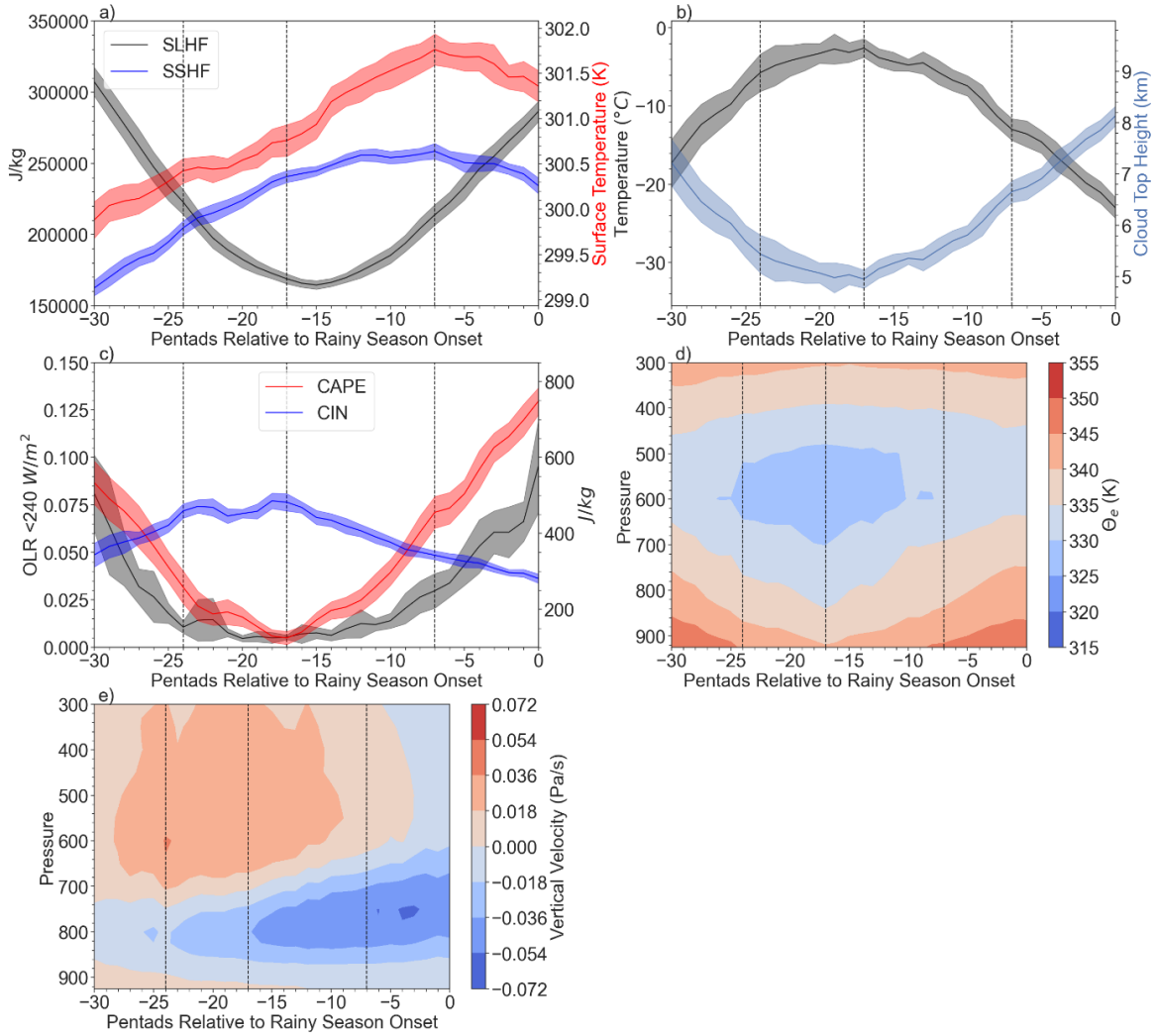

Figure 5.8: a) Surface temperature, surface latent heat flux (SLHF), and surface sensible heat flux (SSHF); b) cloud top temperature (CTT) and cloud top height (CTH); c) convective available potential energy (CAPE) and convective inhibitive energy (CIN), and fraction of $OLR < 240\ W/m^2$; d) equivalent potential temperature (θ_e); and e) vertical velocity (negative means upward motion) all relative to the RSO. Shades in the time series represents the standard error of the mean of the different years. Time series have been smoothed using a Savitsky-Golay filter (number of coefficients: 5, polynomial order 2).

We further examine the mechanisms controlling the increase in SIF and ET during the second half of this transition period, which follows increases in P (Fig. 5.3a), increases in surface temperature (Fig. 5.8a), and precedes increases in soil moisture (Fig. 5.6a). Additionally, VPD

does not significantly change during this time (Fig. 5.6c). Therefore, increases in surface radiation during the second half of this period (Fig. 5.6b) are likely responsible for the turning

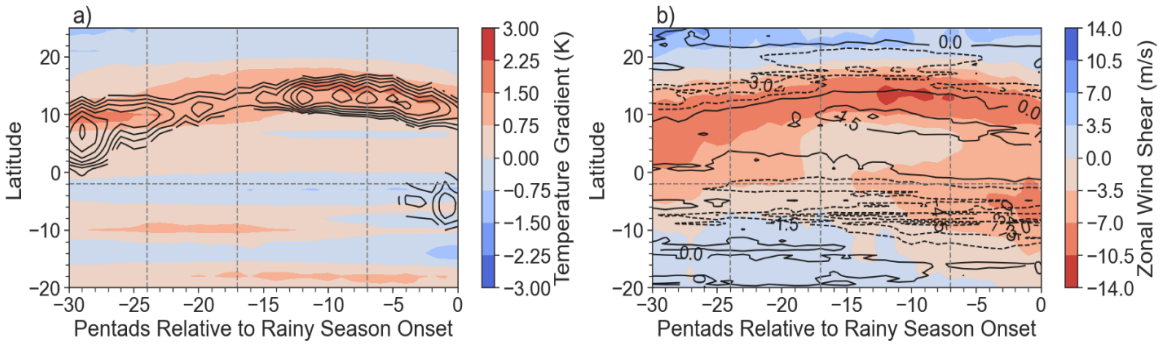

Figure 5.9: a) Shaded contours: meridional surface temperature gradient; black contours: 650 hPa zonal wind speeds >6 m/s to show the evolution of the AEJ-N (top contours) and AEJ-S (bottom contours); and b) Shaded contours: zonal wind shear (650-925 hPa); grey contours: moisture divergence (q*DIV $\times 10^8$, units: $1/s$) at 650 hPa. Negative (dashed contours) indicates divergence.

points in ET and SIF. We explain this control as follows: We explain this radiation control on ET as follows: During the early transition, COT increases to ~10, following maximal low cloud cover and increases in high and mid-level clouds (Fig. 5.6 d,e). Meanwhile, AOD reaches a maximum of 0.7, despite decreases in biomass burning within the southern Congo (Fig 5.6 c, e). This could be due to transport of non-local African biomass burning emissions as areas of high biomass burning emissions seasonally shift from west to east in southern Africa (Val Martin et al., 2018, Duncan et al., 2003). Therefore, surface radiation reaches its minimum, mainly due to the increase of COT and to a lesser degree, the increase of AOD. This corresponds to decreases in ET. However, insolation, which has been increasing since the pre-transition period and can act to increase surface radiation, finally outpaces those decreases in surface radiation from clouds and aerosols. Vegetation responds with increased photosynthesis and ET in the second half of the early-transition.

We confirm the importance of seasonal changes in radiation, rather than water-related metrics (soil moisture, which represents the amount of water available for transpiration below the

surface and VPD, which represents atmospheric demand for moisture) using a random forest to predict ET and then computing its feature importance to examine which predictor was most important for prediction. Our model performs well in predict ET, with $MSE = 0.02$ and $R^2 = 0.60$ in the test dataset (Methods). The feature importance (Fig. 5.10) indicates that radiation was the most important for predicting ET, thus confirming our results indicating that radiation is a key feature. This seasonal radiation control on ET is consistent with prior studies (e.g., Burnett et al., 2020, Liu et al., 2020).

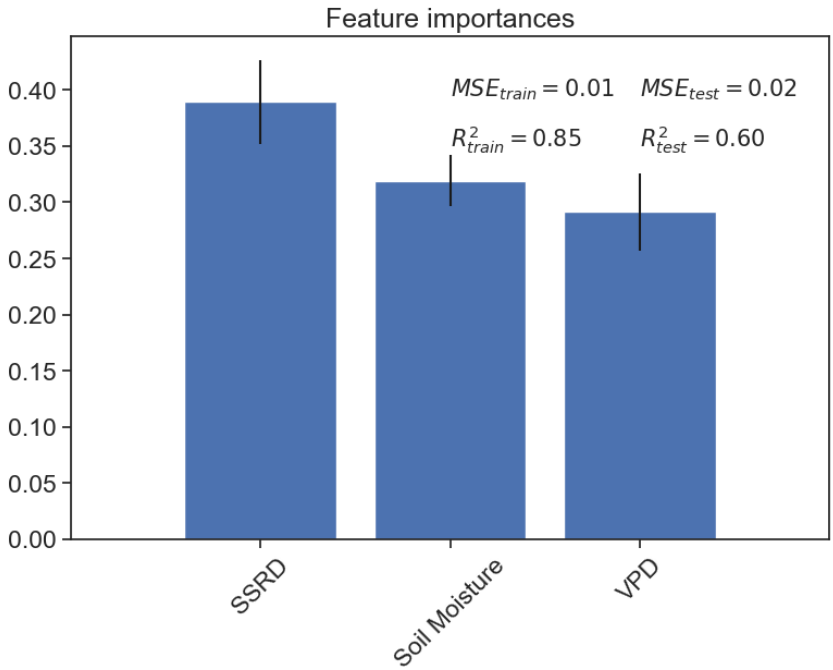

Figure 5.10: Feature importances of the three predictors used to estimate ET using a random forest model: SSRD, soil moisture, and VPD.

5.4.3 Late Transition

During the late transition period, ET and P and MFC (now convergent) continues to increase (Fig. 5.3a). This increase in MFC is due to further decreases in moisture leaving the basin through its northern boundary such that moisture entering the basin through its southern boundary is larger (Fig. 5.3d). This is primarily due to moisture changes in the lower

troposphere: Moisture transport from the Atlantic Ocean that moves through the northern Congo before reaching the south now reaches up to 850 hPa instead of being confined to the near surface (925 hPa) as in the previous periods (Fig. 5.4 c, d, g h). Mean while, This overtakes moisture divergence out of the northern boundary towards the Gulf of Guinea at 750 hPa decreases, reflective of changes in moisture transport by the return branch of the Congo Basin Cell (Longandjo and Rouault 2020).

Increases in lower-troposphere moisture contributes just as much as ET to atmospheric moisture: the fraction of atmospheric moisture from plant transpiration increases rapidly ($f_{mix} = 0.509 \pm 0.125$, Fig. 5.7c). As the CAB moves further south into the region (Fig. S2c), it lifts this low-level moisture to the mid-level, which is then transported by deep convection to the upper levels of the atmosphere (300 hPa) for the first time during the transition period (Fig. 5.8e). These changes rapidly increase CWV and so P (Fig. 5.3 a, b). In addition, the newly-formed AEJ-S induces zonal vertical shear in the lower and mid-troposphere (Fig. 5.9b). Therefore, this rapid destabilization of the atmosphere combined with large increases in atmospheric convergence and moisture create atmospheric conditions conducive for the more frequent formation of deep convective systems, especially MCSs. This is corroborated by increases in cloud area fraction to nearly 80% (Fig. 5.6d), rapid increases in surface latent heat flux and decreases of surface sensible heat flux, CAPE largely over taking CIN (Fig 5.8c), increases in CTHs (decreases in CTTs); Fig 8b), and increases in atmospheric instability ($\frac{d\theta_e}{dp} < 0$) higher up within the atmosphere (Fig. 5.8d). Therefore, the frequency of MCSs begins to increase, as shown by increases in the fraction of $OLR < 240\ W/m^2$, with this fraction sharply increasing after the start of the rainy season (Fig. 5.8c). These conditions indicate the completion of the atmospheric dynamic and thermodynamic evolution to make conditions favorable for the RSO.

5.5 Discussion

5.5.1 Comparing dry-to-rainy season transitions between the Southern Congo and Southern Amazon

Both Southern Congo and Southern Amazon are in the humid tropical continents. To facilitate a general understanding of dry-to-rainy season onset in this climate regime, we briefly compare the similarities and differences in the dry to rainy season transition periods in the Southern Congo versus Southern Amazon. Both regions feature increasing moisture and thermodynamic instability in the lower troposphere during the transition period (Li and Fu 2004, Fu et al., 1999), which leads to increases in shallow convection (Wright et al., 2017). Increasing ET plays a key role in providing atmospheric moisture prior to the RSO (Wright et al., 2017, Li et al., 2006). Fronts between warm/humid tropical air and dry/cold air from the extratropics provide dynamic lifting for large-scale onset of deep convection. In the southern Congo basin, humid air from the interior Congo meets drier air from South Africa along the CAB (Howard and Washington, 2019). In the Amazon, this takes the form of cold fronts moving into the region from mid latitude South America (Siqueira et al., 2005, Li and Fu 2006). Overall, both areas are likely sensitive to climate and land cover and land use changes (e.g.,Vancutsem et al., 2021) that affect ET and hence forest ability to regulate their own water cycles (e.g., Wright et al., 2017, Heiblum et al., 2014, te Wierik et al., 2021).

However, we note some key differences in the mechanisms that control this transition. In the Southern Amazon, ET increases first, initiating shallow convection. The latter preconditions the atmosphere for deep convection. The latent heating generated by deep convection drives large scale moisture convergence (e.g., Li and Fu 2004; Wright et al., 2017). In the Southern Congo, moisture divergence weakens first, which increases lower tropospheric humidity, inducing atmospheric conditions amenable to shallow convection. Then, increases in surface

solar flux, mainly driven by increase of insolation, leads to ET increases. The latter works in concert with moisture convergence to provide the moisture needed to fuel deep convection by the end of the late transition period. Thus, the relative contribution of ET versus advected oceanic moisture is strongest in the late transition in the Southern Congo, instead of in the early transition as in the Southern Amazon (Wright et al., 2017).

Differences in key dynamical systems that control rainfall evolution exist as well. In the Southern Amazon, moisture is provided by ET in the equatorial western Amazon, transported by the South American Low-Level Jet to the Southern Amazon (Wright et al., 2017). In the Southern Congo, key dynamical systems are low level winds and the mid-tropospheric AEJ-S. Moisture from two oceans reaches the interior via low-level westerlies from the Atlantic, and easterly low-level jets through the East African Rift (Pokam et al., 2012, 2014, Munday et al., 2021). Furthermore, the AEJ-S provides the dynamic conditions conducive for MCS formation by inducing uprising motion and vertical wind shear (Jackson et al. 2009; Adebiyi and Zuidama 2016, Fig. 8). In addition, the mid-tropospheric meridional moisture convergence to the north of the AEJ-S entrance (Jackson et al., 2009) is suggested to be important for convection in the Congo basin. The causes of this mid-tropospheric moisture convergence include the divergent flow of the mid-tropospheric high above the Kalahari Low (e.g., Nicholson and Grist 2003, Pokam et al., 2012, Washington, 2013, Kuete et al., 2020), or the CAB (Longandjo and Rouault 2020, 2023). We show mid-tropospheric divergence at 600 hPa within the southern Congo but mid-tropospheric convergence within the northern Congo (Fig 5.9b). Thus, this mid-tropospheric convergence is probably less important for the southern Congo basin than for the seasonal evolution of atmospheric conditions over the northern Congo.

Finally, the role each region plays in moisture recycling is likely different. Recycled moisture can travel 100-1000 km over timescales of days (van der Ent et al., 2010), thus enhancing rainfall downwind. Transpiration from the Southern Amazon acts as a source of moisture for other regions (e.g, Staal et al., 2018). We cannot qualitatively say where moisture produced via transpiration comes from over the southern Congo. The abrupt jump in ET contribution to atmospheric moisture (Fig 5.5c) in the late transition period does coincide with increased low-level winds traveling over the moisture-laden, tropical rainforest-heavy northern Congo. Furthermore, the southern Congo Basin domain only contains a small part of the tropical rainforests, and instead features mixed forest with some grassland areas (e.g., Sorí et al, 2017). Plant transpiration is thus lower and likely contributes less to atmospheric moisture compared to that in the equatorial tropical region (Worden et al., 2021). We therefore hypothesize that the southern Congo acts as a sink for transpired moisture from the northern Congo Basin, and that the sharp jump in ET contribution is due to a combination of local and remote sources.

5.5.2 Role of Biomass Burning on Affecting Water and Energy Cycles

We show that the balance between cloud cover and insolation is the dominant control on radiation available for ET during the transition period. AOD with a maximum ~0.6, which indicates very heavy pollution, is small compared to the change of COT. Therefore, this has a limited impact on surface radiation. This appears to be different from the conclusion of Chakraborty et al. (2021), which shows that early RSO years over the entire Congo Basin (10ºS-5ºN) are induced by higher aerosol concentrations in June, which act to decrease radiation and surface temperature. Such an effect increases the meridional surface temperature gradient between the Congo and the Kalahari Desert, which in turn, leads to the early formation of the AEJ-S and hence the RSO. One possible explanation for such apparent discrepancy is that the

southern Congo basin has strong seasonal change of COT, probably more than that of northern Congo basin that is included in Chakraborty et al. (2021). As such, the radiative effect of clouds on surface solar radiation, as inferred from COT, is more than an order of magnitude larger than that of aerosols, as inferred from AOD. Also, we do not consider dust in our study since previous studies do not show dust intrusions into our region during the time period that we examine (Schulz et al., 2012). However, dust plays a more important role in changing the energy budget in the northern Congo (Chakraborty et al., 2021).

Additionally, previous studies suggest that increasing concentrations of carbonaceous aerosols over tropical Africa, primarily from transport to the equator from fires north and south of the Congo Basin (Roberts et al., 2009, Bauters et al., 2018), can reduce rainfall via increasing atmospheric stability, drying the local atmosphere, changing cloud microphysics, and changing surface energy fluxes (e.g, Kawase et al., 2011, Tosca et al., 2013, Tummon et al., 2010, De Sales et al., 2019, Hodnebrog et al., 2016, Tosca et al., 2015, Jiang et al., 2023, Hodnebrog et al., 2016). These semi-direct and indirect aerosol effects are not accounted for in our analysis, but they are likely minor compared to the effects of changing thermodynamic and dynamic conditions of the atmosphere.

5.6 Conclusion

Using a suite of satellite and reanalysis data, we found the following mechanisms central for the transition to the rainy season in the southern Congo Basin:

(1) *Pre-transition:* This period starts from a turning point from strengthening to weakening of the MFC divergence and ends with the beginning of increasing (CWV). Such a change is mainly due to reduced moisture export out of its northern boundary. This reduction is presumably due to warming of surface temperatures within the southern Congo. This reduces

the large-scale temperature gradient between the southern Congo and the Sahel, weakening moisture export out of its northern boundary. Otherwise, most atmospheric conditions are representative of seasonal drying: P is still at its annual lowest point. ET declines likely due to decreasing surface solar radiation resulting from low insolation and increasing amounts of low clouds.

(2) *Early-Transition:* This period marks the transition from seasonal drying to seasonal moistening of the CWV and surface specific humidity. Low-tropospheric moisture transport from the Atlantic Ocean and northern Congo increase rapidly, leading to net MFC convergence at the end of this phase. Increasing insolation finally outpaces the increase of cloudiness and aerosols, leading to increase of surface solar radiation, photosynthesis, and ET at the end of this phase. Increasing CWV in the lower troposphere promotes more shallow convection, which, in turn, moistens the mid-troposphere.

(3) *Late-Transition:* ET becomes an equal source of moisture for rainfall, while increasing moisture transport from the Atlantic Ocean and decreases in the strength of the return branch of the Congo Basin Cell further increases MFC. CWV and CAPE increase while CIN decreases rapidly, creating favorable thermodynamic conditions for deep convection. The CAB further encourages mixing of this moist air with the relatively dry air from the sub-tropical southern hemispheric Africa, promoting atmospheric instability (not shown). The AEJ-S forms during this time, which enhances rising motion to the north of AEJ-S entrance and vertical wind shear between the lower and mid-troposphere. These conditions provide a dynamically conducive environment for deep convection over the southern Congo basin.

We show that increase of moisture transport prior to ET is central for the dry to rainy season transition. During the late transition, local ET increases due to increases in plant

photosynthesis, driven by increases in surface solar radiation. It is likely that a combination of local ET and plant transpired moisture advected from the humid, tropical rainforests in the northern Congo then takes over as the main moisture source by the late transition period. Additionally, we show that increases in local ET during the early transition are decoupled from P, soil moisture, and VPD, all factors linked to water availability/demand for/from vegetation. ET begins to increase despite low soil moisture and high VPD during the early transition period, indicating limited response to water stress. Our research thus highlights the importance of ET, both local and remote, in being a key link in the tight water-carbon-energy cycle coupling noted in the tropics (Gentine et al., 2019).

CHAPTER 6

On the Mechanisms Controlling the Transition Periods to the Rainy Seasons in the Equatorial Congo Basin

6.1 Introduction

The Congo Basin is a global water and carbon center hosting vast rainforest, rivers, and precipitation (Brummett et al., 2009, Alsdorf et al., 2016, Xu et al., 2021). However, due to a lack of in situ data and relatively small infrastructure for research (Alsdorf et al., 2016), its meteorology has been less studied compared to the rest of Africa (Washington et al., 2013). Most studies examining process controls on seasonal rainfall thus focus on the rainy seasons, but less investigation has examined the transition to the rainy season onsets (Nicholson 2022, Cook and Vizy 2022, Pokam Mba et al., 2022). To fully understand observed rainfall variability (Jiang et al., 2019, Zhou et al., 2014, Hua et al., 2016; 2018), within the equatorial region (defined as the area between $2°S$ and $2°N$), which experiences two rainy seasons in boreal spring and fall (Figure 6.1; Pokam Mba et al., 2022, Nicholson, 2022), necessitates a full understanding of the

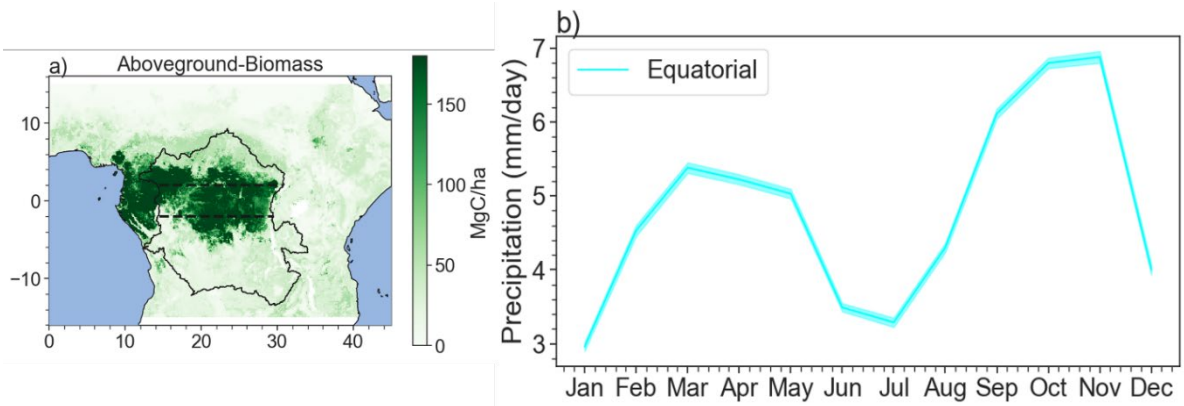

Figure 6.1: a) Above-ground biomass averaged between 2000-2019. Black outline denotes the Congo Basin watershed and the dashed lines at $2°S$ and $2°N$ represent the boundary of the equatorial region. b) Precipitation climatology for the equatorial region. Shades are the standard error of the mean over the grid cells within the boundary.

mechanisms controlling seasonal rainfall.

The equatorial Congo Basin is unique in that seasonal rainfall is not associated with strong surface moisture flux convergence (Nicholson, 2018, Yang et al., 2015). Instead, near surface divergence points towards mid-tropospheric moisture convergence being key for rainfall formation. Additionally, the large band of surface moisture convergence is located to the north of the areas of intense rainfall during its rainy seasons (Nicholson, 2018; 2022). Rainfall is rather controlled by complex interactions between atmospheric moisture sources, dynamics, and mesoscale convective systems (e.g., Pokam et al., 2012, Nicholson and Grist 2003, Jackson et al., 2009. Atmospheric moisture for rainfall mainly comes from evapotranspiration (ET) and the surrounding oceans. Their relative contribution to atmospheric moisture is still debated, but recent studies that consider ET, including from outside the basin, indicate that contributions of ET are greater than 50% (S. Worden et al., 2021, Sorí et al., 2022, van der ent et al., 2010). This moisture is transported into and out of the region and mixed within the different parts of the atmospheric via a series of dynamic systems: the Congo Basin Cell (Longandjo and Rouault 2020), the Congo Air Boundary (Howard and Washington, 2019), the African Easterly Jet North and South (AEJ-N, AEJ-S; Nicholson, 2022, Chen 2005, Kuete et al., 2020), a deep Walker-like circulation (Longandjo and Rouault 2020), and shallow meridional overturning cells (Longandjo and Rouault 2023). Additionally, topographic differences arising from the beginnings of the East African Rift help induce uplift and precipitation on the Congo Basin's eastern boundary (Nicholson, 2022).

However, moisture contributions and presence of these dynamical systems vary throughout the year, likely leading to differences in the mechanisms controlling the transitions to the spring and fall rainy seasons. The annual presence of the Congo Basin Cell is debated, with

Longandjo and Rouault (2020) arguing that the cell is present year-round, while Neupane (2016) and Cook and Vizy (2016) argue that it is present only in the second half of the year. The Congo Air Boundary is strongest August-October, while the frequency that it is identified goes to near zero between December and January (Howard and Washington 2019). The AEJ-N is present year-round but moves latitudinally such that it is centered near the equator during the spring rainy season but centered around $10°N$ during the fall rainy season (Kuete et al., 2020, Nicholson and Grist 2003). The AEJ-S only develops in the boreal fall in September (Kuete et al., 2020) and is therefore not as relevant for the transition to the equatorial spring rainy season. The roles of the heat lows additionally change between the two rainy seasons. During the fall rainy season, the southern African heat low is centered over the plateau region as the Angola heat low, but prior to the spring rainy season, the heat low migrates to become the Kalahari heat low (Howard and Washington 2018, Attwood et al., 2024) and a thermal low develops in the Angola region (Howard and Washington, 2019). Meanwhile, the West African heat low is centered around the Sahelian region during the spring rainy season (around $10° - 15°$). During the fall rainy season, it transitions from the Sahara region back towards the Sahel and Central Africa (Lavaysse et al., 2009). The different position of the heat lows can affect meridional moisture flow in and out of the basin. The mechanisms controlling the transition periods to the rainy seasons likely reflect the seasonal presence or movement of these key features.

6.2 Data

We use satellite and reanalysis estimates in our study. We resample all data to 5-day pentads, except for the Tropospheric Emission Spectrometer (TES) data due to relatively limited data points.

Satellite Data: We use the following satellite data products in our study:

-We use Tropical Rainfall Measuring Mission (TRMM) 3B43 monthly gridded P and 3B42 daily gridded P data at $0.25° \times 0.25°$ resolution between 2000-2019 that are generated using a combination of microwave and radar sensors calibrated with gauge data from the Global Precipitation Climatology Center (GPCC) (Huffman et al., 2007).

-We use the following Atmospheric Infrared Sounder (AIRS) L3 V7 daily Standard Physical Retrieval, $1° \times 1°$ gridded ascending TqJoint (as suggested by Wright et al., 2017) products between 2003-2018: total water vapor, atmospheric-layer mass mixing ratio, surface mass mixing ratio, and atmospheric-layer temperature(Aumann et al., 2019, Pagano et al., 2003, Irion et al., 2018, DeSouza-Machado et al., 2018). All atmospheric-layer products utilize the H2OPressureLev or H2OPressureLay 12 standard pressure levels.

-We use the Clouds and the Earth's Radiant Energy System (CERES) Syn1deg Ed 4.1 $1° \times 1°$ gridded daily cloud top temperature (CTT), cloud top height (CTH), and cloud area fraction (total, high, mid-high, mid-low, and low). This product incorporates derived fluxes from geostationary satellites (GEOs) to constrain global energy budget data computed by using the Fu-Liou radiative transfer model based on observed cloud and aerosol distributions. (Doelling, et al., 2013, Doelling et al., 2016, Su, et al., 2005, Rutan et al., 2015, Wright et al., 2017). Typical deep convective clouds in the Congo Basin are higher than 12 km (e.g., Hosking et al., 2010, Sohn et al., 2015, Chakraborty et al., 2020) with CTTs less than $-40° C$ (Hart et al., 2019). However, the observations of cloud top height (CTH), and CTT at each grid cell are inclusive of clear sky conditions, different cloud types, and on time scales greater than that of individual deep convection events. Therefore, while CTH and CTT are useful metrics to indicate deep convection during individual events, we use this data only to show change of deep convection qualitatively.

-We use the Global Land Evaporation Amsterdam Model (GLEAM) v3.7b $0.25 \times 0.25°$ daily land ET product between 2000-2019. ET products are estimated using the Priestly Taylor model (Martens et al., 2017).

- Annual, $0.1 \times 0.1°$ aboveground biomass between 2000-2019 is estimated by Xu et al. (2021) using a combination of lidar, global modeling, and satellite data. The following steps were taken to produce these estimates: 1) Ground inventory plots (>100,000 in number) are integrated with airborne and satellite data, with models used to relate lidar-derived metrics and radar backscatter to above-ground biomass (AGB) estimates from ground plots; 2) Spatially aggregated samples of woody vegetation AGB mean and variance at 10-km spatial resolution are developed using satellite and airborne lidar as training data; and 3) AGB is estimated by using the training data in spatial-temporal machine learning models. The satellite data used in the process come from the Ice, Cloud, and land Elevation Satellite (ICESAT), the Shuttle Radar Topography Missions (SRTM), the Advanced Land Observing Satellite (ALOS), Landsat, the Moderate Resolution Imaging Spectroradiometer (MODIS), and QuikSCAT (QSCAT). More details on this product can be found in Xu et al. (2021).

-We use the version 6 (v006_Litev01.00) daily Level 2 free-tropospheric deuterium (HDO) and H_2O measurements from the NASA Aura TES satellite instrument. The following quality flags were used when retrieving the data from the TES satellite: "Species Retrieval Quality = 1," "Degrees of Freedom for Signal >1," and "Average Cloud Optical Depth <0.4" in order to ensure good quality data as suggested by Worden et al. (2012). The accuracy of these data is ~6 per mil with a precision of 20 per mil (Worden et al., (2012) for the vertical range used in this analysis (~900-420 hPa, or about 1-6 km above sea level). We use data between 2005-2011 when the quality of estimates is suitable for our analysis (Worden et al., 2021). We use daily HDO and

H_2O measurements in this analysis instead of pentad measurements as the number of observations is limited compared to the other products.

Reanalysis Estimates: We use the fifth-generation of the European Centre for Medium-Range Weather Forecasts (ECMWF) ERA5 daily gridded $0.25° \times 0.25°$ resolution atmospheric reanalysis product between 2000-2018: zonal and meridional (u and v) winds, vertically integrated moisture flux convergence, vertical velocity, divergence, temperature, vertically integrated zonal and meridional moisture flux, and specific humidity. The reanalysis combines observations with model forecasts to estimate dynamic and thermodynamic atmospheric quantities (Hersbach et al., 2020).

6.3 Methods

6.3.1 Calculating the Onsets and Ends of the Rainy Seasons

We calculate the rainy season onsets and ends (RSOs, RSEs) in the equatorial hemispheric Congo Basin similar to that in Chakraborty et al. (2021) and Li and Fu (2004). This definition is designed to capture persistent high rainfall during the rainy season and persistent low rainfall in the dry season using the annual mean rainfall as the threshold. We first calculate the climatological pentad (5 day)-mean rainfall for each year over our domain. To calculate the rainy season onsets and ends, we did the following.

- For the spring rainy season onset: We find the first pentad of each year that meets the following criterion: four out of the previous six pentads are less than the climatological annual mean, and four out of the following seven pentads are more than the climatological annual mean.
- For the spring rainy season end: We find the first pentad of each year that meets the following criterion: four out of the previous six pentads are more than the climatological

annual mean, and four out of the following seven pentads are less than the climatological annual mean.

- For the fall rainy season onset: We find the first pentad of each year that meets the following criterion: six out of the previous eight pentads are less than the climatological annual mean, and six out of the following eight pentads are more than the climatological annual mean.
- For the fall rainy season end: We find the first pentad of each year that meets the following criterion: six out of the previous eight pentads are more than the climatological annual mean, and six out of the following eight pentads are less than the climatological annual mean.

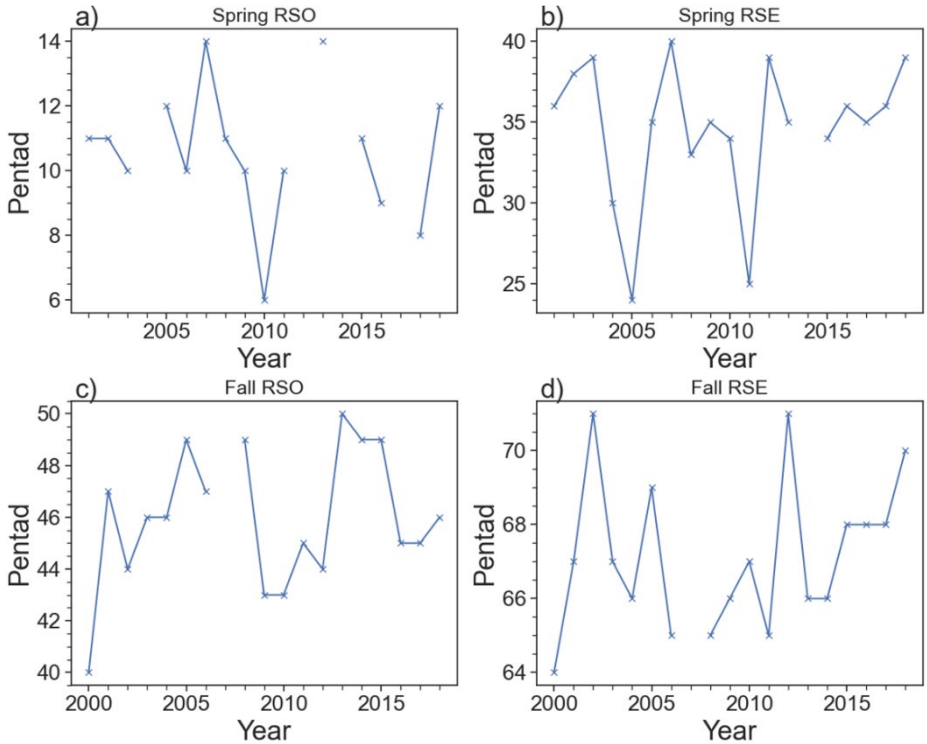

Figure 6.2: Pentad starts of the RSOs and RSEs for the equatorial Congo: a) Spring RSOs; b) Spring RSEs; c) Fall RSOs; d) Fall RSEs

We note that this criterion differs between the spring and fall rainy seasons because the spring rainy season is weaker than that of the fall (Fig 6.1). Therefore, a weaker threshold was needed to best capture the starts of persistently high and low rainfall.

Figure 6.2 shows the RSOs and RSEs for the spring and fall rainy seasons between the years 2000-2020 based on the TRMM pentad data. We excluded the year 2000 when calculating the spring RSO because we needed to consider the ends of the prior years. Similarly, we excluded the year 2020 when calculating the fall RSE because we needed to consider the start of the next years. We additionally excluded any years during which a RSO or RSE was unable to be identified, or if the length of a rainy season was less than 5 pentads. The spring RSO ranges from the 6th to 14th pentad (with Days 1-5 defined as Pentad "0"), corresponding to early-February to mid-March. On average, the spring RSO occurs on February 25. The spring RSE ranges from the 24-40th pentads, corresponding to early-May to late-July. On average, the spring RSE occurs on July 19. The fall RSO ranges from the 40th-50th pentads, corresponding to mid-July to early-September. On average, the fall RSO occurs on August 19. The fall RSE ranges from the 64th - 71st pentads, corresponding to mid-November to late-December. On average, the fall RSE occurs on December 2nd. We evaluated for overlap between the fall RSO and the spring RSE, as well as the spring RSO and the fall RSE and found none. To determine the number of pentads prior to each rainy season onset, we found the average difference between the fall (spring) RSO and spring (fall) RSE. This corresponded to 21 pentads for the difference between the spring RSO and fall RSE and 19 pentads for the difference between the fall RSO and spring RSE. Therefore, we took the average of the 21 pentads leading up to the spring RSO for each year, and the average of the 19 pentads leading up to the fall RSO for each year to examine the climatological seasonal evolutions. We define different phases of this transition based on the changes of the key

processes that drive the dry to rainy season transition as in Li and Fu (2004) and Wright et al. (2017).

6.3.2 Thermodynamic and Dynamic Equations

We calculate saturated equivalent potential temperature θ_{e_s} by assuming $r = r_s$, the saturated mixing ratio. We calculate r_s by the following:

We calculate e_s as in Bolton (1980):

$$e_s = 6.112exp\left(\frac{17.67T}{T+243.5}\right) \qquad \text{Eq 6.1}$$

Where T is the temperature in $°C$. We calculate saturated vapor pressure by replacing the mixing ratio with the saturated mixing ratio, which is calculated by:

$$r_s = \frac{\varepsilon e_s}{p-e_s} \qquad \text{Eq 6.2}$$

Where $\epsilon = 0.622$ is ratio of molar masses of vapor and dry air, and e_s is the saturation vapor pressure, calculated as in Bolton (1980):

$$e_s(T) = 6.112\exp\left(\frac{17.67T}{T+243.5}\right) \qquad \text{Eq 6.3}$$

We calculate θ_{e_s} using the following equation from Bolton (1980):

$$\theta_{e_s} = T_k\left(\frac{1000}{p}\right)^{0.2854\left(1-0.28\times10^{-3}*r_s\right)} \times exp\left[\left(\frac{3.376}{T_L} - 0.00254\right) \times r(1 + 0.81 \times 10^{-3}r_s)\right]$$

Eq 6.4

Where T_k is the absolute temperature (K), p is pressure (hPa), r is the mixing ratio (g/kg), T_L is the absolute temperature at the lifting condensation level (K) calculated by the following:

$$T_L = \frac{2840}{3.5lnT_k - lne - 4.805} + 55 \qquad \text{Eq 6.5}$$

Where $e = \frac{p*r}{622+r}$ is the water vapor pressure. We use the AIRS mass mixing ratio, temperature, and pressure in these calculations.

We additionally calculate diabatic heating as in Pokam et al. (2014):

$$Q_1 = C_p \frac{T}{\theta}\left(\frac{\partial\theta}{\partial t} + \boldsymbol{v} * \nabla\theta + \omega\,\frac{\partial\theta}{\partial p}\right) \qquad \text{Eq 6.6}$$

Where $\theta = T\left(\frac{p_0}{p}\right)^{\frac{R_d}{c_p}}$; ω is the vertical velocity (Pa/s), C_p is the specific heat at conastant pressure of dry air, and v are the horizontal winds (m/s), and θ and T are in units K.

We also calculate the difference in moist static energy between 925 and 700 hPa, a metric for conditional instability as discussed in Yang et al. (2015), where MSE is represented by:

$$MSE = c_p T + Lq + gz. \qquad \text{Eq. 6.7}$$

Where L is the latent heat of evaporation and g is gravity. Finally, we examine changes in moisture in the equatorial Congo with the following:

We examine vertically integrated moisture flux transport (MF), or the vertical integral of q, specific humidity times **V=(u,v),** the zonal or meridional winds integrated from the surface to the top of the atmosphere. We examine the net zonal MF (integral of q*u) across the western and eastern boundaries, and the net meridional MF (integral of q*v) across the northern and southern boundaries. For simplicity, we approximate the boundaries of the southern Congo Basin to straight lines. The northern boundary is across $2°N$ and between $14 - 30°E$. The southern boundary is across $2°S$ and between $14 - 30°E$. The western boundary is across $14°\ E$ and between $2°S - 2°N$. The eastern boundary is across $30°\ E$ and between $2°S - 2°N$. To compare to MFC, we compare the difference across the western/eastern boundaries and the northern/southern boundaries. However, the distance between the zonal boundaries is about four

times larger than the distance between the meridional boundaries. Therefore, we divide the zonal difference by four to best compare to MFC.

We additionally calculate the moisture convergence term ($-q \times \nabla . V$) and moisture transport vectors (qV) averaged between different pressure levels to represent the lower and mid atmospheric moisture transport. We examine the moisture convergence and moisture transport vectors at each pressure level prior to both the spring and fall to determine which pressure levels to average over (not shown).

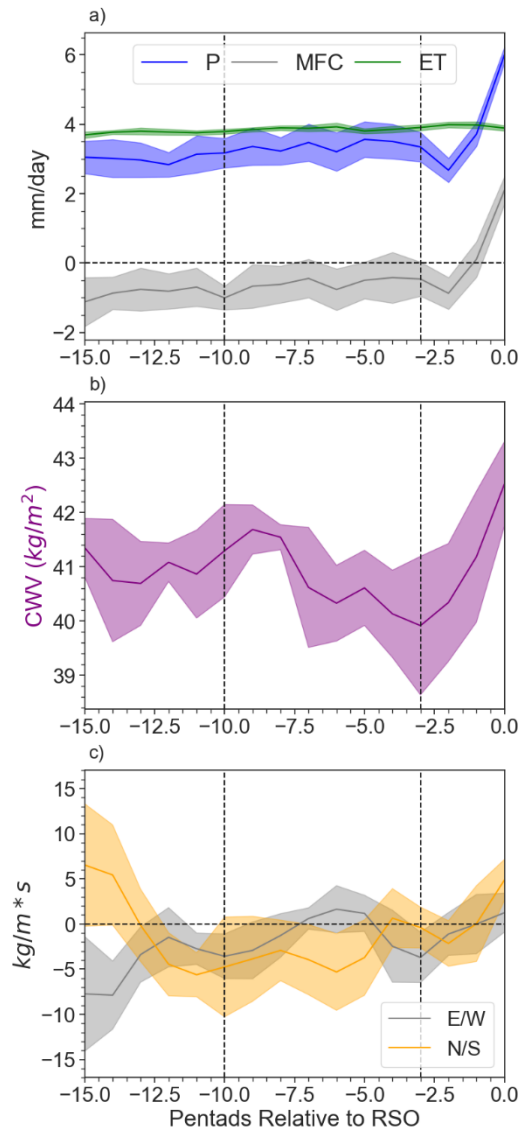

Figure 6.3: For the transition to the spring RSO: a) Precipitation (P), vertically integrated moisture flux convergence (MFC), and evapotranspiration (ET); b) surface specific humidity and column water vapor (CWV); c) Net MF across the zonal and meridional boundaries (Methods). Positive means convergence, negative means divergence. All are relative to the RSO (denoted as ‘’0 in the graph). Time series are smoothed using a Savitsky-Golay filter. Shades represents the standard error of the mean of the different years.

6.4 Results

In the following sections, we identify key changes in the atmospheric dynamic and thermodynamic conditions, as well as key energy and water fluxes, in the context of the evolution of the transition periods for spring and fall. We discuss the mechanisms controlling the spring rainy season transition period first, and then the fall rainy season transition period second.

6.4.1 Early Transition Period, Spring

The first part of the spring transition period, the early-transition period, starts with a turning point in vertically integrated moisture flux convergence (MFC; negative represents divergence; Fig 6.3a) 10 pentads before the start of the spring RSO. The turning point in MFC from most divergent to heading towards convergence means that the atmospheric circulation is changing to induce wetting conditions over the equatorial Congo Basin. To examine where this atmospheric circulation is changing, we evaluate net zonal and meridional vertically integrated moisture flux transport (MF; Fig. 6.3c). Here, positive values indicate net MF into the basin, and negative values indicate net MF out of the basin across the boundaries described in section 6.3.2. The change in MFC towards convergence is initiated by a decrease in the net amount of zonal MF leaving the basin (Figure 6.3 c). This is due to increases in low-level moisture transport averaged between 925-875 hPa from the Atlantic Ocean as well as decreases in mid-level moisture transport averaged between 850-600 hPa out of the basin back to the Atlantic Ocean (Fig 6.4 a,b, d, e, Appendix C.1 a,b). Increases in low-level moisture transport into the equatorial region are due to increases in the strength of the low-level westerlies. These increase in strength over western equatorial Africa between $10° - 15° E$ due to increases in near surface diabatic heating in the northern Congo and Sahel, likely due to radiative heating or latent heat release, between $2°N - 8°N$ (Fig 6.5), consistent with Pokam et al. (2014). We do not find that the zonal surface temperature gradient controls the strength of the low-level zonal winds (Appendix C.2), in contrast with Longandjo and Rouault (2020). Meanwhile decreases in mid-level zonal moisture transport are due to a decrease in the strength of the AEJ-N (Fig 6.6 f), which is located over the equator during the transition period. Therefore, changes in MFC initiate the transition period to the spring rainy season onset.

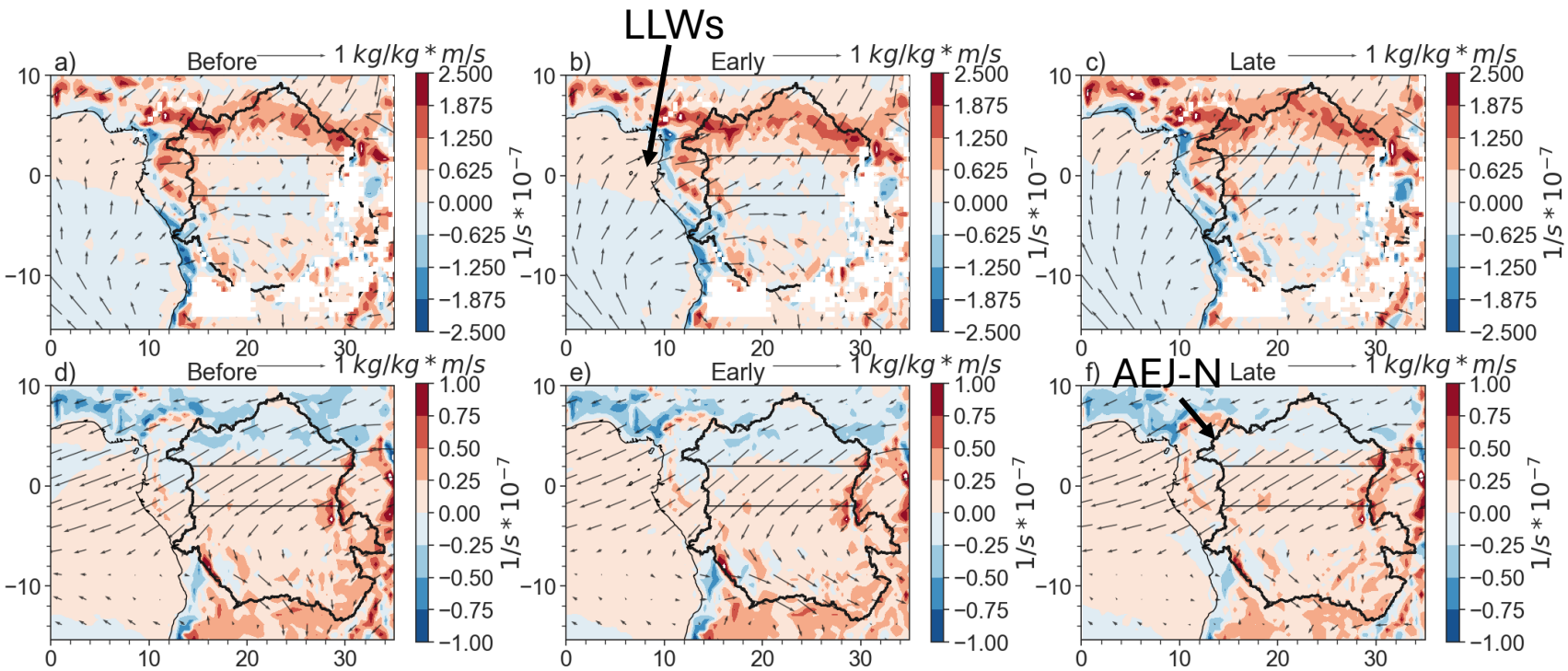

Figure 6.4: Moisture transport vectors (q*v) and moisture convergence (shades; positive means convergence) for a-c) average of 925-875 hPa for the "before," early, and late transition periods; d-f) average of 850-600 hPa for the "before," early, and late transition periods. Vectors are scaled up by 2 in order to better visualize the changes in magnitude and direction between periods. White shading in a-c represents areas where the topography is greater than 875 hPa. Moisture transport onto land between $8°S - 2°N$ from the Atlantic Ocean at low levels, a-c), represents the low-level winds (LLWs) described by Pokam et al. (2014). Mainly zonal moisture transport at mid levels between $4°S - 4°N$ represents the AEJ-N.

ET does not change but is the clear dominant contributor to moisture ($f_{mix} = 0.791 \pm 0.12$; Fig. 6.7b, consistent with S. Worden et al., 2021 for a similar domain), making it important as a source These changes in atmospheric moisture then change atmospheric conditional instability:

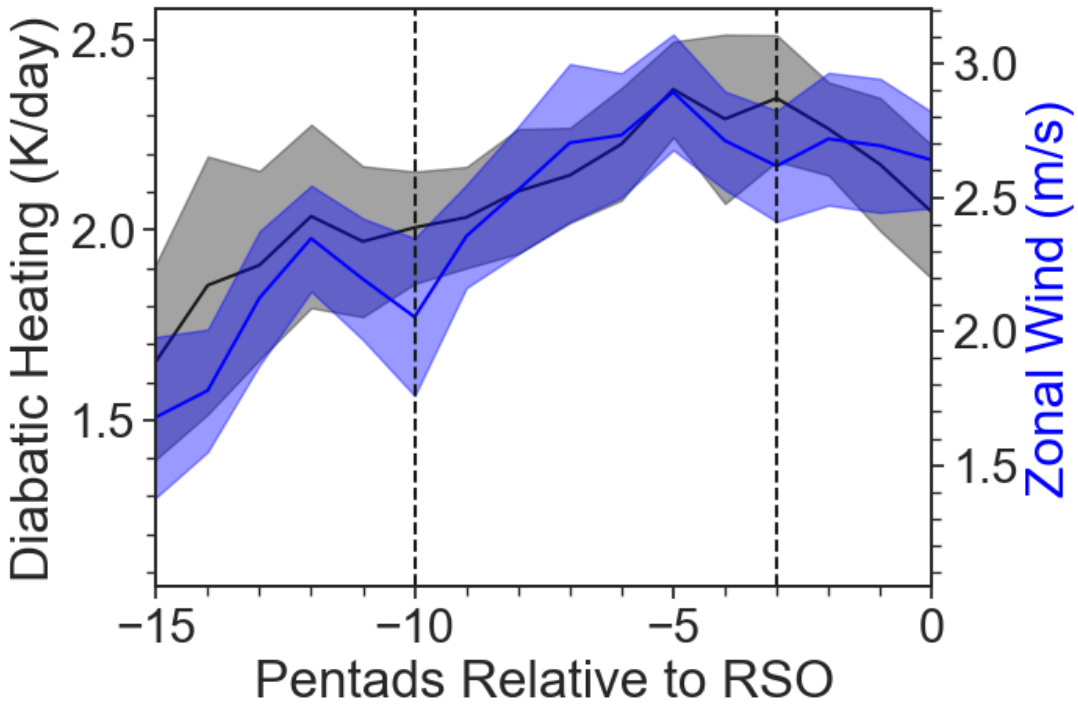

Figure 6.5: Near-surface (925 hPa) diabatic heating averaged between 15-30E and 2N-8N, and near-surface (925 hPa) zonal wind (u) averaged between 10-15E and 2S-2N. Shades represents the standard error of the mean of the different years.

Boundary layer atmospheric moisture begins to increase starting 9 pentads prior to the spring RSO, although it decreases again starting 5 pentads prior (Fig 6.8a). This is due to increases and subsequent decreases in low-level, zonally transported moisture across the western boundary of background moisture. (Appendix C.1a). Meanwhile, mid-level moisture transport initially decreases and then increases in magnitude across the western and eastern boundary, reflecting variability in the strength of the AEJ-N (Fig 6.6f). However, these changes act in opposing manners to cancel out net moisture changes in the mid-atmosphere, indicating that lower-boundary moisture is crucial for changing atmospheric conditional instability (Fig 6.6d).

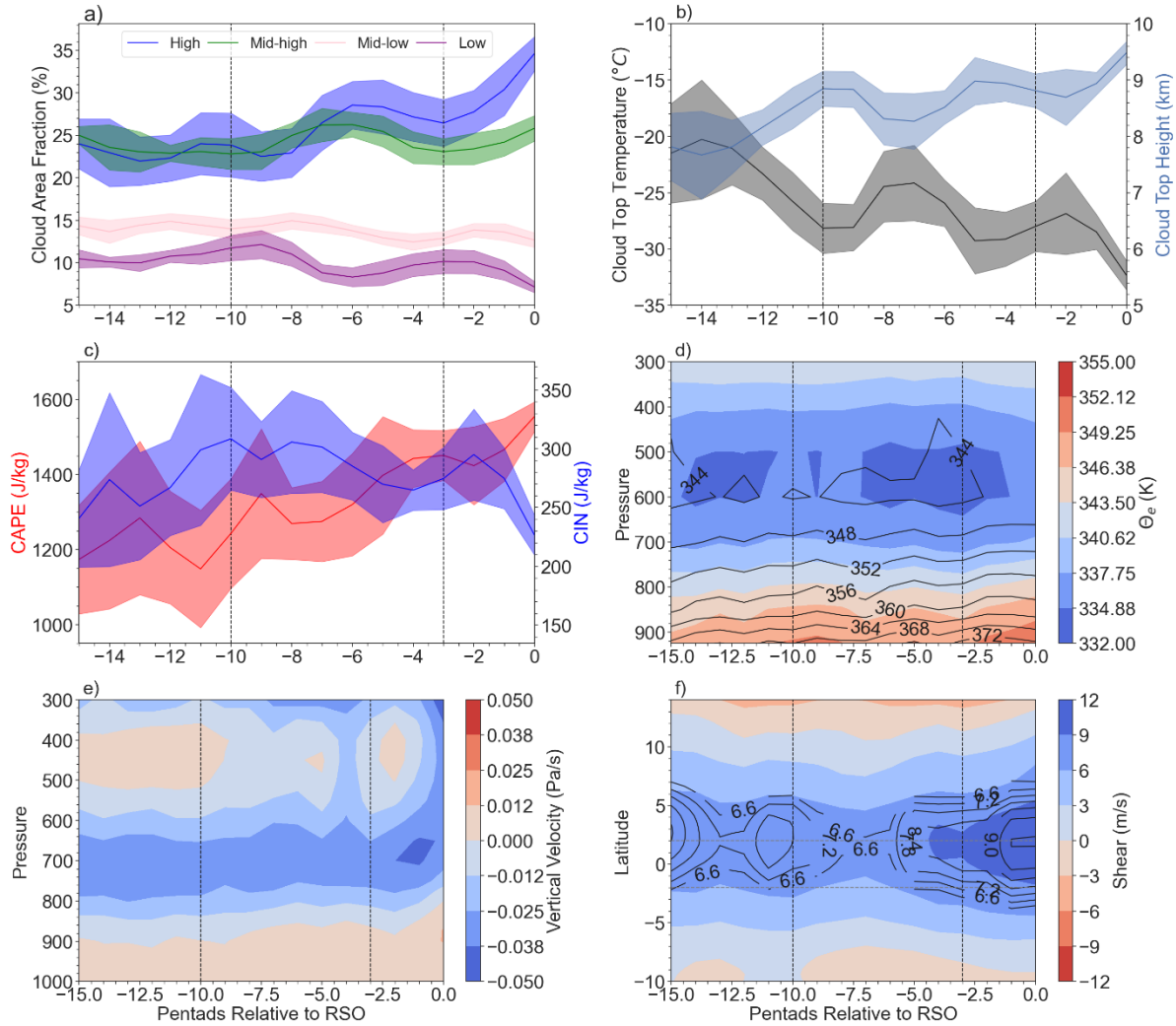

Figure 6.6: Prior to the spring RSO: a) cloud area fraction (CAF) for high, mid-high, mid-low, and low clouds; b) cloud top temperature (CTT) and cloud top height (CTH); c) convective available potential energy (CAPE); and convective inhibitive energy (CIN); d) equivalent potential temperature (θ_e; shades) and saturated equivalent potential temperature (black contours); e) vertical velocity; and f) black contours: 650 hPa zonal wind greater than 6 m/s, denoting the AEJ-N. Shaded contours represent the wind shear ($u_{650} - u_{925}$). Shades represents the standard error of the mean of the different years. All time series have been smoothed using a Savitsky-Golay filter.

The decreases in atmospheric conditional instability in the later part of the early transition indicate that the atmosphere is not yet ready to help initiate deep convection, which is reflected by subsequent increases in the LFC and CIN (Fig 6.6c, Fig 6.8b).

6.4.2 Late Transition Period, Spring

The late-transition period starts with a turning point in column water vapor (CWV), indicating that seasonal conditions have shifted to atmospheric moistening. This occurs 3 pentads before the start of the spring RSO, accompanied by increases in P (Fig. 6.3a). MFC becomes convergent by the end of the late transition period (Fig 6.3 a). At pentads -2-0, MFC and P suddenly increase sharply. We examine atmospheric moisture, atmospheric instability, and potential lift mechanisms to investigate whether they display corresponding changes that could initiate such rainfall increases.

Overall, increases in CWV helps support the increase in P, as ET does not change significantly ($f_{mix} = 0.788 \pm 0.152$, Fig 6.7c). Two pentads prior to the spring RSO, net zonal MF rapidly switches from divergence towards convergence, accompanied by increases in net meridional MF convergence (Fig 6.3c). The net zonal

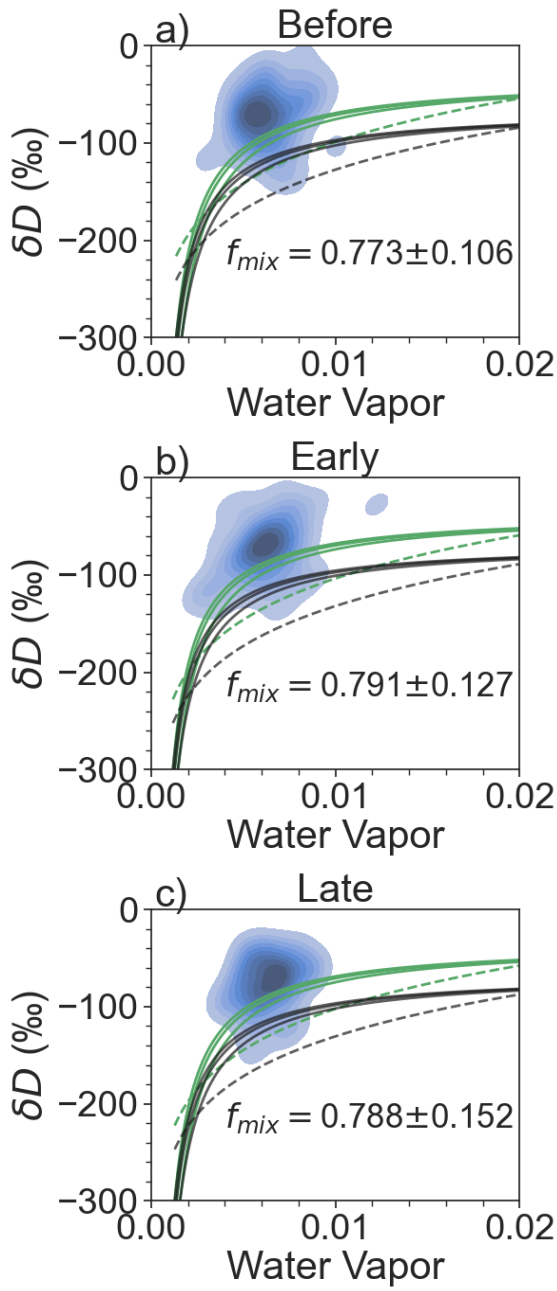

Figure 6.7: Fraction of observed δD above a series of mixing (solid) and Rayleigh (dashed) models. Green indicates land-based water vapor models, while black indicates ocean-based water vapor models. f_{mix} is the fraction of observed δDabove the uppermost, land-based mixing model. For a) the "before" period (15-11 pentads prior to the spring RSO); b) the early-transition; and c) the late-transition.

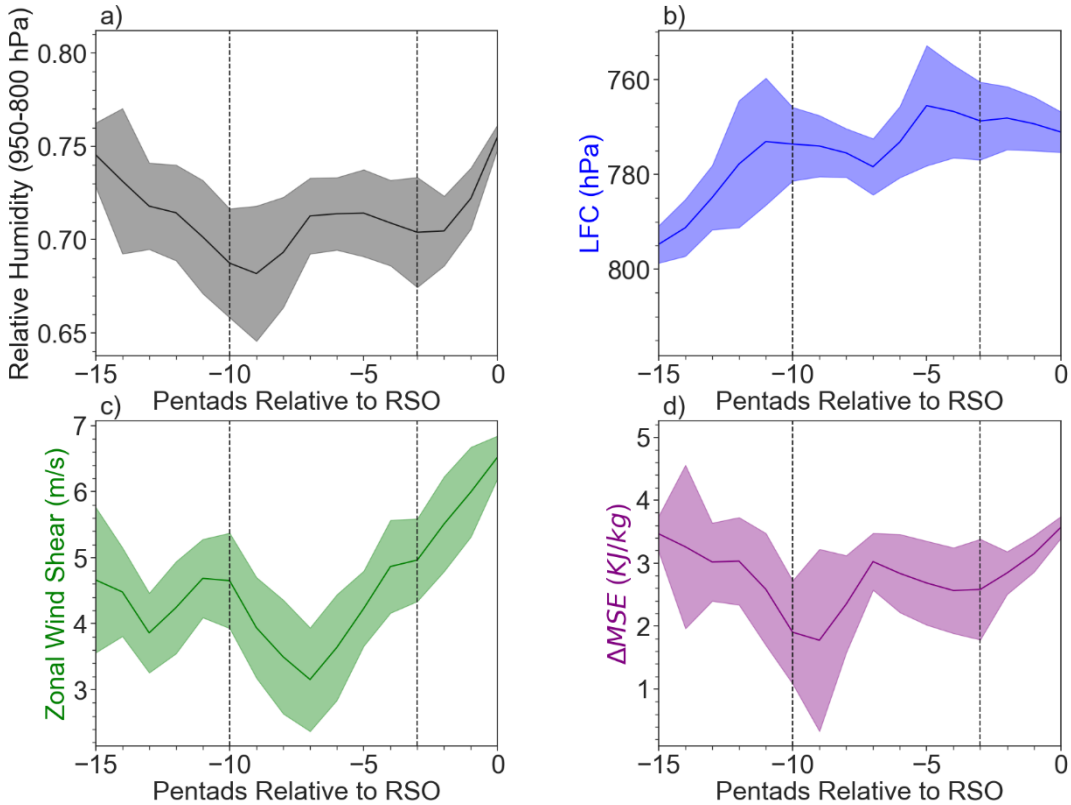

Figure 6.8: Evolution of a) relative humidity averaged between 950-800 hPa (RH); b) the level of free convection (LFC); c) zonal wind shear between 650 and 925 hPa; and d) $\Delta MSE = MSE_{925\,hPa} - MSE_{Sat,750\,hPa}$. All are relative to the spring RSO, averaged between $14 - 26°E$ to avoid topography errors in the calculations, and smoothed using the Savitsky-Golay filter. Shades represents the standard error of the mean of the different years.

MF increase into convergence is due to increases in mid-level moisture transport across the eastern boundary (Fig 6.4 e,f). Meanwhile, increases in the net meridional MF convergence are due to (1) increases in low-level moisture transport across the southern boundary (Fig 6.4 b,c; Appendix C.3c) and (2) decreases in southward moisture transport at mid-levels towards convergence zones below $10S$ (Fig. 6.4 e,f; Appendix C.3 d), associated with the Angola-region tropical low (Howard et al., 2019, Cook and Vizy 2022). This then decreases the meridional

component of the mid-easterly jet across the southern boundary of the Congo Basin (Fig 6.4 b, c, e, f).

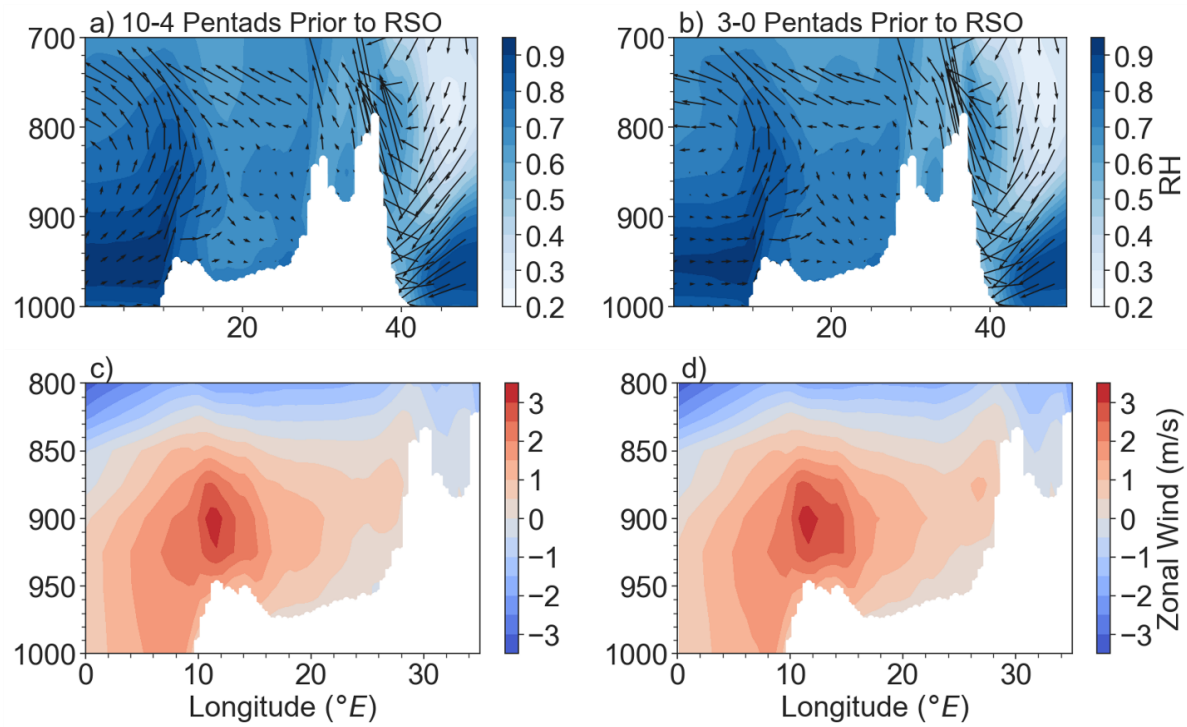

Figure 6.9: Relative humidity (shades) and vectors of u and $\omega * 10^2$ for a) 10-4 pentads prior to the spring RSO; b) 3-0 pentads prior to the spring RSO. Zonal wind (u) for c) 10-4 pentads prior to the spring RSO; d) 3-0 pentads prior to the spring RSO. White shading denotes the topography of the region.

However, subsidence prevents this increased boundary layer atmospheric moisture from being uplifted into the atmosphere between $15 - 26°E$, or within the region just west of and near the East African Rift (Fig 6.9). Instead, increases in zonal wind within the interior of the region, pushes this moisture towards the East African Rift (Fig 6.9), where orographic lifting forces this moist air into the free troposphere above 800 hPa. This acts to decrease the LFC and hence CIN (Fig 6.6c, Fig 6.8b). Meanwhile, shear increases with the increasing strength of the AEJ-N, thus creating conditions favorable for deep convection and the start of the spring rainy

season. This is indicated by increases in high clouds, increases in CTH, and decreases in CTT (Fig 6.6 a,b), as well as strengthening in uplift to the upper parts of the atmosphere (Fig 6.6 e).

6.4.3 Early Transition Period, Fall

The first part of the fall transition period, the early-transition period, similarly starts with a turning point in MFC from divergence towards convergence 14 pentads prior to the start of the fall RSO. This turning point means a reduction of moisture leaving the equatorial Congo Basin, mainly due to decreases in net zonal MF divergence (Fig 6.10c). We examine moisture transport and convergence at different pressure levels to investigate where in the atmosphere these changes happen.

During the "before" period, moisture transport between 925-875 hPa (Fig 6.11 a,b) from the Atlantic Ocean moves into the equatorial Congo before moving north towards the zonal convergence band above $10°N$, (Fig.

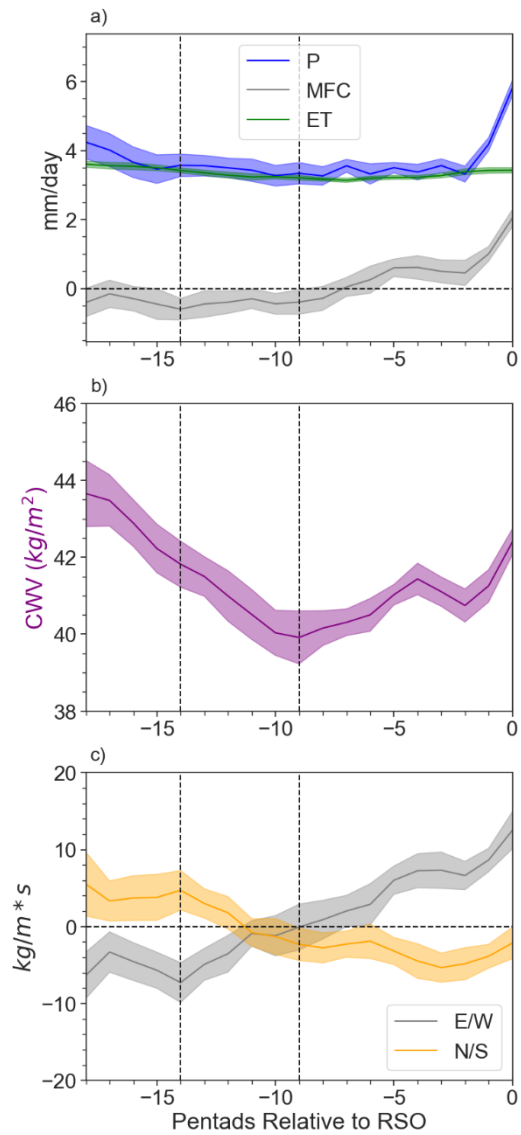

Figure 6.10: For the transition to the fall RSO: a) Precipitation (P), vertically integrated moisture flux convergence (MFC), and evapotranspiration (ET); b) surface specific humidity and column water vapor (CWV); c) Net MF across the zonal and meridional boundaries (Methods). Positive means convergence, negative means divergence. All are relative to the RSO (denoted as ''0 in the graph). All have been smoothed using a Savitsky-Golay filter. Shades represents the standard error of the mean of the different years.

6.11 a,b) associated with the Sahelian phase of the West African Monsoon (Thorncroft et al., 2011), as well as towards Sudan to feed its rainy season (Zhang et al., 2012). As the zonal land-ocean temperature gradient strengthens (Fig 6.12), the low-level winds into the equatorial basin across the western boundary increase in strength (now consistent with Longandjo and Rouault 2020) and begin to instead move south towards the newly formed Congo Air Boundary (Fig. 6.11 a,b; Appendix C.4; Howard and Washington 2019) in the southern Congo.

Between 850-800 hPa, north-easterly moisture transport goes from the southern part of the East African Rift, through the Congo Basin, and towards Sudan (Fig 6.11 d,e). The zonal component of this branch of low-level moisture transport across the western and eastern boundaries does not change significantly between the before and early transition periods (Appendix C.5b,e) and therefore is unlikely to cause changes to net zonal MF. Finally, at the mid-troposphere between 775-600 hPa, moisture transport is dominated by two flows (Fig 6.11g-i). One is the AEJ-N located to the north of the equatorial region (Fig. 6.13f). Meanwhile, a mid-level easterly jet exists over the equatorial region, which is return flow from the Congo Basin Cell (e.g., Longandjo and Rouault 2020, Neupane 2016). On average, this jet does not change significantly either between the "before" and early transition periods, although it does consistently decrease in strength during the early transition (Fig 6.11g,h; Appendix C.5 c,f). Meanwhile, ET does not change significantly: $f_{mix} = 0.564 \pm 0.077$ during the "before" period,19-15 pentads prior to the Fall RSO, while $f_{mix} = 0.681 \pm 0.17$ during the early transition (Fig 6.14 a,b). Therefore, it is changes in low-level moisture from the Atlantic Ocean that initiate the early transition period prior to the fall RSO. While changes in zonal MF indicate decreases in atmospheric moisture leaving the basin, other conditions indicate that this is not enough to initiate deep convection.

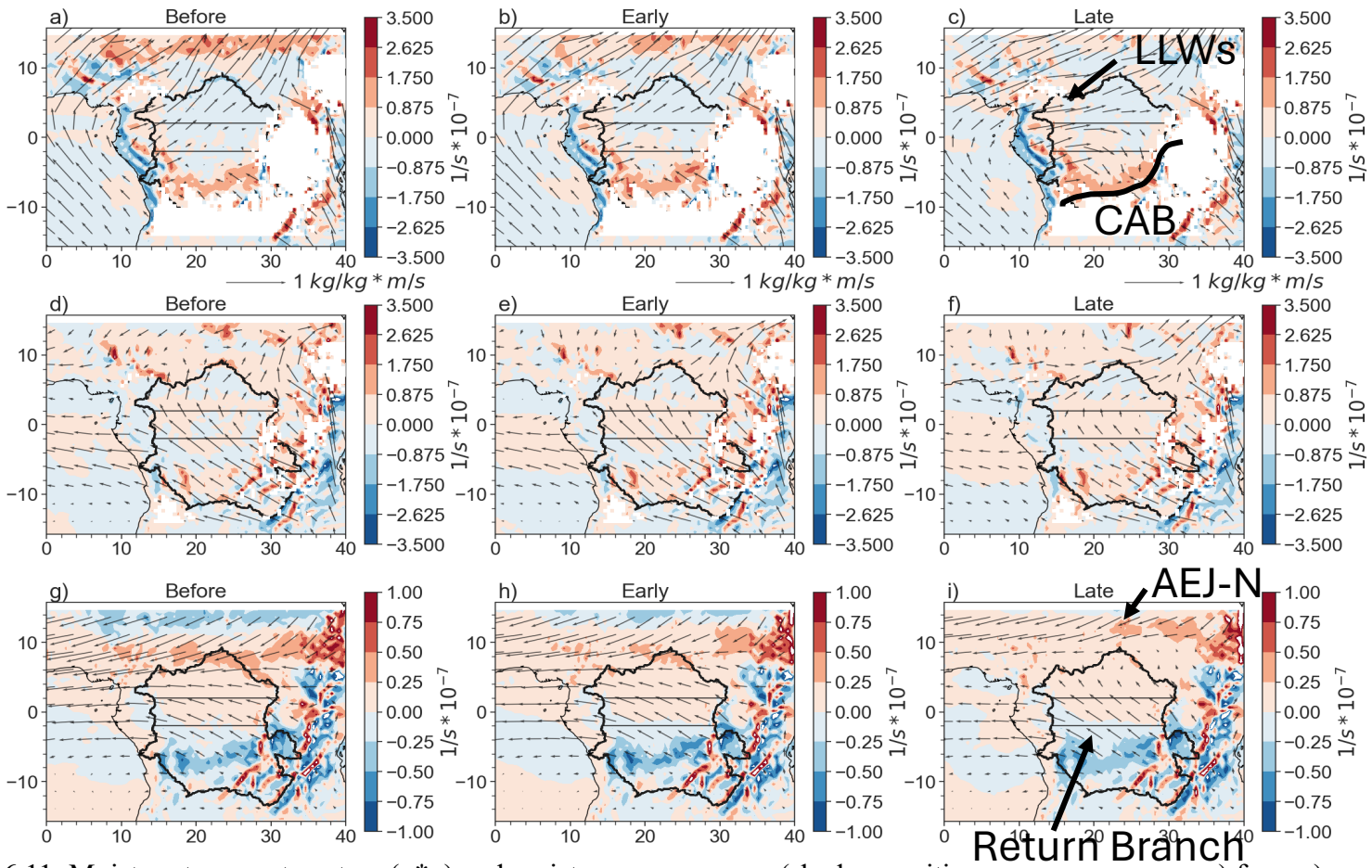

Figure 6.11: Moisture transport vectors (q*v) and moisture convergence (shades; positive means convergence) for a-c) average of 925-875 hPa for the "before" (19-15 pentads prior to the fall RSO), early, and late transition periods; d-f) average of 850-800 hPa for the "before," early, and late transition periods and g-i) averaged of 775-600 for the "before", early, and late transition periods. Winds have been multiplied by a scale factor of 2. White shades in a-c) mask topography greater than 900 hPa. White shades in d-f) mask topography greater than 850 hPa. Moisture transport between $5°S$ and $5°N$ into (out of) the basin represents the lower (return) branch of the Congo Basin Cell in a-c) (g-i). Area of convergence between $4°S$ and $8°S$ in a-c) represents the rough location of the Congo Air Boundary (CAB). Mainly-zonal moisture transport between $6°N - 15°N$ represents the AEJ-N.

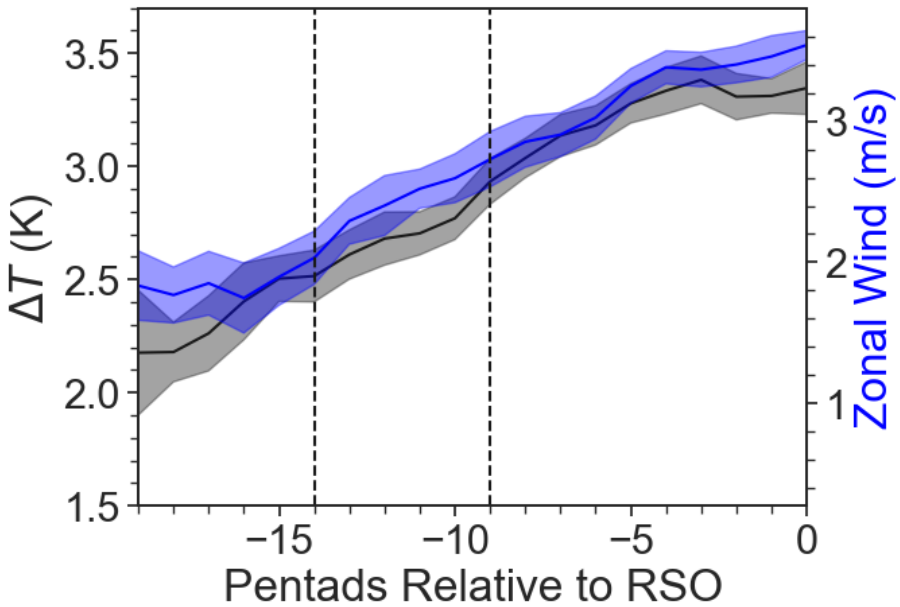

Figure 6.12: Near-surface (925 hPa) zonal temperature gradient: T_{land} is averaged between $10° - 15°E$ and $5°S - 5°N$ and T_{ocean} is averaged between $5°W - 5°E$ and $5°S - 5°N$. Blue line shows the near-surface (925 hPa) zonal wind (u) averaged between $10° - 15°E$ and $5°S - 5°N$. Shades represents the standard error of the mean of the different years.

Although $\frac{d\theta_e}{dp}$ is less than zero, its gradient weakens during this time (Fig 6.13d), consistent with a decrease in ΔMSE (Fig 6.15d). The increases of LFC and CIN and decrease of CAPE further confirm a stabilization of the atmospheric thermodynamic stratification (Fig 6.13c, 6.15b). This is reflected by increases in low clouds and decreases in high and mid-high clouds starting 13 pentads prior to the fall RSO, corresponding to increases in CCTs and decreases in CTHs (Fig 6.13 a,b).

6.4.4 Late Transition, Fall

The late transition period to the fall rainy season starts with a turning point in CWV, again indicating that seasonal conditions have shifted to atmospheric moistening. This occurs 9 pentads before the start of the fall RSO. During this period, P and ET remain mostly constant, while MFC increases and becomes convergent early on.

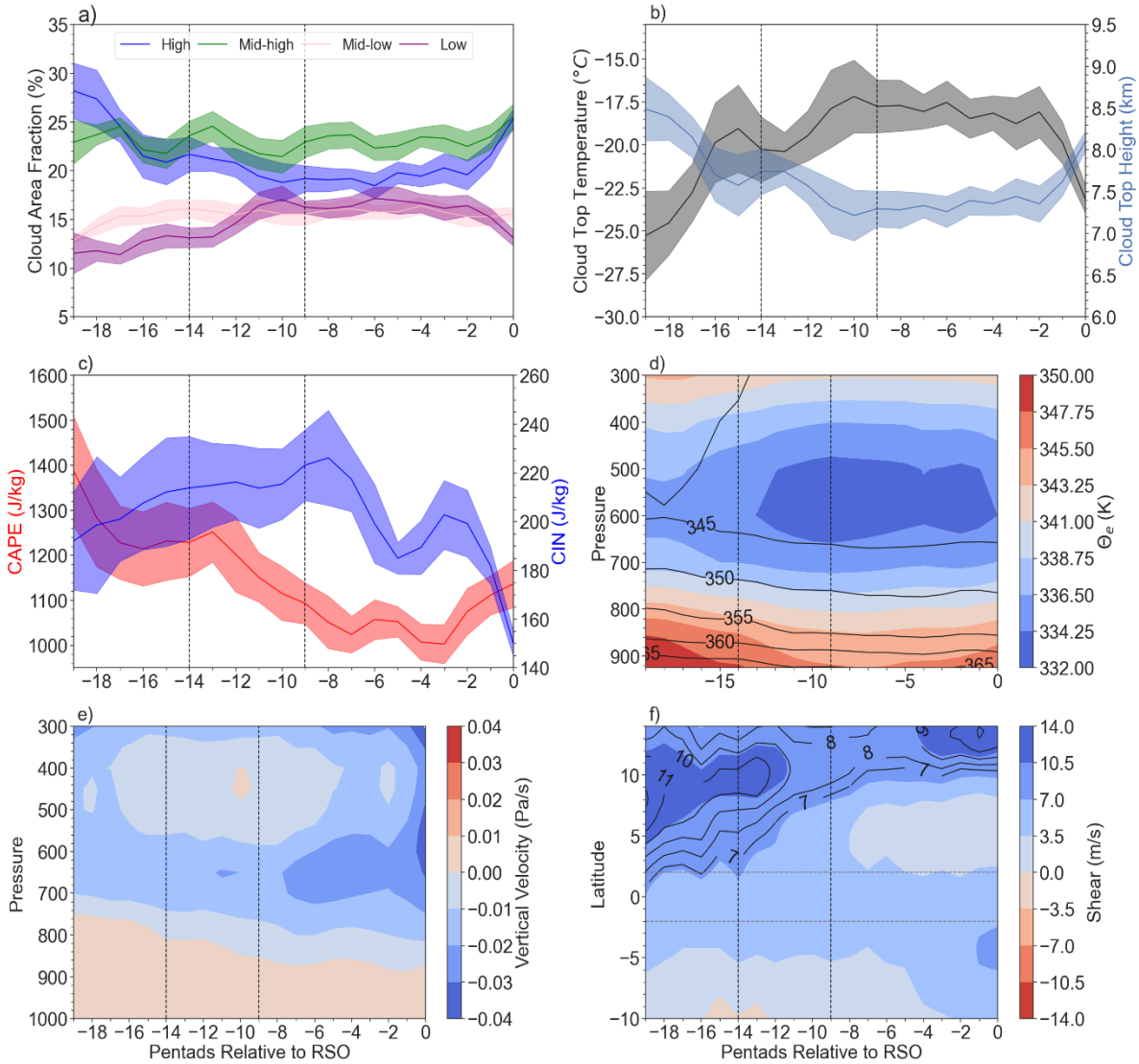

Figure 6.13: Prior to the fall RSO: a) cloud area fraction (CAF) for high, mid-high, mid-low, and low clouds; b) cloud top temperature (CTT) and cloud top height (CTH); c) convective available potential energy (CAPE); and convective inhibitive energy (CIN); d) equivalent potential temperature (θ_e; shades) and saturated equivalent potential temperature (θ_{e_s}); e) vertical velocity; and f) black contours: 650 hPa zonal wind greater than 6.5 m/s, denoting the AEJ-N. Shaded contours represent the wind shear ($u_{900} - u_{650}$). Shades represents the standard error of the mean of the different years. All time series have been smoothed using a Savitsky-Golay filter.

Increases in CWV are controlled by changes in net zonal MF, which increases in convergence during this period (Fig 6.10b,c). This is mainly due to an increase in the low-level winds coming from the Atlantic bringing more moisture into the equatorial region before moving down south towards the Congo Air Boundary (Fig 6.11c) as the zonal land-surface temperature

gradient increases (Fig 6.12). Meanwhile, ET still contributes the most to atmospheric moisture ($f_{mix} = 0.641 \pm 0.176$) but does not change significantly. Therefore, CWV increases (Fig 6.10b) are due to changes in oceanic moisture.

Both MFC and P increase sharply two pentads prior to the start of the fall rainy season, corresponding to sharp increases in boundary layer RH (Fig 6.15 a). This increase in atmospheric moisture destabilizes the lower atmosphere, as indicated by increases in the magnitude of $\frac{d\theta_e}{dp} < 0$. However, subsidence prevents moisture in the boundary layer from being uplifted into the troposphere between $15 - 26°E$ (Fig 6.13e). Instead, increases in zonal wind across the western boundary and into the interior of the region (Fig 6.16) 2-0 pentads prior to the fall RSO push this atmospheric moisture up along the slope of the East African Rift via orographic lifting, allowing it to reach >800 hPa. This decreases the LFC and hence CIN (Fig 6.13c, 6.25b), while

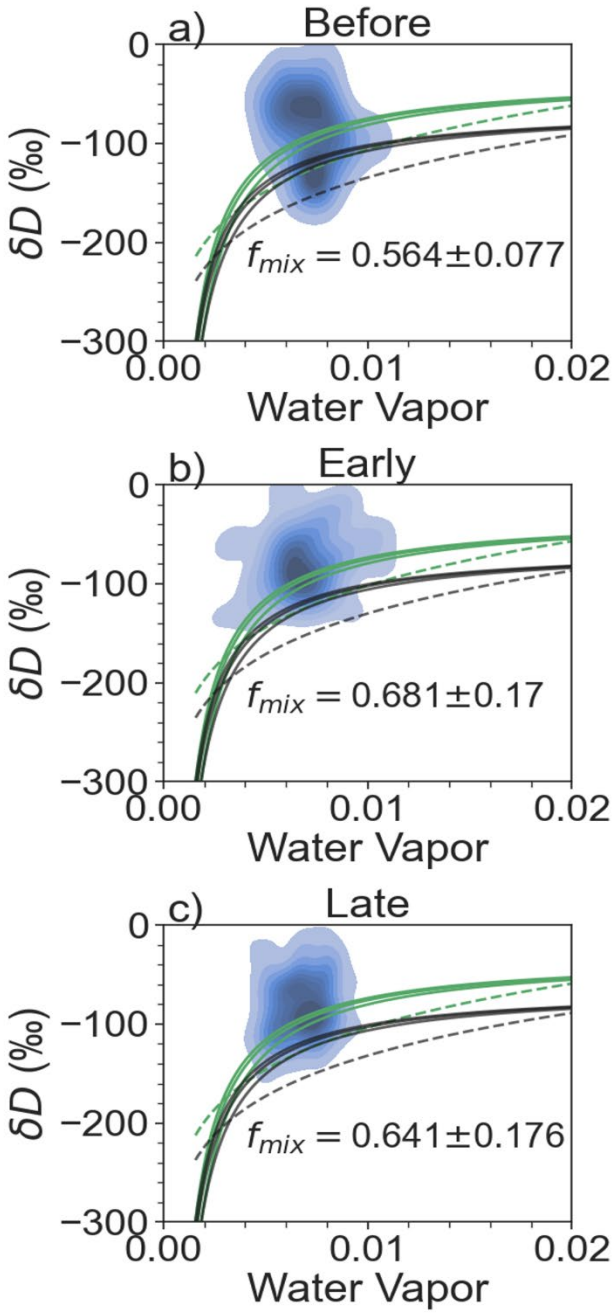

Figure 6.14: Fraction of observed δD above a series of mixing (solid) and Rayleigh (dashed) models. Green indicates land-based water vapor models, while black indicates ocean-based water vapor models. f_{mix} is the fraction of observed δDabove the uppermost, land-based mixing model. For a) the pre-transition; b) the early-transition; and c) the late-transition.

the vertical wind shear increases (Fig 6.15 c). Therefore, the atmospheric conditions become favorable for the formation of MCSs and the fall rainy season starts, as indicated by increases in the strength of vertical velocity from the lower atmosphere to 300 hPa (Fig 6.13 e), sharp increases (decreases) in high/mid-high (low) clouds, and sharp increases (decreases) in CTH (CTT; Fig 6.13 a, b).

6.5 Discussion

6.5.1 Comparing the Transition to the Spring vs Fall Rainy Season

We compare the evolution of conditions to initiate the spring and fall rainy seasons to clarify the different processes and their interactions that lead to the onset of each. For example, the transition to the fall rainy season clearly features a zonal overturning circulation, the Congo

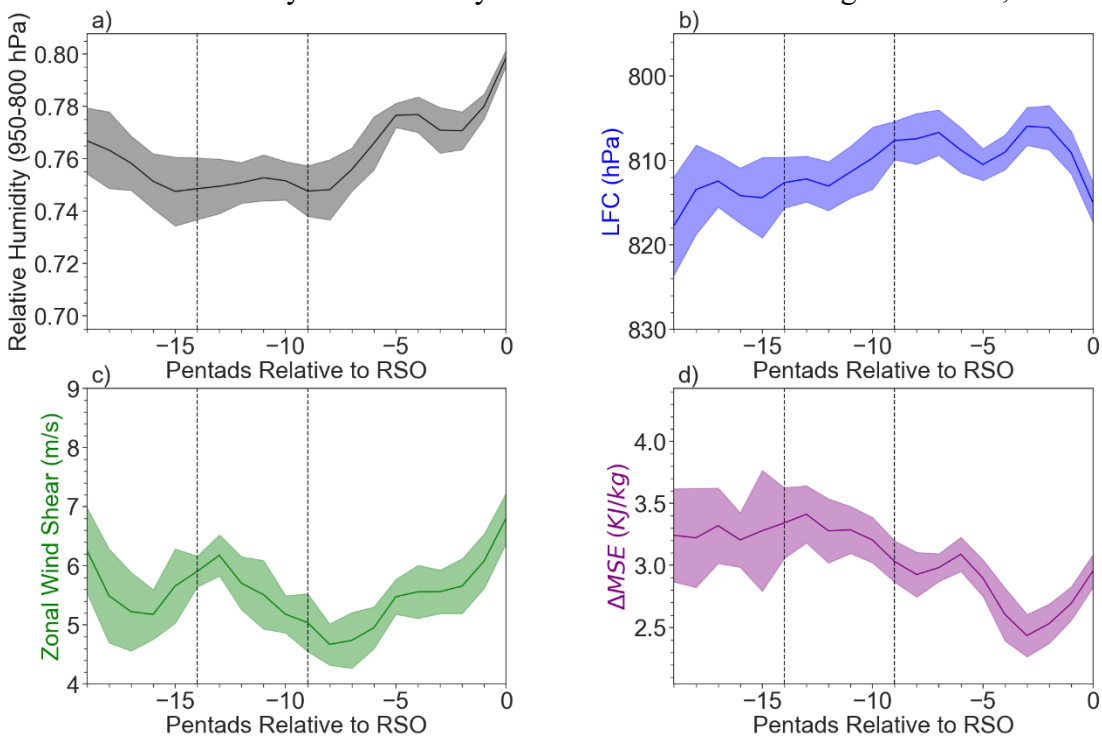

Figure 6.15: Evolution of a) relative humidity averaged between 950-800 hPa; (RH); b) level of free convection (LFC), c) zonal wind shear between 650 and 925 hPa; d) $\Delta MSE = MSE_{925\,hPa} - MSE_{Sat,750\,hPa}$. All are prior to the fall rainy season. All are averaged between 14-26E to account for effects of topography in the eastern part of the region. All have been smoothed using a Savitsky-Golay filter. Shades represents the standard error of the mean of the different years.

Basin Cell (Fig. 6.16 a,b) that moves moisture from the Atlantic ocean into the interior of the equatorial region. However, prior to the spring rainy season, while uplift still occurs (Fig. 6.9 a,b) around the highlands of Cameroon and Gabon (Nicholson, 2022), a complete overturning cell is not identified. Furthermore, the cause of the lower to middle tropospheric wind shear differs between the two rainy seasons. The zonal shear induced by the AEJ-N, present in the equatorial re gion prior to the spring rainy season but not the fall, increases prior to the start of the rainy season. While shear exists from the mid-level easterly jet at the same pressure levels, it is weaker prior to the fall rainy season.

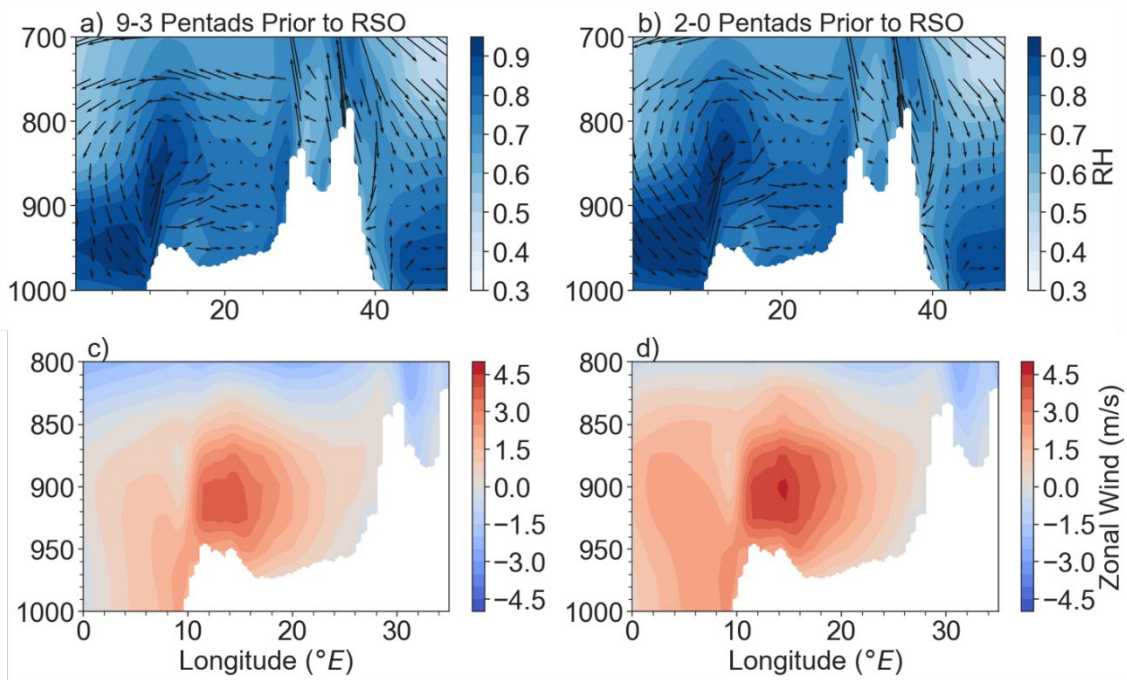

Figure 6.16: Relative humidity (shades) and vectors of u and $\omega * 10^2$ for a) 9-3 pentads prior to the fall RSO; b) 2-0 pentads prior to the fall RSO. Zonal wind (u) for c) 9-3 pentads prior to the fall RSO; d) 2-0 pentads prior to the fall RSO. White shading denotes the topography of the region.

Additionally, the thermodynamic conditions, especially at the near surface and in the lower troposphere, are more favorable for convection prior to the fall RSO than the spring RSO. In particular, CIN prior to the spring rainy season ranges from 242-325 J/Kg and is 236 J/kg 1 pentad prior to RSO, while CIN prior to the fall rainy season ranges from 149-235 J/kg and is at

149 J/kg 1 pentad prior to the RSO. The LFC is also lower prior to the fall rainy season than the spring rainy season. Thus, the cloud base is higher and convective air has to overcome stronger CIN prior to the spring rainy season compared to the fall rainy season.

6.5.2 Comparing the Transition to the Fall Rainy Season in the Equatorial vs Southern Congo

We next compare the transition period to the fall rainy season in the equatorial versus southern Congo. The equatorial fall rainy season happens earlier, on average August 19, compared to the southern Congo, beginning on average October 9 (Worden and Fu, 2024, in review). This difference in timing is likely due to the seasonal movement of the Congo Air Boundary (Longandjo and Rouault 2020), which is centered closer to the equator prior to the equatorial RSO and then moves south to be centered more within the southern Congo prior to the fall RSO (Appendix B.2, C.4). Furthermore, moisture contributions between the two regions differ greatly. ET is the dominant contributor to atmospheric moisture prior to the fall rainy season in the equator, however, it does not change significantly during the transition period. Meanwhile, for the southern region, ET contributes equally to atmospheric moisture by the late transition period, increasing significantly compared to the early transition period. Therefore, the equatorial region moisture changes are primarily controlled by advected oceanic moisture, while the southern Congo moisture changes are controlled by both ocean moisture and ET .

Furthermore, atmospheric instability differs strongly. In the equatorial region, CAPE is much higher than CIN for the entire transition period, helping initiate a large jump in P once CIN decreases as there is plenty of energy for deep convection. However, in the southern region, CAPE is much lower and CIN is higher than in the equatorial Congo, where above 700 hPa is dominated by adiabatic warming due to subsidence until the late transition period. Therefore, the equatorial region has larger potential for storms to occur than in the southern Congo basin.

Finally, the AEJs play different roles between the equatorial region and the southern Congo. In the equatorial region, both the AEJ-S and AEJ-N do not play a direct role in determining vertical wind shear in the fall RSO. In contrast, the AEJ-S directly contribute to the vertical wind shear prior to the RSO in the southern Congo. Therefore, it is important to consider the sub-basin scale variability in the evolution of atmospheric conditions prior to the transition to the rainy season onsets that will likely react differently to climate perturbations and hence the seasonal rainfall cycle.

6.6 Conclusion

Using a suite of satellite and reanalysis data, we examined the mechanisms controlling the transition periods to the spring and fall rainy season in the equatorial Congo. We summarize these mechanisms below.

Spring rainy season:

(1) *Early-transition:* This period starts from a turning point from strengthening to weakening of the MFC divergence. Such a change is mainly due to decreases in net zonal MF due to increases in low level winds from the Atlantic controlled by diabatic heating in western equatorial Africa. ET contributes the most to atmospheric moisture but does not change significantly. Meanwhile, CAPE is larger than CIN and $\frac{d\theta_e}{dp}$ is negative, indicating good potential for deep convection. However, deep convection does not trigger yet as CIN must still be overcome, atmospheric moisture must increase, and a lift mechanism needs to be more well developed.

(2) *Late-transition:* This period starts with increases in CWV, indicating increases in atmospheric moistening. 2 pentads prior to the RSO, MFC and P sharply increase. Increases in CWV are due to increases in net zonal and meridional MF. Meanwhile, the

contribution of ET to atmospheric moisture does not significantly change. CIN and LFC decrease sharply 2 pentads prior, while ΔMSE increases sharply, indicating increases in atmosphere instability. This is likely due to increases in lower atmospheric moisture that is zonally transported towards the East African Rift, where orographic lifting helps bring it into the free troposphere. Therefore, deep convection initiates and the spring rainy season begins.

The evolution of the fall rainy season transition period is similar to that of the spring rainy season, with some key differences. We show that shear is provided by the AEJ-N prior to the spring rainy season, but prior to the fall rainy season, it is provided by the return branch of the Congo Basin Cell. Furthermore, low-level moisture transport across the western boundary is stronger prior to the fall rainy season, explaining the relatively lower contribution of ET to atmospheric moisture for rainfall.

Overall, changes in advected oceanic moisture into the region from the Atlantic or leaving the region back to the Atlantic are responsible for initiating the transition periods and helping progress the atmosphere to be amenable to deep convection. ET contributes the most to atmospheric moisture for rainfall prior to both spring and fall rainy season and is therefore important mainly as a source of background humidity. It is also likely that moisture contributions from the Indian Ocean are important as a source of moisture entering the basin (e.g., Sorí et al., 2022); however, changes in moisture across the western boundary are key for transitioning the atmospheric conditions to deep convection.

The clarification of the atmospheric processes that drive the dry to rainy season transition provided by this study will lay the groundwork for understanding variability in the seasonal cycle of precipitation. This includes changes induced by ENSO, the Indian Ocean Dipole, and

Madden-Julian Oscillations (e.g., Kebacho and Sarfo 2023, Moihamette et al., 2022, Jury et al., 2009, Creese et al., 2019), variability induced by aerosols (Chakraborty et al., 2020), by the poleward movement of the northern and southern heat lows (Cook et al., 2020), and by the long-term AMJ drought (Jiang et al., 2019). Overall, the equatorial region seasonal rainfall is influenced by a combination of local and remote processes, thus increasing the ability of climate variability and change to alter its timing and intensity.

CHAPTER 7

Conclusions

In this chapter, I conclude by revisiting each science question presented in Chapter 1 and discussing the conclusions for each question based off the results presented in Chapter 3-7. I then provide a brief discussion of future directions based on the conclusions made in this work. Finally, I mention long-term goals inspired by this thesis work.

7.1 Summary

The overall goal of this dissertation is to better understand the Congo Basin water cycle to better inform climate models and understand the mechanisms controlling its observed variability. We have done this by answering the following scientific questions:

1. What is the relative contribution of evapotranspiration versus advected oceanic moisture to atmospheric moisture for rainfall over the Congo Basin?

In Chapter 3, we evaluated the relative contribution of evapotranspiration (ET) versus advected oceanic moisture to atmospheric moisture for rainfall in the equatorial region throughout the year using remotely-sensed water vapor isotopes. When comparing these observed isotopes to a mixing model showing the isotopic evolution of a land-based air parcel (i.e., from transpiration) when mixing with the surrounding air, we showed that ET contributes the most to atmospheric moisture for rainfall in this region throughout the year ($f_{mix} > 0.50$) except for during the rainy seasons. However, we note that the rainout effect, in which enriched (from land) water vapor preferentially condenses, could alter the isotopic signal enough during those months to indicate a lesser ET contribution. Therefore, it is still possible that ET contributes the most to atmospheric moisture during that time.

Additionally, in Chapters 5 and 6, we use the same method to evaluate the contribution of ET to atmospheric moisture prior to the starts of the rainy seasons in the southern and equatorial, and Congo. In Chapter 5, we show that in the southern Congo during the pre and early transition periods, advected oceanic moisture contributes most to atmospheric moisture for rainfall, but during the late-transition period, ET contributes the most to atmospheric moisture for rainfall. We hypothesize that this sudden jump in ET is due to a combination of increases in local ET as well as ET brought into the southern Congo from the equatorial region. However, in Chapter 6, we show that ET contributes the most to atmospheric moisture for rainfall (more so prior to the spring rainy season than the fall rainy season), during both the early and late transition periods. This is consistent with the results of S. Worden et al. (2021), as the domains heavily overlap with each other.

2. Has observed rainfall variability induced water deficits within the Congo Basin?

The Congo Basin has shown variability in its water cycle in the 21st century, such as decadal trends in precipitation, changes to the rainy season onset, ends, and lengths, and a long-term drought in April-June. We examined whether these changes were reflected in changes to its water balance, or evapotranspiration minus precipitation ($ET - P$; Chapter 4). Due to large uncertainties in ET and precipitation datasets, we estimated $ET - P$ using water vapor isotopes in conjunction with surface water balance measurements: gravity-based changes in terrestrial water storage and river discharge measurements from a river gauge station in Kinshasa-Brazzaville to estimate on $ET - P$. Typically $ET - P$ estimates are limited to a basin scale due to the river discharge measurements. We showed that the linear relationship that exists between normalized water vapor isotopes and the surface water balance can be used to calculate $ET - P$ on sub-basin scales. When examining $ET - P$ on both basin and sub-basin scales, we did not

find any significant trends. If water variability between 2003-2018 induced water deficits, defined here at $ET - P > 0$, we would have seen an increasing trend. Therefore, the Congo Basin water balance displays limited response to changes in precipitation, potentially indicating resiliency to these changes.

1 What are the mechanisms controlling the transition periods to the rainy seasons within the Congo Basin?

To answer this question, we split the Congo Basin into three parts, divided by the $2°S$ and $2°N$ latitudinal lines: the southern Congo, equatorial Congo, and northern Congo. This is done to capture (1) hemispheric differences in the seasonality; and (2) examine the biannual regime within the equatorial Congo Basin. Seasonal rainfall is controlled by the complex interactions between atmospheric moisture sources, dynamic systems, and mesoscale convective systems. We examine their evolution prior to the rainy season onsets (RSOs) for the southern and equatorial Congo.

For the southern Congo, we show that the transition from the dry to the rainy season over the is initiated by a decrease in northward moisture export, about three to four months before the rainy season onset (RSO), referred to as the pre-transition period. During this period, ET is low due to low surface solar radiation, resulting from low insolation, and high amounts of low-level clouds. In the early transition period, one to three months before the RSO, CWV and surface specific humidity increase due to increased oceanic moisture. Meanwhile, ET starts increasing for the first time due to increases in surface radiation and vegetation photosynthesis, despite a lack of soil moisture increases. Finally, in the late transition period about one month before the RSO, ET continues to increase, contributing equally to atmospheric moisture needed for deep convection as advected oceanic moisture. Additionally, the formation of the African Easterly-Jet South and the

southward movement of the Congo Air Boundary increase vertical wind shear and provide large-scale dynamic lifting of the warm and humid air from the Congo. The frequency of deep convection increases rapidly, leading to the start of the rainy season. Therefore, the RSO over southern-hemispheric Congo basin is a result of combined large-scale atmospheric circulation change and vegetation response to the seasonal change of insolation.

For the equatorial region, we show that changes in advected oceanic moisture across the western boundary from the Atlantic initiate the transition period to the rainy seasons in boreal spring and fall. While ET provides the most atmospheric moisture, it functions mainly as background moisture. Generally, thermodynamic conditions indicate an unstable atmosphere, but changes in the LFC and CIN must happen for deep convection to initiate. We additionally show that the East African Rift likely provides the lift mechanism needed to transport moisture upwards in the atmosphere, while the AEJ-N and return branch of the Congo Basin Cell provides shear for the spring and fall rainy seasons, respectively. Therefore, the RSOs over the equatorial region are a result of large-scale atmospheric circulation changes.

7.2 Future Directions

To my knowledge, the work presented in this dissertation provides the first systematical assessment of the atmospheric moisture sources, moisture fluxes, and the mechanisms controlling the transition periods to the rainy seasons. Therefore, we have increased fundamental understanding of the Congo Basin seasonal water cycle. Future research can then use this understanding to test how the rainy sesaon onsets and so the Congo Basin water cycle change under present and future variability, especially by evaluating the influences of external global climate change and internal land use on the key thermodynamic and dynamic processes that

control the rainy season onset. We discuss future directions based off the significant results of this dissertation below:

This dissertation explores the transition periods to the rainy seasons in the southern and equatorial Congo basin, but the northern Congo Basin transition period still much be investigated. This region, with an annual rainy season, likely receives moisture from the equatorial Congo Basin at the near surface (Ch 6). Furthermore, interactions with the ITCZ and the West African Monsoon (WAM) are likely important as it is hosts the zonal moisture convergence band (Nicholson, 2018) during some parts of the year and it is closest to the Gulf of Guinea/Sahelian area where the WAM seasonally travels. Changes in how atmospheric moisture is transported throughout the seasons will be crucial for understanding the transition period to its rainy season.

Additionally, this dissertation primarily uses ERA5 reanalysis to examine dynamics and thermodynamic conditions as observations are either unavailable or not well constrained due to interference with remote sensing such as clouds or rainfall (e.g., Chambers et al., 2007). We choose to use ERA5 reanalysis as this is frequently used in other studies of this region (e.g., Crowhurst et al., 2020, Cook and Vizy 2022, Alber et al., 2020). However, discrepancies do exist between the different reanalysis products (e.g., Longandjo and Rouault 2020, Kenfack et al., 2023, Hua et al., 2019). To gain more confidence in the atmospheric moisture, dynamic systems, and thermodynamic conditions that we discuss in this dissertation, the next steps are to examine whether they are reproduced in other reanalysis products, such as JRA-55, MERRA2, and NCEP-2 (Gelaro et al., 2017, Kanamitsu et al., 2002 for NCEP-2, Kobayashi et al., 2015).

This dissertation highlights the key role of ET, especially for the tropical rainforests around the equator, in regulating the Congo Basin water cycle. Therefore, alterations to ET, either induced by climate change or land cover and land use changes (LCLUC), could have significant

impacts on the region's water cycle locally as well as surrounding areas. Modeling studies focusing on the impacts on ET, and hence the Congo Basin water cycle, from climate change, LCLUC, or their combined effects would help us better understand the following question: Could enough vegetation stress and/or vegetation alteration lead to a rapid decline in ET, and with it, dramatic changes to the Congo Basin water cycle that induces a tipping point for its vegetation? For example, while the Congo Basin is historically less deforested compared to other tropical regions, due to comparatively small clearing mechanisms (Tyukavina et al., 2018), deforestation and degradation has rapidly increased since the start of the 21st century (Vancutsem et al., 2020). This has mainly happened on the outskirts of the equatorial humid intact forest regions, but increased demand for resources and rapidly increasing human expansion into the region (e.g., Vancutsem et al., 2020) could lead to larger-scale forest removal. Therefore, modeling studies that examine changes to ET and its water cycle based off spatially realistic simulations of future land cover and land use changes could identify if such tipping points exist.

In addition, ET from the tropical forests could provide moisture not just for the equatorial region, but also for the southern region. While water vapor tracer models have been used in the past to examine moisture contributions during the rainy seasons (e.g., Dyer et al., 2017), or throughout the year but on large spatial or monthly temporal scales (Sorí et al., 2017; 2022), no work has been done to explicitly examine moisture sources during the transition periods within different parts of the Congo Basin. These models could therefore be used to test the hypothesis that the equatorial region provides ET to the southern Congo to help initiate its rainy seasons. If the hypothesis is true, then this research would confirm the important of ET in the equatorial region providing moisture to both local and non-local regions, similar to the moisture recycling

cascades that transport moisture from the northern Amazon to the southern Amazon (Staal et al., 2018).

Furthermore, while this work investigates the changes in larger-scale environmental conditions during the transition period that can induce deep convection, smaller-scale processes that control the primary form of deep convection, mesoscale convective systems, within the Congo Basin must still be investigated, which require higher spatial and temporal resolutions of data used. This includes internal cloud processes such as updraft structures and cold pool formation, local environmental interactions such as entrainment-shear interactions with updrafts, and cold pool interactions with the environment (Feng et al., 2022) Many studies have focused on identifying the spatial and temporal patterns of MCSs in the Congo Basin (Jackson et al., 2009, Hartman et al., 2021, Andrews et al., 2023). However, examining these smaller-scale controls on MCS development requires high-resolution, convection-permitting modeling (e.g., Kendon et al., 2019 or ground-based data collection (e.g., Feng et al., 2022), neither of which are well developed in this region.

Finally, the newly developed process understanding of the mechanisms controlling the transition period to the Congo Basin can be used to better understand which mechanisms control rainfall variability, especially as rainfall seasonality within the region is highly unstable (Herrmann and Mohr, 2011). For example, the April-June (AMJ) drought has been linked to changes in the Indian Walker circulation that induce greater subsidence over the equatorial African region (Zhou et al., 2014, Hua et al., 2016; 2018). The AMJ drought has itself been linked to early onsets of the summer dry season within the equatorial African region (Jiang et al., 2019), at the expense of the spring rainy season end. However, mechanisms controlling changes to the onset of the spring rainy season have not yet been studied, and in general, it is unclear

what leads to the temporary shortening or even disappearance of the spring rainy season. In addition, could climate or LCLUC changes lead to an eventual long-term disappearance of the spring rainy season, the weaker of the two rainy seasons in the equatorial region? This must be investigated to better forecast rainfall, which is critical for rain-fed agriculture within the rapidly expanding nations in the Congo.

7.3 Final Remarks

African countries have contributed among the least to the causes of climate change but are experiencing some of the fastest climate-change induced warming and with highly vulnerable population to climate-change impacts (Cabeza et al., 2022, Overland et al., 2021). Between 1990-2020, only 3.8% of global funding for climate-related research was directed towards this continent (Cabeza et al., 2022,). Within the continent, climate-related research in the equatorial regions, which host a major global carbon, water, and energy center and are home to millions of people, remains relatively scarce (Cabeza et al., 2022). My biggest hope for the work presented in this dissertation is that it plays a small part in advancing our understanding of the equatorial African region.

APPENDIX A

Supplementary Materials for Chapter 4

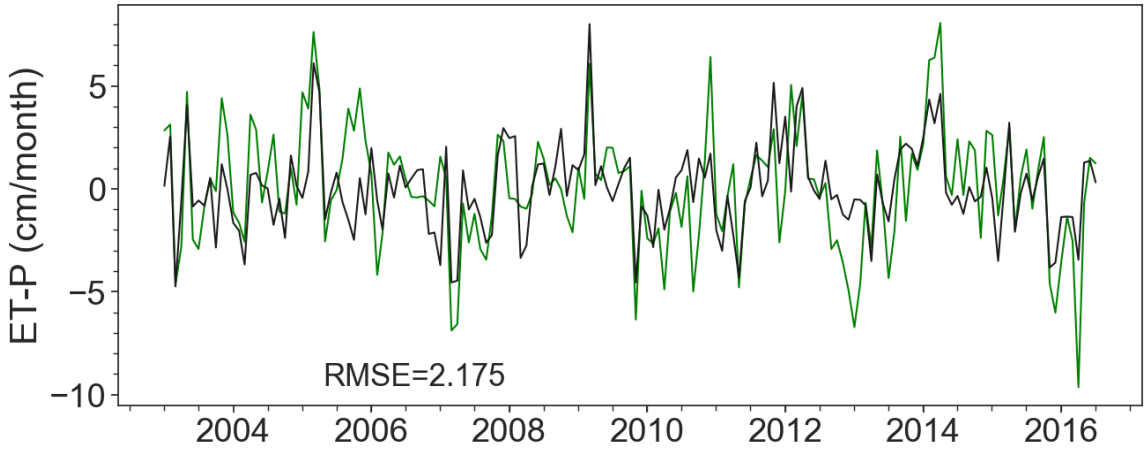

Figure A.1: Basin-scale $ET - P$ IAVs from ICAM. Monthly scale.

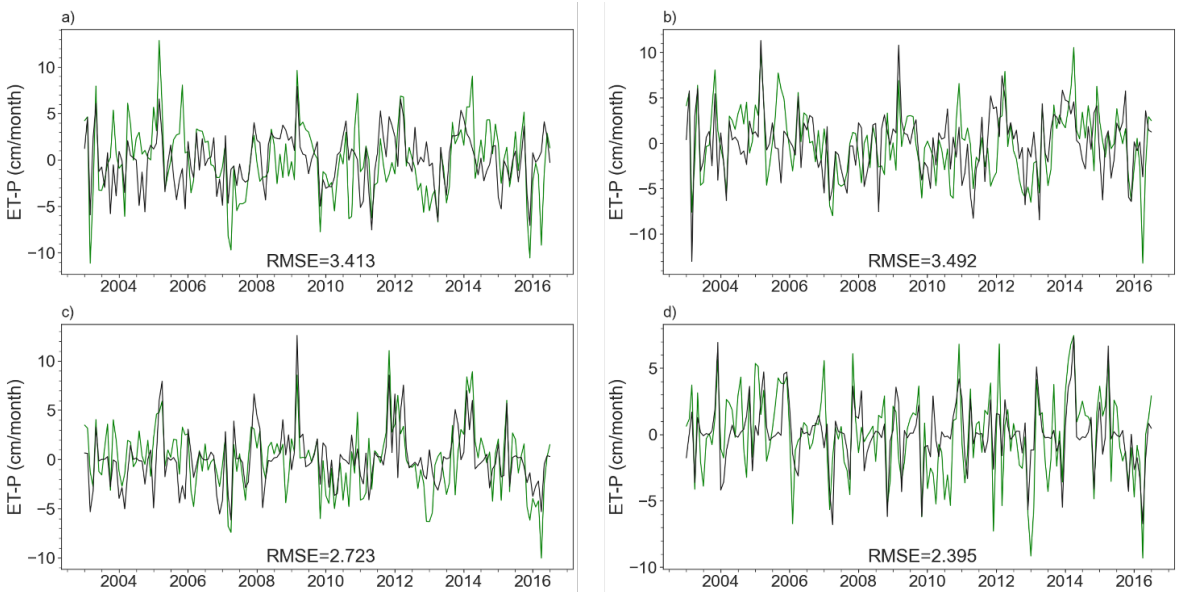

Figure A.2: Quadrant-Scale $ET - P$ IAVs from ICAM on a monthly scale: a) $Quad_{NW}$; b) $Quad_{NE}$; c) $Quad_{SW}$; d) $Quad_{SE}$

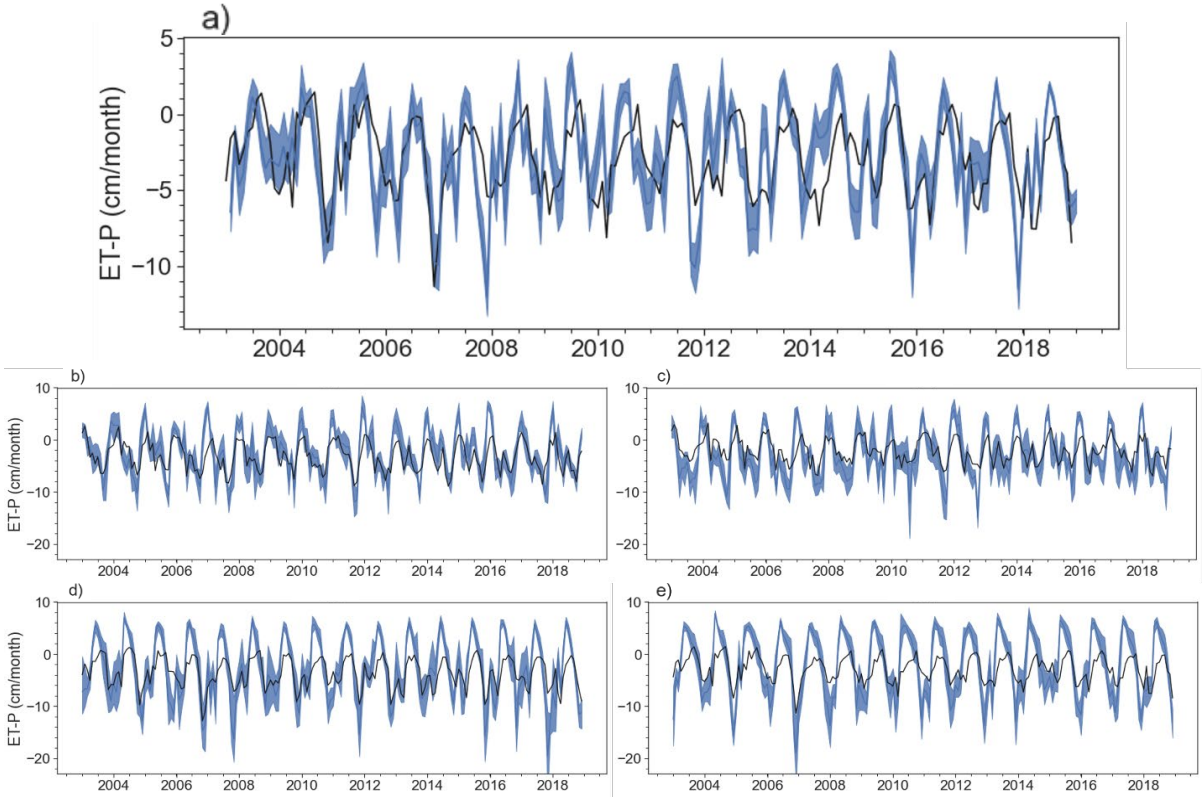

Figure A.3: Comparison of regression-based $ET - P$ (black line) to $ET - P$ calculated using different ET and P datasets. Shaded blue represents the maximum and minimum $ET - P$ from the different datasets, and dark blue line represents the mean $ET - P$ from the different datasets for: a) basin-scale; b) $Quad_{NW}$; c) $Quad_{NE}$; d)$Quad_{SW}$; and e) $Quad_{SE}$

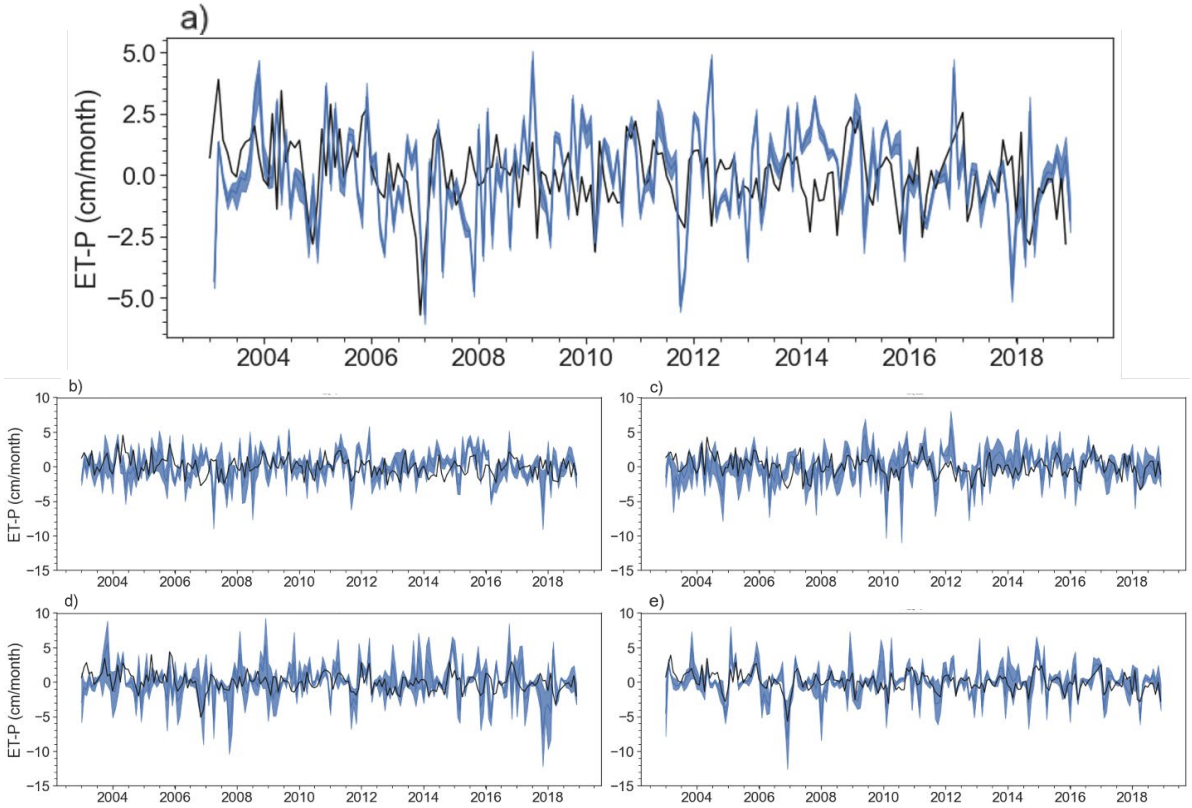

Figure A.4: Like Figure S3, except for the IAVs instead of the multi-year record for: a) basin-scale; b) $Quad_{NW}$; c) $Quad_{NE}$; d)$Quad_{SW}$; and e) $Quad_{SE}$

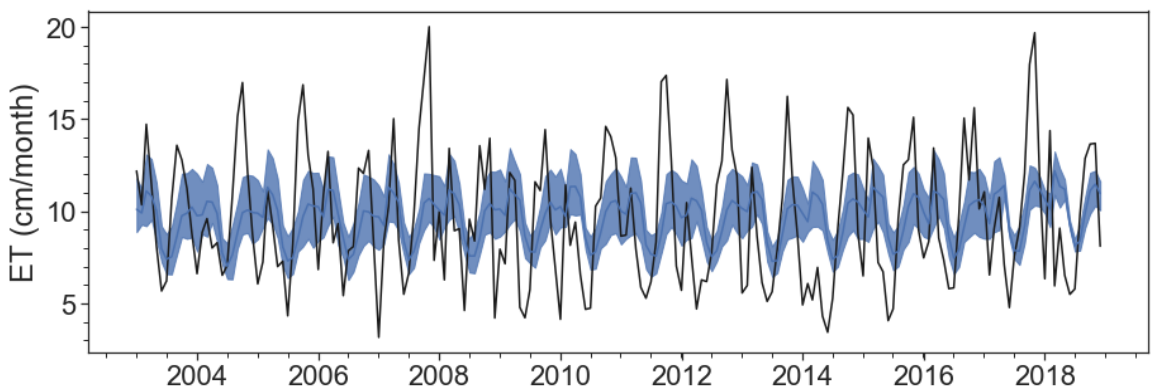

Figure A.5: Comparison of regression-based ET (black line) to ET from different datasets. Shaded blue represents the maximum and minimum ET from the different datasets, and dark blue line represents the mean ET from the different datasets. Basin-scale.

APPENDIX B

Supplementary Material for Chapter 5

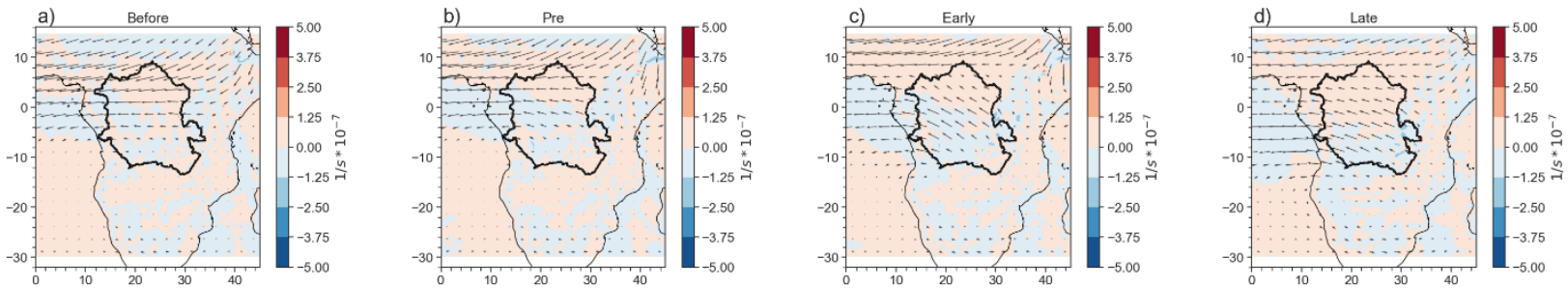

Figure B.1: Moisture transport and moisture convergence at 650 hPa for a) the “before” period; b) the pre-transition; c) the early-transition, and d) the late transition period.

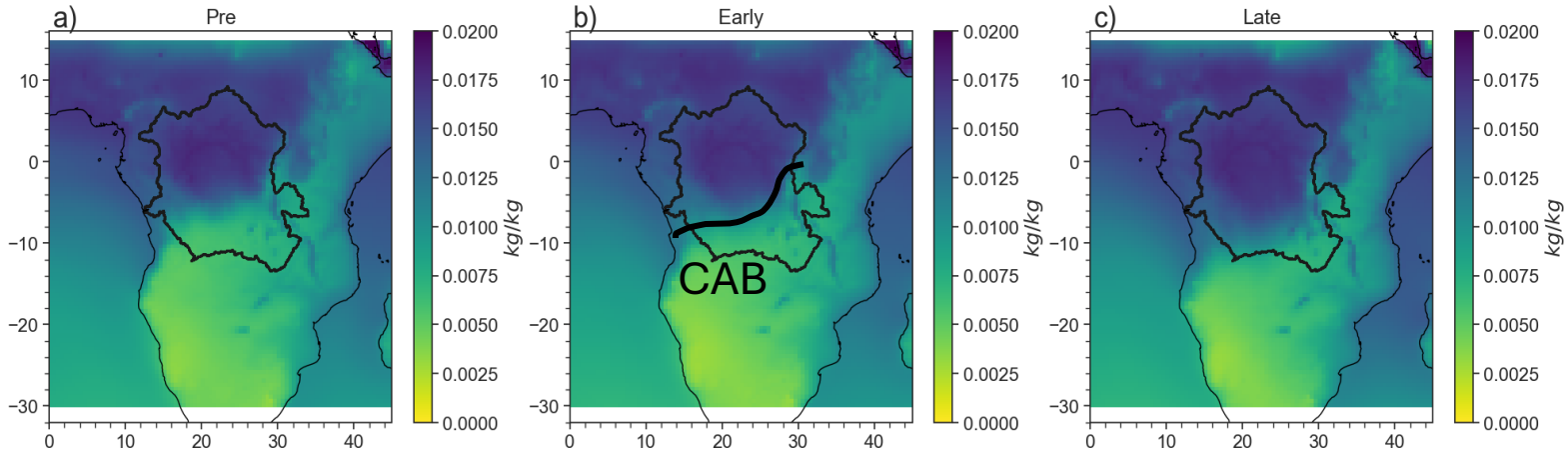

Figure B.2: Surface specific humidity from ERA5 for a) the pre-transition period; b) the early-transition period; and c) the late-transition period. The sharp diagonal gradient in surface humidity denotes the rough position of the Congo Air Boundary (CAB).

APPENDIX C

Supplementary Material for Chapter 6

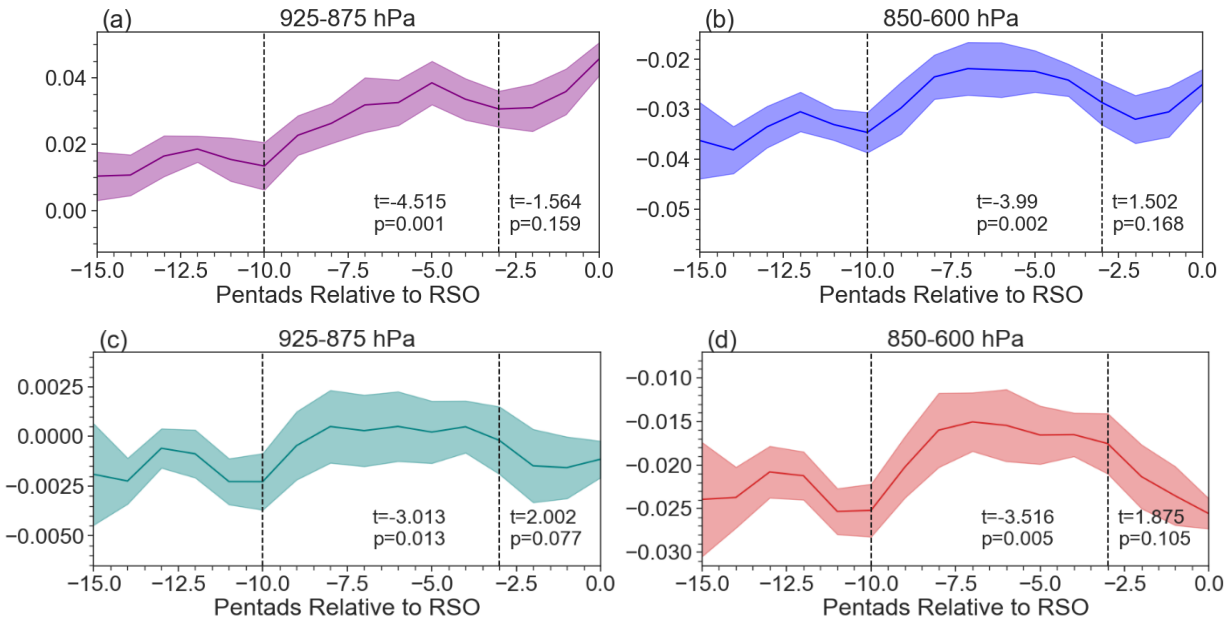

Figure C.1: q*u averaged between a) 925-875 hPa across the western boundary; b) 850-600 hPa across the western boundary; c) 925-875 hPa across the eastern boundary; and d) 850-600 hPa across the eastern boundary. Positive values across the western boundary indicates moisture entering the basin; positive values across the eastern boundary indicate moisture leaving the basin. For the transition to the Spring RSO. A Welch's t-test was computed between the "before" and early transition, as well as between the early and late transition period. p values less than 0.05 indicate that the means of the early and late periods are statistically different from that of the before and early periods, respectively. Shades represents the standard error of the mean of the different years.

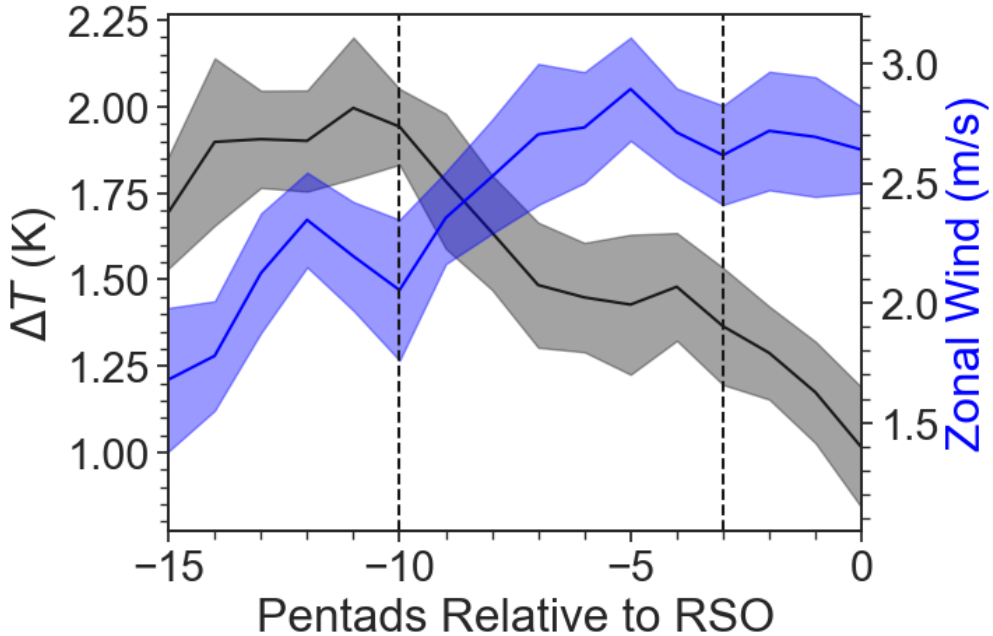

Figure C.2: Land-ocean zonal temperature (black line) gradient of near-surface (925 hPa) temperature: T_{ocean} is averaged between $5°S - 5°N\ and\ 5°W - 5°E$. T_{land} is averaged between $5°S - 5N$ and $10 - 15°E$. Zonal wind (blue line) averaged between $5°S - 5°N$ and $10° - 15°E$. Shades represents the standard error of the mean of the different years. Prior to the spring RSO.

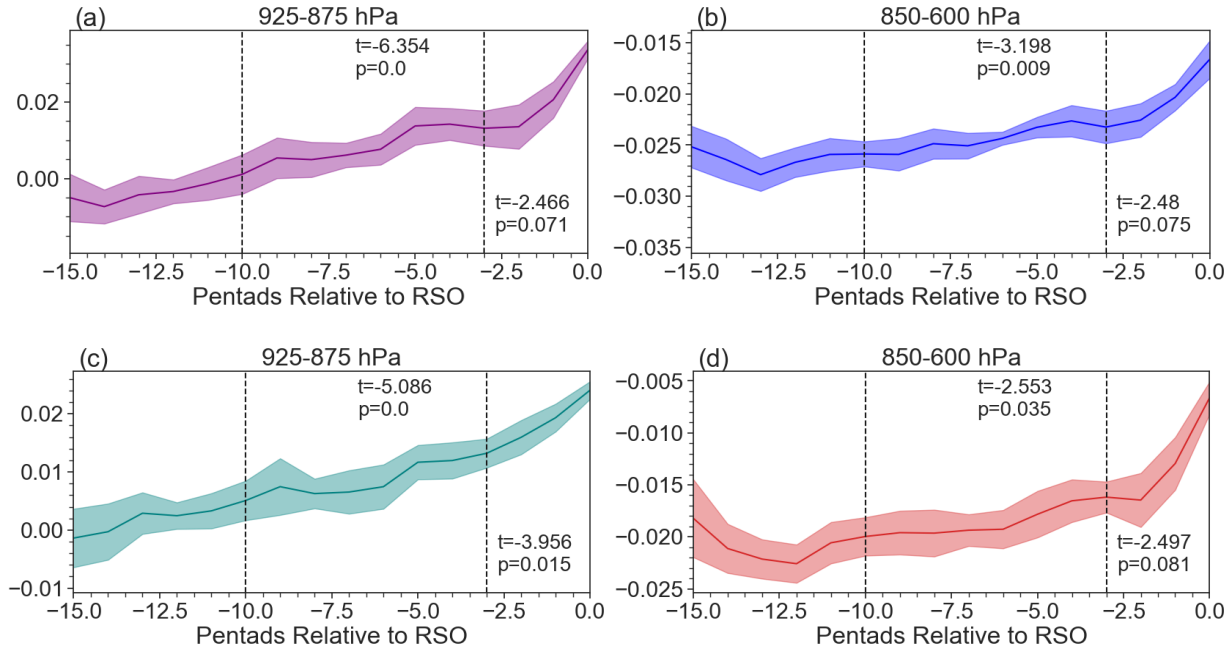

Figure C.3: q*v averaged between a) 925-875 hPa across the northern boundary of the equatorial region; b) 850-600 hPa across the northern boundary; c) 925-875 hPa across the southern boundary of the equatorial region; and d) 850-600 hPa across the southern boundary. Positive values across the northern boundary indicate moisture leaving the basin; positive values across the southern boundary indicate moisture entering the basin. A Welch's t-test was computed between the "before" and early transition, as well as between the early and late transition period. p values less than 0.05 indicate that the means of the early and late periods are statistically different from that of the before and early periods, respectively. For the transition to the Spring RSO. Shades represents the standard error of the mean of the different years.

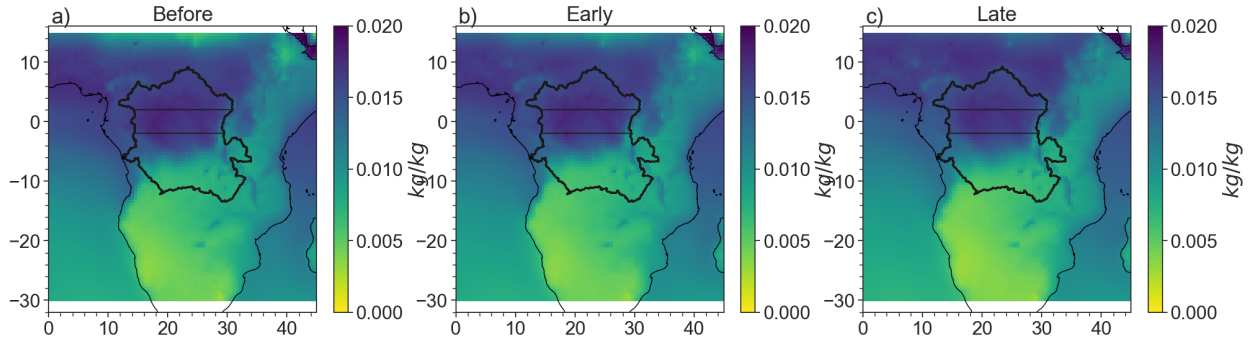

Figure C.4: Specific humidity at 1000 hPa prior to the fall rainy season during the a) "before," (19-15 pentads prior to the Fall RSO) b) Early, and c) Late transition periods.

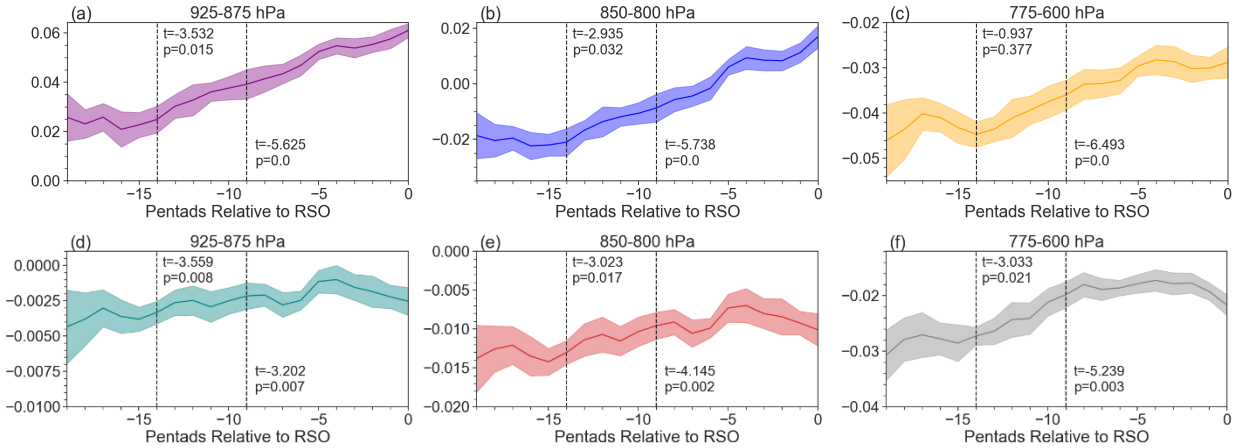

Figure C.5: q*u averaged between a) 925-875 hPa across the western boundary of the equatorial region; b) 850-800 hPa across the western boundary; c) 775-600 hPa across the western boundary of the equatorial region; d) 925-875 hPa across the eastern boundary; e) 850-800 hPa across the eastern boundary; and f) 775-600 hPa across the eastern boundary. Positive values across the western boundaries indicate moisture entering the basin; positive values across the eastern boundary indicate moisture leaving the basin. For the transition to the Fall RSO. A Welch's t-test was computed between the "before" and early transition, as well as between the early and late transition period. p values less than 0.05 indicate that the means of the early and late periods are statistically different from that of the before and early periods, respectively.

Bibliography

Adams, C. E., & Garcia-Carreras, L. (2023). Detection of land-use change and rapid recovery of vegetation after deforestation in the Congo Basin. Earth Interactions, 1-25. https://doi.org/10.1175/EI-D-22-0020.1.

Adebiyi, A. A., & Zuidema, P. (2016). The role of the southern African easterly jet in modifying the southeast Atlantic aerosol and cloud environments. Quarterly Journal of the Royal Meteorological Society, 142(697), 1574-1589. 04?

Alber, K., Zhou, L., & Raghavendra, A. (2021). A shift in the diurnal timing and intensity of deep convection over the Congo Basin during the past 40 years. *Atmospheric Research*, *264*, 105869. https://doi.org/10.1016/j.atmosres.2021.105869

Alsdorf, D., Beighley, E., Laraque, A., Lee, H., Tshimanga, R., O'Loughlin, F., et al. (2016). Opportunities for hydrologic research in the Congo Basin. *Reviews of Geophysics*, 54(2), 378–409. https://doi.org/10.1002/2016RG000517

Andela, N., Morton, D. C., Giglio, L., Paugam, R., Chen, Y., Hantson, S., et al. (2019). The Global Fire Atlas of individual fire size, duration, speed and direction. Earth Syst. Sci. Data, 11, 529–552. https://doi.org/10.5194/essd-11-529-2019.

Andela, N. & Guido R. van der Werf, (2014). Recent trends in African fires driven by cropland expansion and El Niño to La Niña transition. Nature, 4. 791-795. 10.1038/nclimate2313.

Andrews, P. C., Cook, K. H., & Vizy, E. K. (2024). Mesoscale convective systems in the Congo Basin: seasonality, regionality, and diurnal cycles. *Climate Dynamics*, *62*(1), 609-630. https://doi.org/10.1007/s00382-023-06903-7

Aragão, L. E. O., Malhi, Y., Roman-Cuesta, R. M., Saatchi, S., Anderson, L. O., & Shimabukuro, Y. E. (2007). Spatial patterns and fire response of recent Amazonian droughts. Geophysical Research Letters, *34*(7). https://doi.org/10.1029/2006GL028946

Asefi-Najafabady, S., & Saatchi, S. (2013). Response of African humid tropical forests to recent rainfall anomalies. Philosophical Transactions of the Royal Society B: Biological Sciences, 368(1625), 20120306. https://doi.org/10.1098/rstb.2012.0306

Ashouri, H., Hsu, K., Sorooshian, S., Braithwaite, D. K., Knapp, K. R., Cecil, L. D., et al. (2015). PERSIANN-CDR: Daily Precipitation Climate Data Record from Multisatellite Observations for Hydrological and Climate Studies, Bulletin of the American Meteorological Society, 96(1), 69-83. https://doi.org/10.1175/BAMS-D-13-00068.1.

Attwood, K., Washington, R., & Munday, C. (2024). The Southern African Heat Low: Structure, Seasonal and Diurnal Variability, and Climatological Trends. Journal of Climate. https://doi.org/10.1175/JCLI-D-23-0522.1

Aumann, H. H., Broberg, S., Manning, E., & Pagano, T. (2019). Radiometric Stability Validation of 17 Years of AIRS Data Using Sea Surface Temperatures. Geophysical Research Letters, 46, 12504– 12510. https://doi.org/10.1029/2019GL085098.

Azarderakhsh, M., Rossow, W. B., Papa, F., Norouzi, H., & Khanbilvardi, R. (2011). Diagnosing water variations within the Amazon basin using satellite data. J. Geophys. Res., 116, D24107. 10.1029/2011JD015997.

Bailey, A., Blossey, P. N., Noone, D., Nusbaumer, J., & Wood, R. (2017). Detecting shifts in tropical moisture imbalances with satellite-derived isotope ratios in water vapor. *Journal of Geophysical Research: Atmospheres*, 122(11), 5763–5779. https://doi.org/10.1002/2016JD026222

Baker, J. C. A., Garcia-Carreras, L., Gloor, M., Marsham, J. H., Buermann, W., da Rocha, H. R., et al. (2021). Evapotranspiration in the Amazon: spatial patterns, seasonality, and recent trends in observations, reanalysis, and climate models. Hydrol. Earth Syst. Sci., 25, 2279–2300. https://doi.org/10.5194/hess-25-2279-202.

Balas, N., Nicholson, S. E., & Klotter, D. (2007). The relationship of rainfall variability in West Central Africa to sea-surface temperature fluctuations. *International Journal of Climatology*, 27(10), 1335–1349. https://doi.org/10.1002/joc.1456

Bauters, M., Drake, T. W., Verbeeck, H., Bodé, S., Hervé-Fernández, P., Zito, et al. (2018). High fire-derived nitrogen deposition on central African forests. Proceedings of the National Academy of Sciences, 115(3), 549-554. https://doi.org/10.1073/pnas.1714597115.

Bauters, M., Drake, T. W., Wagner, S., Baumgartner, S., Makelele, I. A., Bodé, S., et al. (2021). Fire-derived phosphorus fertilization of African tropical forests. Nature communications, 12(1), 1-8. https://doi.org/10.1038/s41467-021-25428-3.

Beaudoing, H. & M. Rodell, NASA/GSFC/HSL (2019), GLDAS Noah Land Surface Model L4 monthly 0.25 x 0.25 degree V2.0, Greenbelt, Maryland, USA, Goddard Earth Sciences Data and Information Services Center (GES DISC). 10.5067/9SQ1B3ZXP2C5.

Bele, M.Y., Sonwa, D.J., & Tiani, A.M. (2015). Adapting the Congo Basin forests management to climate change: Linkages among biodiversity, forest loss, and human well-being. Forest Policy and Economics, 50, 1-10. https://doi.org/10.1016/j.forpol.2014.05.010.

Bell, J. P., Tompkins, A. M., Bouka-Biona, C., & Sanda, I. S. (2015). A process-based investigation into the impact of the Congo Basin deforestation on surface climate. *Journal of Geophysical Research: Atmospheres*, 120(12), 5721–5739. https://doi.org/10.1002/2014JD022586

Boese, S., Jung, M., Carvalhais, N., & Reichstein, M. (2017). The importance of radiation for semiempirical water-use efficiency models. *Biogeosciences*, 14(12), 3015–3026. https://doi.org/10.5194/bg-14-3015-2017

Bolton, D. (1980). The computation of equivalent potential temperature. Monthly weather review, 108(7), 1046-1053. https://doi.org/10.1175/1520-0493(1980)108<1046:TCOEPT>2.0.CO;2

Breiman, L. Random Forests. Machine Learning 45, 5–32 (2001). https://doi.org/10.1023/A:1010933404324

Bretherton, C. S., Peters, M. E., & Back, L. E. (2004). Relationships between water vapor path and precipitation over the tropical oceans. *Journal of Climate*, 17(7), 1517–1528. https://doi.org/10.1175/1520-0442(2004)017<1517:RBWVPA>2.0.CO;2

Brown, D., Worden, J., & Noone, D. (2008). Comparison of atmospheric hydrology over convective continental regions using water vapor isotope measurements from space. *Journal of Geophysical Research*, 113(D15), D15124. https://doi.org/10.1029/2007JD009676

Brummett, R.E., C. Tanania, A. Pandi, J. Ladel, Y. Munzimi, A. Russell, et al. (2009). Ressources en eau et biens et services liés à l'écosystème forestier. In: Wasseige, C., Devers, D., de Marcen, P., Eba'a Atyi, R., Nasi, R., & Mayaux, P. (Eds.) Les forêts du Bassin du Congo. Office des publications de l'Union européenne, Luxembourg. 10.2788/32456.

Burnett, M. W., Quetin, G. R., & Konings, A. G. (2020). Data-driven estimates of evapotranspiration and its controls in the Congo Basin. *Hydrology and Earth System Sciences*, 24(8), 4189–4211. https://doi.org/10.5194/hess-24-4189-2020

Cabeza, L. F., Q. Bai, P. Bertoldi, J.M. Kihila, A.F.P. Lucena, É. Mata, S. Mirasgedis, A. Novikova, Y. Saheb, 2022: Buildings. In IPCC, 2022*: Climate Change 2022: Mitigation of Climate Change. Contribution of Working Group III to the Sixth Assessment Report of the Intergovernmental Panel on Climate Change* [P.R. Shukla, J. Skea, R. Slade, A. Al Khourdajie, R. van Diemen, D. McCollum, M. Pathak, S. Some, P. Vyas, R. Fradera, M. Belkacemi, A. Hasija, G. Lisboa, S. Luz, J. Malley, (eds.)]. Cambridge University Press, Cambridge, UK and New York, NY, USA. doi: 10.1017/9781009157926.011

Chakraborty, S., Jiang, J. H., Su, H., & Fu, R. (2020). Deep convective evolution from shallow clouds over the Amazon and Congo rainforests. Journal of Geophysical Research: Atmospheres, 125(1), e2019JD030962. https://doi.org/10.1029/2019JD030962

Chakraborty, S., Jiang, J. H., Su, H., & Fu, R. (2021). On the role of aerosol radiative effect in the wet season onset timing over the Congo rainforest during boreal autumn. Atmospheric Chemistry and Physics, 21(17), 12855-12866. https://doi.org/10.5194/acp-21-12855-2021.

Chambers, J. Q., Asner, G., Morton, D., Anderson, L., Saatchi, S., Espírito-Santo,F., et al. (2007). Regional ecosystem structure and function: Ecological insights from remote sensing of tropical forests. Trends Ecol. Evol. 22, 414–423. 10.1016/j.tree.2007.05.001.

Chen, T. C. (2005). Maintenance of the midtropospheric North African summer circulation: Saharan high and African easterly jet. *Journal of climate*, *18*(15), 2943-2962. https://doi.org/10.1175/JCLI3446.1

Chu, D. A., Kaufman, Y. J., Ichoku, C., Remer, L. A., Tanré, D., & Holben, B. N. (2002). Validation of MODIS aerosol optical depth retrieval over land. Geophysical Research Letters, 29(12), MOD2-1. https://doi.org/10.1029/2001GL013205

Cook, K. H., Liu, Y., & Vizy, E. K. (2020). Congo Basin drying associated with poleward shifts of the African thermal lows. *Climate Dynamics*, *54*, 863-883. https://doi.org/10.1007/s00382-019-05033-3

Cook, K. H., & Vizy, E. K. (2016). The Congo Basin Walker circulation: Dynamics and connections to precipitation. *Climate Dynamics*, 47(3–4), 697–717. https://doi.org/10.1007/s00382-015-2864-y

Cook, K. H., & Vizy, E. K. (2022). Hydrodynamics of regional and seasonal variations in Congo Basin precipitation. Climate Dynamics, 59(5-6), 1775-1797. https://doi.org/10.1007/s00382-021-06066-3

Creese, A., Washington, R., & Jones, R. (2019). Climate change in the Congo Basin: processes related to wetting in the December–February dry season. *Climate Dynamics*, *53*, 3583-3602. https://doi.org/10.1007/s00382-019-04728-x

Crowhurst, D., Dadson, S., Peng, J., & Washington, R. (2020). Contrasting controls on Congo Basin evaporation at the two rainfall peaks. *Climate Dynamics*, 56(5), 1609–1624. https://doi.org/10.1007/s00382-020-05547-1

Dai, A. (2013). Increasing drought under global warming in observations and models. *Nature Climate Change*, 3(1), 52–58. https://doi.org/10.1038/nclimate1633

Danabasoglu, G., Lamarque, J.-F., Bacmeister, J., Bailey, D. A., DuVivier, A. K., Edwards, J., et al. (2020). The Community Earth System Model Version 2 (CESM2). Journal of Advances in Modeling Earth Systems, 12, e2019MS001916. https://doi.org/10.1029/2019MS001916.

Dargie, G., Lewis, S., Lawson, I.., Mitchard, E.T.A., Page, S., Bocko, Y., et al. (2017) Age, extent and carbon storage of the central Congo Basin peatland complex. Nature 542, 86–90. https://doi.org/10.1038/nature21048.

Davis, K.T., Dobrowski, S.Z., Holden, Z.A., Higuera, P.E. and Abatzoglou, J.T. (2019), Microclimatic buffering in forests of the future: the role of local water balance. Ecography, 42: 1-11. https://doi.org/10.1111/ecog.03836.

Dee, D. P., Uppala, S. M., Simmons, A. J., Berrisford, P., Poli, P., Kobayashi, S., et al. (2011). The ERA-Interim reanalysis: Configuration and performance of the data assimilation system. *Quarterly Journal of the Royal Meteorological Society*, 137(656), 553–597. https://doi.org/10.1002/qj.828

Defourny, P., Lamarche, C., Bontemps, S., De Maet, T., Van Bogaert, E., Moreau, I., et al. (2017). *Land cover climate change initiative: Product user guide v2. Issue 2.0*. Retrieved from http://maps.elie.ucl.ac.be/CCI/viewer/download/ESACCI-LC-Ph2-PUGv2_2.0.pdf

De Sales, F., Okin, G. S., Xue, Y., & Dintwe, K. (2019). On the effects of wildfires on precipitation in Southern Africa. Climate dynamics, 52, 951-967. https://doi.org/10.1007/s00382-018-4174-7

DeSouza-Machado, S., Strow, L. L., Tangborn, A., Huang, X., Chen, X., Liu, X., Wu, W., and Yang, Q. (2018). Single-footprint retrievals for AIRS using a fast TwoSlab cloud-representation model and the SARTA all-sky infrared radiative transfer algorithm. Atmos. Meas. Tech., 11, 529–550. https://doi.org/10.5194/amt-11-529-2018

Dezfuli, A. (2017). Climate of Western and Central Equatorial Africa. Oxford Research Encyclopedia of Climate Science. https://doi.org/10.1093/acrefore/9780190228620.013.511

Diem, J. E., Ryan, S. J., Hartter, J., & Palace, M. W. (2014). Satellite-based rainfall data reveal a recent drying trend in central equatorial Africa. *Climatic Change*, 126, 263–272. https://doi.org/10.1007/s10584-014-1217-x

Doelling, D. R., N. G. Loeb, D. F. Keyes, M. L. Nordeen, D. Morstad, C. Nguyen, B. A. Wielicki, D. F. Young, M. Sun. (2013). Geostationary Enhanced Temporal Interpolation for CERES Flux Products, Journal of Atmospheric and Oceanic Technology, **30**(6), 1072-1090. doi: 10.1175/JTECH-D-12-00136.1.

Doelling, D. R., M. Sun, L. T. Nguyen, M. L. Nordeen, C. O. Haney, D. F. Keyes, P. E. Mlynczak. (2016). Advances in Geostationary-Derived Longwave Fluxes for the CERES Synoptic (SYN1deg) Product, Journal of Atmospheric and Oceanic Technology, 33(3), 503-521. doi: 10.1175/JTECH-D-15-0147.1

Dong, G., Zhao, F.Y., Chen, J.Q., Zhang, Y.Q., & Shao, C.L. (2020). Non-climatic component provoked substantial spatiotemporal changes of carbon and water use efficiency on the Mongolian Plateau. Environ. Res. Lett. 15, 095009–095025. 10.1088/1748-9326/ab9692.

Dosio, A., Jury, M. W., Almazroui, M., Ashfaq, M., Diallo, I., Engelbrecht, F. A., ... & Tamoffo, A. T. (2021). Projected future daily characteristics of African precipitation based on global (CMIP5, CMIP6) and regional (CORDEX, CORDEX-CORE) climate models. *Climate Dynamics*, *57*(11), 3135-3158. https://doi.org/10.1007/s00382-021-05859-w

Duncan, B. N., Martin, R. V., Staudt, A. C., Yevich, R., & Logan, J. A. (2003). Interannual and seasonal variability of biomass burning emissions constrained by satellite observations. Journal of Geophysical Research: Atmospheres, 108(D2), ACH-1. https://doi.org/10.1029/2002JD002378

Dyer, E. L. E., Jones, D. B. A., Nusbaumer, J., Li, H., Collins, O., Vettoretti, G., & Noone, D. (2017). Congo Basin precipitation: Assessing seasonality, regional interactions, and sources of moisture. Journal of Geophysical Research: Atmospheres, 122(13), 6882–6898. https://doi.org/10.1002/2016JD026240.

Eltahir, E. A. B., & Bras, R. L. (1996). Precipitation recycling. *Reviews of Geophysics*, 34(3), 367–378. https://doi.org/10.1029/96RG01927

Farnsworth, A., White, E., Williams, C. J., Black, E., & Kniveton, D. R. (2011). Understanding the large scale driving mechanisms of rainfall variability over Central Africa. African climate and climate change: physical, social and political perspectives, 101-122. https://doi.org/10.1007/978-90-481-3842-5_5

Fekete, B. M., Vörösmarty, C. J., Roads, J. O., & Willmott, C. J. (2004). Uncertainties in precipitation and their impacts on runoff estimates. *Journal of Climate*, 17(2), 294–304. https://doi.org/10.1175/1520-0442(2004)017<0294:UIPATI>2.0.CO;2

Feng, H., & Zhang, M. (2015). Global land moisture trends: drier in dry and wetter in wet over land. Scientific reports, 5(1), 1-6. https://doi.org/10.1038/srep18018

Feng, Z., Varble, A., Hardin, J., Marquis, J., Hunzinger, A., Zhang, Z., & Thieman, M. (2022). Deep convection initiation, growth, and environments in the complex terrain of Central Argentina during CACTI. *Monthly Weather Review*, *150*(5), 1135-1155. https://doi.org/10.1175/MWR-D-21-0237.1

Fernandes, K., Fu, R., & Betts, A. K. (2008). How well does the ERA40 surface water budget compare to observations in the Amazon River basin? *Journal of Geophysical Research*, 113(D11), D11117. https://doi.org/10.1029/2007JD009220

Fisher, J. B., Malhi, Y., Bonal, D., Da Rocha, H. R., De Araújo, A. C., Gamo, M., et al. (2009). The land-atmosphere water flux in the tropics. *Global Change Biology*, 15(11), 2694–2714. https://doi.org/10.1111/j.1365-2486.2008.01813.x

Fisher, J. B., Tu, K. P., & Baldocchi, D. D. (2008). Global estimates of the land-atmosphere water flux based on monthly AVHRR and ISLSCP-II data, validated at 16 FLUXNET sites. Remote Sensing of Environment, 112(3), 901–919. https://doi.org/10.1016/j.rse.2007.06.025.

Frankenberg, C., Fisher, J. B., Worden, J., Badgley, G., Saatchi, S. S., Lee, J.-E., et al. (2011). New global observations of the terrestrial carbon cycle from GOSAT: Patterns of plant fluorescence with gross primary productivity. *Geophysical Research Letters*, 38(17). https://doi.org/10.1029/2011GL048738

Fu, R., Del Genio, A. D., & Rossow, W. B. (1990). Behavior of deep convective clouds in the tropical Pacific deduced from ISCCP radiances. Journal of climate, 3(10), 1129-1152. https://doi.org/10.1175/1520-0442(1990)003<1129:BODCCI>2.0.CO;2

Fu, R., Zhu, B., & Dickinson, R. E. (1999). How do atmosphere and land surface influence seasonal changes of convection in the tropical Amazon?. Journal of Climate, 12(5), 1306-1321. https://doi.org/10.1175/1520-0442(1999)012<1306:HDAALS>2.0.CO;2

Fuller, T. L., Narins, T. P., Nackoney, J., Bonebrake, T. C., Sesink Clee, P., Morgan, K., et al. (2019). Assessing the impact of China's timber industry on Congo Basin land use change. Area, 51(2), 340–349. https://doi.org/10.1111/AREA.12469.

Fung, I. Y., Doney, S. C., Lindsay, K., & John, J. (2005). Evolution of carbon sinks in a changing climate. Proceedings of the National Academy of Sciences, 102(32), 11201-11206. https://doi.org/10.1073/pnas.0504949102.

Funk, C., Peterson, P., Landsfeld, M., Pedreros, D., Verdin, J., Shukla, S., et al. (2015). The climate hazards infrared precipitation with stations—a new environmental record for monitoring extremes. Scientific data, 2(1), 1-21. https://doi.org/10.1038/sdata.2015.66.

Galewsky, J. (2018). Using stable isotopes in water vapor to diagnose relationships between lower-tropospheric stability, mixing, and low-cloud cover near the island of Hawaii. *Geophysical Research Letters*, 45(1), 297–305. https://doi.org/10.1002/2017GL075770

Galewsky, J., & Hurley, J. V. (2010). An advection-condensation model for subtropical water vapor isotopic ratios. *Journal of Geophysical Research*, 115(D16), D16116. https://doi.org/10.1029/2009JD013651

Galewsky, J., Steen-Larsen, H. C., Field, R. D., Worden, J., Risi, C., & Schneider, M. (2016). Stable isotopes in atmospheric water vapor and applications to the hydrologic cycle. *Reviews of Geophysics*, 54(4), 809–865. https://doi.org/10.1002/2015RG000512

Gelaro, R., McCarty, W., Suárez, M. J., Todling, R., Molod, A., Reichle, K. W., ... & Zhao, B. (2017). The modern-era retrospective analysis for research and applications. https://doi.org/10.1175/JCLI-D-16-0758.1

Gentine, P., Massmann, A., Lintner, B. R., Hamed Alemohammad, S., Fu, R., Green, J. K., et al. (2019). Land–atmosphere interactions in the tropics–a review. Hydrology and Earth System Sciences, 23(10), 4171-4197. https://doi.org/10.5194/hess-23-4171-2019.

Giglio, L., Randerson, J. T., & Van Der Werf, G. R. (2013). Analysis of daily, monthly, and annual burned area using the fourth-generation global fire emissions database (GFED4). Journal of Geophysical Research: Biogeosciences, 118(1), 317-328. https://doi.org/10.1002/jgrg.20042

Green, J., Konings, A., Alemohammad, S., Berry, J., Entekhabi, D., Kolassa, J., et al. (2017). Regionally strong feedbacks between the atmosphere and terrestrial biosphere. Nature Geosci 10, 410–414. https://doi.org/10.1038/ngeo2957.

Guan, K., Pan, M., Li, H., Wolf, A., Wu, J., Medvigy, D., et al. (2015). Photosynthetic seasonality of global tropical forests constrained by hydroclimate. Nature Geosci 8, 284–289. https://doi.org/10.1038/ngeo2382.

Hakamada, R., Hubbard, R., Stape, J.,Lima, W., Moreira, & G., Ferraz, S. (2020). Stocking effects on seasonal tree transpiration and ecosystem water balance in a fast-growing Eucalyptus plantation in Brazil. Forest Ecology and Management, 466, 118149. 10.1016/j.foreco.2020.118149.

Haensler, A., Saeed, F., & Jacob, D. (2013). Assessing the robustness of projected precipitation changes over central Africa on the basis of a multitude of global and regional climate projections. *Climatic Change*, *121*, 349-363. https://doi.org/10.1007/s10584-013-0863-8

Hart, N. C., Washington, R., & Maidment, R. I. (2019). Deep convection over Africa: Annual cycle, ENSO, and trends in the hotspots. Journal of Climate, 32(24), 8791-8811. https://doi.org/10.1175/JCLI-D-19-0274.1

Hartman, A. T. (2021). Tracking mesoscale convective systems in central equatorial Africa. *International Journal of Climatology*, *41*(1), 469-482. https://doi.org/10.1002/joc.6632

Hastenrath, S. (2007). Circulation mechanisms of climate anomalies in East Africa and equatorial Indian Ocean. Dynamics of Atmospheres and Oceans. 43. 25-35. 10.1016/j.dynatmoce.2006.06.002.

Herrmann, S. M., & Mohr, K. I. (2011). A continental-scale classification of rainfall seasonality regimes in Africa based on gridded precipitation and land surface temperature products. *Journal of Applied Meteorology and Climatology*, *50*(12), 2504-2513. https://doi.org/10.1175/JAMC-D-11-024.1

Hersbach, H., Bell, B., Berrisford, P., Hirahara, S., Horányi, A., Muñoz-Sabater, J., et al. (2020). The ERA5 global reanalysis. *Quarterly Journal of the Royal Meteorological Society*, 146(730), 1999–2049. https://doi.org/10.1002/QJ.3803

Hodnebrog, Ø., Myhre, G., Forster, P. M., Sillmann, J., & Samset, B. H. (2016). Local biomass burning is a dominant cause of the observed precipitation reduction in southern Africa. Nature Communications, 7(1), 11236. 10.1038/ncomms11236

Hoerling, M., Hurrell, J., Eischeid, J., & Phillips, A. (2006). Detection and attribution of twentieth-century northern and southern African rainfall change. *Journal of Climate*, 19(16), 3989–4008. https://doi.org/10.1175/JCLI3842.1

Holloway, C. E., & Neelin, J. D. (2009). Moisture vertical structure, column water vapor, and tropical deep convection. *Journal of the Atmospheric Sciences*, 66(6), 1665–1683. https://doi.org/10.1175/2008JAS2806.1

Hosking, J. S., Russo, M. R., Braesicke, P., & Pyle, J. A. (2010). Modelling deep convection and its impacts on the tropical tropopause layer. Atmospheric Chemistry and Physics, 10(22), 11175-11188. https://doi.org/10.5194/acp-10-11175-2010

Howard, E., & Washington, R. (2018). Characterizing the synoptic expression of the Angola low. *Journal of Climate*, *31*(17), 7147-7165. https://doi.org/10.1175/JCLI-D-18-0017.1

Howard, E., & Washington, R. (2019). Drylines in southern Africa: Rediscovering the Congo air boundary. *Journal of Climate*, *32*(23), 8223-8242. https://doi.org/10.1175/JCLI-D-19-0437.1

Howard, E., Washington, R., & Hodges, K. I. (2019). Tropical lows in southern Africa: Tracks, rainfall contributions, and the role of ENSO. *Journal of Geophysical Research: Atmospheres*, *124*(21), 11009-11032. https://doi.org/10.1029/2019JD030803

Hua, W., Zhou, L., Chen, H., Nicholson, S. E., Raghavendra, A., & Jiang, Y. (2016). Possible causes of the Central Equatorial African long-term drought. *Environmental Research Letters*, 11(12). https://doi.org/10.1088/1748-9326/11/12/124002

Hua, W., Zhou, L., Nicholson, S. E., Chen, H., & Qin, M. (2019). Assessing reanalysis data for understanding rainfall climatology and variability over Central Equatorial Africa. *Climate Dynamics*, 53(1–2), 651–669. https://doi.org/10.1007/s00382-018-04604-0

Huffman, G. J., Bolvin, D. T., Nelkin, E. J., Wolff, D. B., Adler, R. F., Gu, G., et al. (2007). The TRMM multisatellite precipitation analysis (TMPA): Quasi-global, multiyear, combined-sensor precipitation estimates at fine scales. *Journal of Hydrometeorology*, 8(1), 38–55. https://doi.org/10.1175/JHM560.1

Irion, F. W., Kahn, B. H., Schreier, M. M., Fetzer, E. J., Fishbein, E., Fu, D., Kalmus, P., Wilson, R. C., Wong, S., and Yue, Q. (2018). Single-footprint retrievals of temperature, water vapor and cloud properties from AIRS,.Atmos. Meas. Tech., 11, 971–995. https://doi.org/10.5194/amt-11-971-2018.

Jackson, B., Nicholson, S. & Klotter, D. (2009). Mesoscale Convective Systems over Western Equatorial Africa and Their Relationship to Large-Scale Circulation. Monthly Weather Review, 137. 10.1175/2008MWR2525.1.

James, R., Washington, R., Abiodun, B., Kay, G., Mutemi, J., Pokam, W., et al. (2018). Evaluating climate models with an African lens. *Bulletin of the American Meteorological Society*, 99(2), 313–336. https://doi.org/10.1175/BAMS-D-16-0090.1

Jiang, X., Albright, R., Creecy, E., Li, K. F., Liang, M. C., Newman, S., ... & Yung, Y. L. (2023). Congo basin rainforest is a net carbon source during the dry season. Earth and Space Science, e2022EA002644. https://doi.org/10.1029/2022EA002644.

Jiang, Y., Zhou, L., Tucker, C. J., Raghavendra, A., Hua, W., Liu, Y. Y., & Joiner, J. (2019). Widespread increase of boreal summer dry season length over the Congo rainforest. *Nature Climate Change*, 9, 617–622. https://doi.org/10.1038/s41558-019-0512-y

Joiner, J., Guanter, L., Lindstrot, R., Voigt, M., Vasilkov, A. P., Middleton, E. M., et al. (2013). Global monitoring of terrestrial chlorophyll fluorescence from moderate-spectral-resolution near-infrared satellite measurements: Methodology, simulations, and application to GOME-2. *Atmospheric Measurement Techniques*, 6(10), 2803–2823. https://doi.org/10.5194/amt-6-2803-2013

Juárez-Orozco, S. M., Siebe, C., & Fernández y Fernández, D. (2017). Causes and effects of forest fires in tropical rainforests: a bibliometric approach. Tropical Conservation Science, 10, 1940082917737207.

Jury, M. R., Matari, E., & Matitu, M. (2009). Equatorial African climate teleconnections. *Theoretical and applied climatology*, *95*, 407-416. https://doi.org/10.1007/s00704-008-0018-4

Kanamitsu, M., Ebisuzaki, W., Woollen, J., Yang, S. K., Hnilo, J. J., Fiorino, M., & Potter, G. L. (2002). Ncep–doe amip-ii reanalysis (r-2). *Bulletin of the American Meteorological Society*, *83*(11), 1631-1644. https://doi.org/10.1175/BAMS-83-11-1631

Kawase, H., Takemura, T., & Nozawa, T. (2011). Impact of carbonaceous aerosols on precipitation in tropical Africa during the austral summer in the twentieth century. Journal of Geophysical Research: Atmospheres, 116(D18). https://doi.org/10.1029/2011JD015933

Kebacho, L. L., & Sarfo, I. (2023). Why Eastern Africa was not dry during the 2020 short rainy season despite La Niña and a negative Indian Ocean Dipole: Interplay between the Madden-Julian Oscillation and La Niña in modulating short rain. *Theoretical and Applied Climatology*, *153*(3), 1191-1201. https://doi.org/10.1007/s00704-023-04519-9

Kendon, E. J., Stratton, R. A., Tucker, S., Marsham, J. H., Berthou, S., Rowell, D. P., & Senior, C. A. (2019). Enhanced future changes in wet and dry extremes over Africa at convection-permitting scale. *Nature communications*, *10*(1), 1794. https://doi.org/10.1038/s41467-019-09776-9

Kenfack, K., Tamoffo, A. T., Djiotang Tchotchou, L. A., & Vondou, D. A. (2023). Assessment of uncertainties in reanalysis datasets in reproducing thermodynamic mechanisms in the moisture budget's provision in the Congo Basin. *Theoretical and Applied Climatology*, *154*(1), 613-626. https://doi.org/10.1007/s00704-023-04576-0

Kitambo, B. M., Papa, F., Paris, A., Tshimanga, R. M., Frappart, F., Calmant, S., ... & Wongchuig, S. (2022). A long-term monthly surface water storage dataset for the Congo basin from 1992 to 2015. *Earth System Science Data Discussions*, 1-39. https://doi.org/10.5194/essd-15-2957-2023

Kleinschroth, F., Laporte, N., Laurance, W.F., Goetz, S.J., & Ghazoul, J. (2019). Road expansion and persistence in forests of the Congo Basin. Nat Sustain 2, 628–634. https://doi.org/10.1038/s41893-019-0310-6

Kobayashi, S., Ota, Y., Harada, Y., Ebita, A., Moriya, M., Onoda, H., ... & Takahashi, K. (2015). The JRA-55 reanalysis: General specifications and basic characteristics. *Journal of the Meteorological Society of Japan. Ser. II*, *93*(1), 5-48. https://doi.org/10.2151/jmsj.2015-001

Kuete, G., Pokam Mba, W., & Washington, R. (2020). African Easterly Jet South: control, maintenance mechanisms and link with Southern subtropical waves. Climate Dynamics, 54(3-4), 1539-1552. https://doi.org/10.1007/s00382-019-05072-w

Lacour, J.-L., Risi, C., Worden, J., Clerbaux, C., & Coheur, P.-F. (2018). Importance of depth and intensity of convection on the isotopic composition of water vapor as seen from IASI and TES δ D observations. *Earth and Planetary Science Letters*, 481, 387–394. https://doi.org/10.1016/j.epsl.2017.10.048

Laing, A. G., & Fritsch, J. M. (1993). Mesoscale convective complexes in Africa. *Monthly Weather Review*, *121*(8), 2254-2263. https://doi.org/10.1175/1520-0493(1993)121<2254:MCCIA>2.0.CO;2

Landerer, F. W., Dickey, J. O., & Güntner, A. (2010). Terrestrial water budget of the Eurasian pan-Arctic from GRACE satellite measurements during 2003–2009, J. Geophys. Res., 115, D23115. https://doi.org/10.1029/2010JD014584.

Landerer, F. W., Flechtner, F. M., Save, H., Webb, F. H., Bandikova, T., Bertiger, W. I., et al. (2020). Extending the global mass change data record: GRACE Follow-On instrument and science data performance. Geophysical Research Letters, 47, e2020GL088306. https://doi.org/10.1029/2020GL088306

Landerer, F. W., & Swenson, S. C. (2012). Accuracy of scaled GRACE terrestrial water storage estimates. Water Resour. Res., 48, W04531. 10.1029/2011WR011453.

Laraque, A., Bellanger, M., Adèle, G., Guebanda, S. Gulemvuga, G., Pandi, A., et al. (2013a). Recent evolution of Congo, Oubangui and Sangha rivers flows. Académie Royale des Sciences de Belgique. Geogr. Ecol. Trop., 37(1), 93–100.

Lau, K. M., & Chan, P. H. (1983). Short-term climate variability and atmospheric teleconnections from satellite-observed outgoing longwave radiation. Part I: Simultaneous relationships. Journal of the atmospheric sciences, 40(12), 2735-2750. https://doi.org/10.1175/1520-0469(1983)040<2735:STCVAA>2.0.CO;2

Lavaysse, C., Flamant, C., Janicot, S., Parker, D. J., Lafore, J. P., Sultan, B., & Pelon, J. (2009). Seasonal evolution of the West African heat low: a climatological perspective. Climate Dynamics, *33*, 313-330. https://doi.org/10.1007/s00382-009-0553-4.

Lee, H., Beighley, R. E., Alsdorf, D., Jung, H. C., Shum, C. K., Duan, J., et al. (2011). Characterization of terrestrial water dynamics in the Congo Basin using GRACE and satellite radar altimetry. Remote Sens. Environ., 115, 3530 - 3538. https://doi.org/10.1016/j.rse.2011.08.015.

Lehner, B., Verdin, K., & Jarvis, A. (2008). New global hydrography derived from spaceborne elevation data. Eos Trans. Am Gesphys. Union, 89, 93 95. https://doi.org/10.1029/2008EO100001.

Levin, N. E., Zipser, E. J., & Ceding, T. E. (2009). Isotopic composition of waters from Ethiopia and Kenya: Insights into moisture sources for eastern Africa. *Journal of Geophysical Research*, 114(23). https://doi.org/10.1029/2009JD012166

Li, W., & Fu, R. (2004). Transition of the large-scale atmospheric and land surface conditions from the dry to the wet season over Amazonia as diagnosed by the ECMWF re-analysis. Journal of Climate, 17(13), 2637-2651. https://doi.org/10.1175/1520-0442(2004)017<2637:TOTLAA>2.0.CO;2

Li, W., & Fu, R. (2006). Influence of cold air intrusions on the wet season onset over Amazonia. Journal of climate, 19(2), 257-275. https://doi.org/10.1175/JCLI3614.1

Li, W., Fu, R., & Dickinson, R. E. (2006). Rainfall and its seasonality over the Amazon in the 21st century as assessed by the coupled models for the IPCC AR4. Journal of Geophysical Research: Atmospheres, 111(D2). https://doi.org/10.1029/2005JD006355

Liu, Z., Cheng, L., Zhou, G., Chen, X., Lin, K., Zhang, W., ... & Zhou, P. (2020). Global response of evapotranspiration ratio to climate conditions and watershed characteristics in a changing environment. Journal of Geophysical Research: Atmospheres, 125(7), e2020JD032371. https://doi.org/10.1029/2020JD032371

Loomis, B.D., Luthcke, S.B. & Sabaka, T.J. (2019) Regularization and error characterization of GRACE mascons. J Geod 93, 1381–1398. https://doi.org/10.1007/s00190-019-01252-y.

Longandjo, G. N. T., and Rouault, M. (2020). "On the Structure of the Regional-Scale Circulation over Central Africa: Seasonal Evolution, Variability, and Mechanisms". Journal of Climate 33.1, 145-162. https://doi.org/10.1175/JCLI-D-19-0176.1

Longandjo, G. N. T., & Rouault, M. (2023). Revisiting the Seasonal Cycle of Rainfall over Central Africa. Journal of Climate. https://doi.org/10.1175/JCLI-D-23-0281.1

Mahé, G. (1995). Modulation annuelle et fluctuations interannuelles des précipitations sur le bassin versant du Congo. Colloques et séminaires-Institut français de recherche scientifique pour le développement en coopération, 13-26. http://pascal-francis.inist.fr/vibad/index.php?action=getRecordDetail&idt=6313630

Majoube, M. (1971). Fractionnement en oxygène 18 et en deutérium entre l'eau et sa vapeur. *Journal de Chimie Physique*, 68, 1423–1436. https://doi.org/10.1051/jcp/1971681423

Martens, B., Miralles, D. G., Lievens, H., van der Schalie, R., de Jeu, R. A. M., Fernández-Prieto, D., et al. (2017). GLEAM v3: satellite-based land evaporation and root-zone soil moisture. Geosci. Model Dev., 10, 1903–1925. https://doi.org/10.5194/gmd-10-1903-2017.

Mayer, A. L., & Khalyani, A. H. (2011). Grass trumps trees with fire. *Science*, 334, 188–189. https://doi.org/10.1126/science.1213908

Mba, W.P., Vondou, D.A. & Kamsu-Tamo, P.H. (2022). Central African Climate. In Congo Basin Hydrology, Climate, and Biogeochemistry (eds R.M. Tshimanga, G.D.M. N'kaya and D. Alsdorf). https://doi.org/10.1002/9781119657002.ch2.

Meyer, K., Platnick, S., & Zhang, Z. (2015). Simultaneously inferring above-cloud absorbing aerosol optical thickness and underlying liquid phase cloud optical and microphysical properties

using MODIS. Journal of Geophysical Research: Atmospheres, 120(11), 5524-5547. https://doi.org/10.1002/2015JD023128

Miralles, D. G., De Jeu, R. A. M., Gash, J. H., Holmes, T. R. H., & Dolman, A. J. (2011). Magnitude and variability of land evaporation and its components at the global scale. Hydrol. Earth Syst. Sci., 15, 967–981. https://doi.org/10.5194/hess-15-967-2011.

Moihamette, F., Pokam, W. M., Diallo, I., & Washington, R. (2022). Extreme Indian Ocean dipole and rainfall variability over Central Africa. *International Journal of Climatology*, *42*(10), 5255-5272. https://doi.org/10.1002/joc.7531

Molion, L. C. B. (1975). *A climatonomic study of the energy and moisture fluxes of the Amazonas Basin with considerations of deforestation effects*. The University Of Wisconsin - Madison thesis.

Moreira, A., Ruhoff, A., Roberti, D., Souza, V., Rocha, H. & Paiva, R. (2019). Assessment of terrestrial water balance using remote sensing data in South America. Journal of Hydrology, 575. 10.1016/j.jhydrol.2019.05.021.

Moore, M., Kuang, Z., & Blossey, P. N. (2014). A moisture budget perspective of the amount effect. *Geophysical Research Letters*, 41(4), 1329–1335. https://doi.org/10.1002/2013GL058302

da Motta Paca, V., Espinoza-Dávalos, G.E., Hessels, T.M.., Moreira, D.M., Comair, G.F., & Bastiaanssen, W.G.M., (2019). The spatial variability of actual evapotranspiration across the Amazon River Basin based on remote sensing products validated with flux towers. Ecol Process, 8, 6. https://doi.org/10.1186/s13717-019-0158-8.

Munday, C., Washington, R., & Hart, N. (2021). African low-level jets and their importance for water vapor transport and rainfall. Geophysical Research Letters, 48(1), e2020GL090999. https://doi.org/10.1029/2020GL090999

Munier, S., & Aires, F. (2018). A new global method of satellite dataset merging and quality characterization constrained by the terrestrial water budget. *Remote Sensing of Environment*, 205, 119–130. https://doi.org/10.1016/j.rse.2017.11.008

Munzimi, Y., Hansen, M.., & Asante, K. (2019). Estimating daily streamflow in the Congo Basin using satellite-derived data and a semi-distributed hydrological model. Hydrological sciences journal, 64, 1472-1487. 10.1080/02626667.2019.1647342.

Murakami, T. (1980). Empirical orthogonal function analysis of satellite-observed outgoing longwave radiation during summer. Monthly Weather Review, 108(2), 205-222. https://doi.org/10.1175/1520-0493(1980)108<0205:EOFAOS>2.0.CO;2

Negrón Juárez, R. I., Li, W., Fu, R., Fernandes, K., & de Oliveira Cardoso, A. (2009). Comparison of Precipitation Datasets over the Tropical South American and African Continents. Journal of Hydrometeorology, 10(1), 289-299. https://doi.org/10.1175/2008JHM1023.1.

Neupane, N. (2016). The Congo Basin zonal overturning circulation. Adv. Atmos. Sci., 33, 767–782, https://doi.org/10.1007/s00376-015-5190-8.

Nicholson, S. E. (2018). The ITCZ and the seasonal cycle over equatorial Africa. *Bulletin of the American Meteorological Society*, 99(2), 337–348. https://doi.org/10.1175/BAMS-D-16-0287.1

Nicholson, S.E. (2022). The Rainfall and Convective Regime over Equatorial Africa, with Emphasis on the Congo Basin. In Congo Basin Hydrology, Climate, and Biogeochemistry (eds R.M. Tshimanga, G.D.M. N'kaya and D. Alsdorf). https://doi.org/10.1002/9781119657002.ch3.

Nicholson, S. E., & Dezfuli, A. K. (2013). The relationship of rainfall variability in western equatorial Africa to the tropical oceans and atmospheric circulation. Part I: The boreal spring. *Journal of Climate*, 26(1), 45–65. https://doi.org/10.1175/JCLI-D-11-00653.1

Nicholson, S. E., & Grist, J. P. (2003). The seasonal evolution of the atmospheric circulation over West Africa and equatorial Africa. Journal of climate, 16(7), 1013-1030. https://doi.org/10.1175/1520-0442(2003)016<1013:TSEOTA>2.0.CO;2

Nicholson, S. E., Kim, J., Ba, M. B., & Lare, A. R. (1997). The mean surface water balance over Africa and its interannual variability. *Journal of Climate*, 10(12), 2981–3002. https://doi.org/10.1175/1520-0442(1997)010<2981:TMSWBO>2.0.CO;2

Nicholson, S.E. & Klotter, D.A. (2021). Assessing the Reliability of Satellite and Reanalysis Estimates of Rainfall in Equatorial Africa. Remote Sens., 13, 3609. https://doi.org/10.3390/rs13183609.

Nicholson, S.E., Klotter, D., Zhou, L., & Hua, W. (2022). Recent rainfall conditions in the Congo Basin. Environmental Research Letters, 17. 10.1088/1748-9326/ac61c4.

Nicholson, S. E., Klotter, D., Dezfuli, A. K., & Zhou, L. (2018b). New rainfall datasets for the Congo Basin and surrounding regions. Journal of Hydrometeorology, 19, 1379– 1396. https://doi.org/10.1175/JHM- D 18- 0015.1

N'kaya, G.D.M., Laraque, A., Paturel, J.-E., Guzanga, G.G., Mahé, G. & Tshimanga, R.M. (2022). A New Look at Hydrology in the Congo Basin, Based on the Study of Multi-Decadal Time Series. In Congo Basin Hydrology, Climate, and Biogeochemistry (eds R.M. Tshimanga, G.D.M. N'kaya and D. Alsdorf). https://doi.org/10.1002/9781119657002.ch8.

Nlend, B., Celle-Jeanton, H., Risi, C., Pohl, B., Huneau, F., Ngo Boum-Nkot, S., et al. (2020). Identification of processes that control the stable isotope composition of rainwater in the humid tropical West-Central Africa. *Journal of Hydrology*, 584, 124650. https://doi.org/10.1016/j.jhydrol.2020.124650

Noone, D. (2012). Pairing measurements of the water vapor isotope ratio with humidity to deduce atmospheric moistening and dehydration in the tropical midtroposphere. *Journal of Climate*, 25(13), 4476–4494. https://doi.org/10.1175/JCLI-D-11-00582.1

Okoola, R. E. (1998). Spatial evolutions of the active convective patterns across the equatorial eastern Africa region during Northern Hemisphere spring season using outgoing longwave radiation records. Meteorology and Atmospheric Physics, 66(1-2), 51-63. https://doi.org/10.1007/BF01030448

O'Loughlin, F. E., Neal, J., Schumann, G. J. P., Beighley, E., & Bates, P. D. (2020). A LISFLOOD-FP hydraulic model of the middle reach of the Congo. Journal of hydrology, *580*, 124203. https://doi.org/10.1016/j.jhydrol.2019.124203

Overland, I., Fossum Sagbakken, H., Isataeva, A., Kolodzinskaia, G., Simpson, N. P., Trisos, C., & Vakulchuk, R. (2022). Funding flows for climate change research on Africa: where do they come from and where do they go?. *Climate and Development*, *14*(8), 705-724. https://doi.org/10.1080/17565529.2021.1976609

Paca, V. H. D. M., Espinoza-Dávalos, G. E., Hessels, T. M., Moreira, D. M., Comair, G. F., & Bastiaanssen, W. G. M. (2019). The spatial variability of actual evapotranspiration across the Amazon River Basin based on remote sensing products validated with flux towers. *Ecological Processes*, 8(1), 1–20. https://doi.org/10.1186/S13717-019-0158-8

Pagano, T. S., Aumann, H. H., Hagan, D. E., & Overoye, K. (2003). Prelaunch and in-flight radiometric calibration of the Atmospheric Infrared Sounder (AIRS). IEEE transactions on geoscience and remote sensing, 41(2), 265-273. 10.1109/TGRS.2002.808324

Pan, S., Pan, N., Tian, H., Friedlingstein, P., Sitch, S., Shi, H., et al. (2020). Evaluation of global terrestrial evapotranspiration using state-of-the-art approaches in remote sensing, machine learning and land surface modeling. *Hydrology and Earth System Sciences*, 24(3), 1485–1509. https://doi.org/10.5194/hess-24-1485-2020

Pokam, W. M., Bain, C. L., Chadwick, R. S., Graham, R., Sonwa, D. J., & Kamga, F. M. (2014). Identification of processes driving low-level westerlies in West Equatorial Africa. *Journal of Climate*, 27(11), 4245–4262. https://doi.org/10.1175/JCLI-D-13-00490.1

Pokam, W. M., Djiotang, L. A. T., & Mkankam, F. K. (2012). Atmospheric water vapor transport and recycling in Equatorial Central Africa through NCEP/NCAR reanalysis data. *Climate Dynamics*, 38(9–10), 1715–1729. https://doi.org/10.1007/s00382-011-1242-7

Randerson, J.T., G.R. van der Werf, L. Giglio, G.J. Collatz, and P.S. Kasibhatla. (2018). Global Fire Emissions Database, Version 4.1 (GFEDv4). ORNL DAAC, Oak Ridge, Tennessee, USA. https://doi.org/10.3334/ORNLDAAC/1293.

Rauniyar, S. P., Protat, A., & Kanamori, H. (2017). Uncertainties in TRMM-Era multisatellite-based tropical rainfall estimates over the Maritime Continent. *Earth and Space Science*, 4(5), 275–302. https://doi.org/10.1002/2017EA000279

Reager, J. T., Gardner, A. S., Famiglietti, J. S., Wiese, D. N., Eicker, A., & Lo, M. H. (2016). A decade of sea level rise slowed by climate-driven hydrology. *Science*, 351(6274), 699–703. https://doi.org/10.1126/science.aad8386

Rifai, S. W., Li, S., & Malhi, Y. (2019). Coupling of El Niño events and long-term warming leads to pervasive climate extremes in the terrestrial tropics. Environmental Research Letters, 14(10), 105002. 10.1088/1748-9326/ab402f.

Risi, C., Bony, S., Vimeux, F., Frankenberg, C., Noone, D., & Worden, J. (2010). Understanding the Sahelian water budget through the isotopic composition of water vapor and precipitation. *Journal of Geophysical Research*, 115(D24). https://doi.org/10.1029/2010JD014690

Risi, C., Muller, C., & Blossey, P. (2020). What controls the water vapor isotopic composition near the surface of tropical oceans? Results from an analytical model constrained by large-eddy simulations. *Journal of Advances in Modeling Earth Systems*, 12(8). https://doi.org/10.1029/2020MS002106

Risi, C., Noone, D., Frankenberg, C., & Worden, J. (2013). Role of continental recycling in intraseasonal variations of continental moisture as deduced from model simulations and water vapor isotopic measurements. *Water Resources Research*, 49(7), 4136–4156. https://doi.org/10.1002/wrcr.20312

Roberts, G., Wooster, M. J., & Lagoudakis, E. (2009). Annual and diurnal african biomass burning temporal dynamics. Biogeosciences, 6(5), 849-866. https://doi.org/10.5194/bg-6-849-2009

Rodell, M., Famiglietti, J. S., Chen, J., Seneviratne, S. I., Viterbo, P., Holl, S., et al. (2004). Basin scale estimates of evapotranspiration using GRACE and other observations. Geophys. Res. Lett., 31, L20504. 10.1029/2004GL020873.

Rodell, M., Houser, P.R., Jambor, U., Gottschalck, J., Mitchell, K., Meng, C., et al. (2004). The Global Land Data Assimilation System. Bull. Amer. Meteor. Soc., 85, 381-394. 10.1175/BAMS-85-3-381.

Rodell, M., McWilliams, E.B., Famiglietti, J.S., Beaudoing, H.K. & Nigro, J. (2011). Estimating evapotranspiration using an observation based terrestrial water budget. Hydrol. Process., 25: 4082-4092. https://doi.org/10.1002/hyp.8369.

Running, S., Mu, Q., Zhao, M., & Moreno, A. (2021). MODIS/Terra Net Evapotranspiration Gap-Filled Yearly L4 Global 500m SIN Grid V061 [Data set]. NASA EOSDIS Land Processes DAAC. https://doi.org/10.5067/MODIS/MOD16A3GF.061.

Rutan, D. A., S. Kato, D. R. Doelling, F. G. Rose, L. T. Nguyen, T. E. Caldwell, and N. G. Loeb. (2015): CERES synoptic product: Methodology and validation of surface radiant flux. J. Atmos. Oceanic Technol., 32, 1121–1143, doi: 10.1175/JTECH-D-14-00165.1.

Saeed F., Haensler A., Weber T., Hagemann S., & Jacob D. (2013). Representation of Extreme Precipitation Events Leading to Opposite Climate Change Signals over the Congo Basin. Atmosphere, 4(3):254-271. https://doi.org/10.3390/atmos4030254.

Sakumura, C., Bettadpur, S., & Bruinsma, S. (2014). Ensemble prediction and intercomparison analysis of GRACE time-variable gravity field models. Geophys. Res. Lett., 41, 1389–1397. https://doi.org/10.1002/2013GL058632, 2014.

Salati, E., Dall'Olio, A., Matsui, E., & Gat, J. R. (1979). Recycling of water in the Amazon Basin: An isotopic study. *Water Resources Research*, 15(5), 1250–1258. https://doi.org/10.1029/WR015i005p01250

Samba, G., & Nganga, D. (2012). Rainfall variability in Congo-Brazzaville: 1932-2007. *International Journal of Climatology*, 32(6), 854–873. https://doi.org/10.1002/joc.2311

Samuels-Crow, K. E., Galewsky, J., Sharp, Z. D., & Dennis, K. J. (2014). Deuterium excess in subtropical free troposphere water vapor: Continuous measurements from the Chajnantor Plateau, northern Chile. *Geophysical Research Letters*, 41(23), 8652–8659. https://doi.org/10.1002/2014GL062302

Santoso, A., Mcphaden, M. J., & Cai, W. (2017). The defining characteristics of ENSO extremes and the strong 2015/2016 El Niño. Reviews of Geophysics, 55(4), 1079-1129. https://doi.org/10.1002/2017RG000560.

Satyamurty, P., da Costa, C. P. W., & Manzi, A. O. (2013). Moisture source for the Amazon Basin: a study of contrasting years. Theoretical and Applied Climatology, 111, 195-209.https://doi.org/10.1007/s00704-012-0637-7

Save, H., S. Bettadpur, & Tapley, B.D. (2016). High resolution CSR GRACE RL05 mascons. J. Geophys. Res. Solid Earth, 121. 10.1002/2016JB013007.

Save, H. (2020), CSR GRACE and GRACE-FO RL06 Mascon Solutions v02. 10.15781/cgq9-nh24.

Schiro, K. A., Ahmed, F., Giangrande, S. E., & David Neelin, J. (2018). GoAmazon2014/5 campaign points to deep-inflow approach to deep convection across scales. *Proceedings of the National Academy of Sciences of the USA*, 115(18), 4577–4582. https://doi.org/10.1073/pnas.1719842115

Schulz, M., Prospero, J. M., Baker, A. R., Dentener, F., Ickes, L., Liss, P. S., ... & Duce, R. A. (2012). Atmospheric transport and deposition of mineral dust to the ocean: Implications for research needs. Environmental science & technology, 46(19), 10390-10404. https://doi.org/10.1021/es300073u

Sheffield, J., Ferguson, C. R., Troy, T. J., Wood, E. F., & McCabe, M. F. (2009). Closing the terrestrial water budget from satellite remote sensing. Geophys. Res. Lett., 36, L07403. 10.1029/2009GL037338.

Shi, M., Liu, J., Worden, J. R., Bloom, A. A., Wong, S., & Fu, R. (2019). The 2005 Amazon drought legacy effect delayed the 2006 wet season onset. *Geophysical Research Letters*, 46(15), 9082–9090. https://doi.org/10.1029/2019GL083776

Siqueira, J. R., Rossow, W. B., Machado, L. A. T., & Pearl, C. (2005). Structural characteristics of convective systems over South America related to cold-frontal incursions. Monthly weather review, 133(5), 1045-1064. https://doi.org/10.1175/MWR2888.1

Sobel, A. H., Yuter, S. E., Bretherton, C. S., & Kiladis, G. N. (2004). Large-scale meteorology and deep convection during TRMM KWAJEX*. *Monthly Weather Review*, 132(2), 422–444. https://doi.org/10.1175/1520-0493(2004)132<0422:LMADCD>2.0.CO;2

Sohn, B. J., Choi, M. J., & Ryu, J. (2015). Explaining darker deep convective clouds over the western Pacific than over tropical continental convective regions. Atmospheric Measurement Techniques, 8(11), 4573-4585. https://doi.org/10.5194/amt-8-4573-2015

Sonkoué, D., Monkam, D., Fotso-Nguemo, T. C., Yepdo, Z. D., & Vondou, D. A. (2019). Evaluation and projected changes in daily rainfall characteristics over Central Africa based on a multi-model ensemble mean of CMIP5 simulations. *Theoretical and Applied Climatology*, *137*, 2167-2186. https://doi.org/10.1007/s00704-018-2729-5

Sorí, R., Nieto, R., Vicente-Serrano, S. M., Drumond, A., & Gimeno, L. (2017). A Lagrangian perspective of the hydrological cycle in the Congo River basin. *Earth System Dynamics*, 8(3), 653–675. https://doi.org/10.5194/esd-8-653-2017

Sorí, R., Stojanovic, M., Nieto, R., Liberato, M.L. & Gimeno, L. (2022). Spatiotemporal variability of droughts in the Congo River Basin: The role of atmospheric moisture transport. In Congo Basin Hydrology, Climate, and Biogeochemistry (eds R.M. Tshimanga, G.D.M. N'kaya and D. Alsdorf). 10.1002/9781119657002.ch11.

Staal, A., Dekker, S. C., Xu, C., & van Nes, E. H. (2016). Bistability, spatial interaction, and the distribution of tropical forests and Savannas. *Ecosystems*, 19(6), 1080–1091. https://doi.org/10.1007/s10021-016-0011-1

Staal, A., Tuinenburg, O. A., Bosmans, J. H. C., Holmgren, M., Van Nes, E. H., Scheffer, M., et al. (2018). Forest-rainfall cascades buffer against drought across the Amazon. *Nature Climate Change*, 8(6), 539–543. https://doi.org/10.1038/s41558-018-0177-y

Staver, A. C., Archibald, S., & Levin, S. A. (2011). The global extent and determinants of savanna and forest as alternative biome states. *Science*, 334(6053), 230–232. https://doi.org/10.1126/science.1210465

Su, W., T. P. Charlock, and F. G. Rose. (2005): Deriving surface ultraviolet radiation from CERES surface and atmospheric radiation budget: Methodology. J. Geophys. Res., 110(D14209), doi: 10.1029/2005JD005794.

Sun, Q., Miao, C., Duan, Q., Ashouri, H., Sorooshian, S., & Hsu, K.-L. (2018). A review of global precipitation data sets: Data sources, estimation, and intercomparisons. Reviews of Geophysics, 56, 79– 107. https://doi.org/10.1002/2017RG000574.

Suryatmojo, H., Fujimoto, M., Yamakawa, Y., Kosugi, K., & Mizuyama, T. (2013). Water balance changes in the tropical rainforest with intensive forest management system. International Journal of Sustainable Future for Human Security J-SustaiN. 1. 56-62. 10.24910/jsustain/1.2/5662.

Swann, A & Koven, C. (2017). A Direct Estimate of the Seasonal Cycle of Evapotranspiration over the Amazon Basin. Journal of Hydrometeorology, 18. 10.1175/JHM-D-17-0004.1.

Tamoffo, A. T., Moufouma-Okia, W., Dosio, A., James, R., Pokam, W. M., Vondou, D. A., et al. (2019). Process-oriented assessment of RCA4 regional climate model projections over the Congo Basin under 1.5°C and 2°C global warming levels: Influence of regional moisture fluxes. *Climate Dynamics*, 53(3–4), 1911–1935. https://doi.org/10.1007/s00382-019-04751-y

Tao, S., Chave, J., Frison, P.-L., Toan, T. L., Ciais, P., Fang, J., et al. (2022). Increasing and widespread vulnerability of intact tropical rainforests to repeated droughts. Proceedings of the National Academy of Sciences, 119(37), e2116626119. https://doi.org/10.1073/pnas.2116626119.

Taylor, C. M., Fink, A. H., Klein, C., Parker, D. J., Guichard, F., Harris, P. P., & Knapp, K. R. (2018). Earlier seasonal onset of intense mesoscale convective systems in the Congo Basin

since 1999. *Geophysical Research Letters*, 45(24), 13458–13467. https://doi.org/10.1029/2018GL080516

te Wierik, S. A., Cammeraat, E. L., Gupta, J., & Artzy-Randrup, Y. A. (2021). Reviewing the impact of land use and land-use change on moisture recycling and precipitation patterns. Water Resources Research, 57(7), e2020WR029234. https://doi.org/10.1029/2020WR029234

Thorncroft, C. D., Nguyen, H., Zhang, C., & Peyrillé, P. (2011). Annual cycle of the West African monsoon: regional circulations and associated water vapour transport. Quarterly Journal of the Royal Meteorological Society, *137*(654), 129-147. https://doi.org/10.1002/qj.728

Thorne, P. W., & Vose, R. S. (2010). Reanalyses suitable for characterizing long-term trends. *Bulletin of the American Meteorological Society*, 91(3), 353–361. https://doi.org/10.1175/2009bams2858.1

Tierney, J. E., Lewis, S. C., Cook, B. I., LeGrande, A. N., & Schmidt, G. A. (2011). Model, proxy and isotopic perspectives on the East African Humid Period. Earth and Planetary Science Letters, 307(1-2), 103-112. https://doi.org/10.1016/j.epsl.2011.04.038

Tosca, M. G., Diner, D. J., Garay, M. J., & Kalashnikova, O. V. (2015). Human-caused fires limit convection in tropical Africa: First temporal observations and attribution. Geophysical Research Letters, 42(15), 6492-6501. https://doi.org/10.1002/2015GL065063

Tosca, M. G., Randerson, J. T., & Zender, C. S. (2013). Global impact of smoke aerosols from landscape fires on climate and the Hadley circulation. Atmospheric Chemistry and Physics, 13(10), 5227-5241. https://doi.org/10.5194/acp-13-5227-2013

Tremoy, G., Vimeux, F., Soumana, S., Souley, I., Risi, C., Favreau, G., & Oï, M. (2014). Clustering mesoscale convective systems with laser-based water vapor $\delta^{18}O$ monitoring in Niamey (Niger). *Journal of Geophysical Research*, 119(9), 5079–5103. https://doi.org/10.1002/2013JD020968

Trenberth, K. E. (1999). Atmospheric moisture recycling: Role of advection and local evaporation. *Journal of Climate*, 12(5 II), 1368–1381. https://doi.org/10.1175/1520-0442(1999)012<1368:amrroa>2.0.co;2

Tshimanga, R. M., & Hughes, D. A. (2014). Basin-scale performance of a semidistributed rainfall-runoff model for hydrological predictions and water resources assessment of large rivers: The Congo River. Water Resources Research, 50(2), 1174-1188. https://doi.org/10.1002/2013WR014310.

Tummon, F., Solmon, F., Liousse, C., & Tadross, M. (2010). Simulation of the direct and semidirect aerosol effects on the southern Africa regional climate during the biomass burning

season. Journal of Geophysical Research: Atmospheres, 115(D19). https://doi.org/10.1029/2009JD013738

Tyukavina, A., Hansen, M.C., Potapov, P., Parker, D., Okpa, C., Stehman, SV, et al. (2018). Congo Basin forest loss dominated by increasing smallholder clearing. Sci Adv., 4(11):eaat2993. 10.1126/sciadv.aat2993.

Val Martin, M., Kahn, R. A., & Tosca, M. G. (2018). A global analysis of wildfire smoke injection heights derived from space-based multi-angle imaging. Remote Sensing, 10(10), 1609. https://doi.org/10.3390/rs10101609

Vancutsem, C., Achard, F., Pekel, J. F., Vieilledent, G., Carboni, S., Simonetti, D., ... & Nasi, R. (2021). Long-term (1990–2019) monitoring of forest cover changes in the humid tropics. Science Advances, 7(10), eabe1603. 10.1126/sciadv.abe1603

van der Ent, R. J., Savenije, H. H. G., Schaefli, B., & Steele-Dunne, S. C. (2010). Origin and fate of atmospheric moisture over continents. *Water Resources Research*, 46(9). https://doi.org/10.1029/2010WR009127

Verhegghen, A., Mayaux, P., de Wasseige, C., & Defourny, P. (2012). Mapping Congo Basin vegetation types from 300 m and 1 km multi-sensor time series for carbon stocks and forest areas estimation. Biogeosciences, 9(12), 5061-5079. https://doi.org/10.5194/bg-9-5061-2012.

Wahr, J., Swenson, S., & Velicogna, I. (2006). Accuracy of GRACE mass estimates. Geophys. Res. Lett., 33, L06401. https://doi.org/10.1029/2005GL025305.

Wahr, J., Swenson, S., Zlotnicki, V., & Velicogna, I. (2004). Time-variable gravity from GRACE: First results. Geophys. Res. Lett., 31, L11501. 10.1029/2004GL019779.

Wan, Z. (2008). New Refinements and Validation of the MODIS Land-Surface Temperature/Emissivity Products. Remote Sensing of Environment, 140, 59-74. 10.1016/j.rse.2006.06.026.

Washington, R., James, R., Pearce, H., Pokam, W. M., & Moufouma-Okia, W. (2013). Congo basin rainfall climatology: Can we believe the climate models? *Philosophical Transactions of the Royal Society B: Biological Sciences*, 368(1625). https://doi.org/10.1098/rstb.2012.0296

Watkins, M. M., Wiese, D. N., Yuan, D. N., Boening, C., & Landerer, F. W. (2015). Improved methods for observing Earth's time variable mass distribution with GRACE using spherical cap mascons: Improved Gravity Observations from GRACE. Journal of Geophysical Research: Solid Earth, 120. 4. 10.1002/2014JB011547.

Weerasinghe, I., Bastiaanssen, W., Mul, M., Jia, L., & van Griensven, A. (2020). Can we trust remote sensing evapotranspiration products over Africa? Hydrol. Earth Syst. Sci., 24, 1565–1586, https://doi.org/10.5194/hess-24-1565-2020.

Wiese, D.N., Yuan, C., Boening, F. W., Landerer, M. & Watkins, M. (2019). JPL GRACE Mascon Ocean, Ice, and Hydrology Equivalent Water Height RL06 CRI Filtered Version 02. Ver. 02. PO.DAAC, CA, USA. https://doi.org/10.5067/TEMSC-3JC62.

Worden, S., Fu, R., Chakraborty, S., Liu, J., & Worden, J. (2021). Where Does Moisture Come From Over the Congo Basin?. Journal of Geophysical Research: Biogeosciences, 126(8), e2020JG006024. https://doi.org/10.1029/2020JG006024

Worden, J. R., Kulawik, S. S., Fu, D., Payne, V. H., Lipton, A. E., Polonsky, I., et al. (2019). Characterization and evaluation of AIRS-based estimates of the deuterium content of water vapor. Atmospheric Measurement Techniques, 12(4), 2331–2339. https://doi.org/10.5194/amt-12-2331-2019.

Worden, J., Kulawik, S., Frankenberg, C., Payne, V., Bowman, K., Cady-Peirara, K., et al. (2012). Profiles of CH_4, HDO, H_2O, and N_2O with improved lower tropospheric vertical resolution from Aura TES radiances. *Atmospheric Measurement Techniques*, 5(2), 397–411. https://doi.org/10.5194/amt-5-397-2012

Worden, J., Noone, D., Bowman, K., Beer, R., Eldering, A., Fisher, B., et al. (2007). Importance of rain evaporation and continental convection in the tropical water cycle. *Nature*, 445(7127), 528–532. https://doi.org/10.1038/nature05508

Worden, J., Saatchi, S., Keller, M., Bloom, A., Liu, J., Parazoo, N., et al. (2021). Satellite observations of the tropical terrestrial carbon balance and interactions with the water cycle during the 21st century. Reviews of Geophysics, 59, e2020RG000711. https://doi.org/10.1029/2020RG000711.

Wright, J. S., Fu, R., Worden, J. R., Chakraborty, S., Clinton, N. E., Risi, C., et al. (2017). Rainforest-initiated wet season onset over the southern Amazon. *Proceedings of the National Academy of Sciences of the USA*, 114(32), 8481–8486. https://doi.org/10.1073/pnas.1621516114

Xu, D., Agee, E., Wang, J., & Ivanov, V. Y. (2019). Estimation of evapotranspiration of Amazon rainforest using the maximum entropy production method. Geophysical Research Letters, 46, 1402– 1412. https://doi.org/10.1029/2018GL080907

Xu, L., Saatchi, S., Yang, Y., Yu, Y., Pongratz, J., Bloom, A., et al. 2021. Changes in global terrestrial live biomass over the 21st century. Science Advances, 7(27): eabe9829. 18 p. https://doi.org/10.1126/sciadv.abe9829.

Yang, W., Seager, R., Cane, M. A., & Lyon, B. (2015). The annual cycle of East African precipitation. Journal of Climate, 28, 2385–2404. https://doi.org/10.1175/JCLI- D- 14- 00484.1

Yoshimura, K., Oki, T., Ohte, N., & Kanae, S. (2004). Colored moisture analysis estimates of variations in 1998 Asian monsoon water sources. *Journal of the Meteorological Society of Japan*, 82, 1315–1329. https://doi.org/10.2151/jmsj.2004.1315

Zebaze, S., Jain, S., Salunke, P., Shafiq, S., & Mishra, S. K. (2019). Assessment of CMIP5 multimodel mean for the historical climate of Africa. *Atmospheric Science Letters*, *20*(8), e926. https://doi.org/10.1002/asl.926

Zemp, D. C., Schleussner, C.-F., Barbosa, H. M. J., Hirota, M., Montade, V., Sampaio, G., et al. (2017). Self-amplified Amazon forest loss due to vegetation-atmosphere feedbacks. Nature Communications, 8, 14681. https://doi.org/10.1038/ncomms14681.

Zhao, Z., Li, W., Ciais, P., Santoro, M., Cartus, O., Peng, S., et al. (2021). Fire enhances forest degradation within forest edge zones in Africa. Nature Geoscience, 14(7), 479-483. https://doi.org/10.1038/s41561-021-00763-8.

Zhang, Z., Xu, C. Y., El-Tahir, M. E. H., Cao, J., & Singh, V. P. (2012). Spatial and temporal variation of precipitation in Sudan and their possible causes during 1948–2005. *Stochastic environmental research and risk assessment*, *26*, 429-441. https://doi.org/10.1007/s00477-011-0512-6

Zhang, Y., Joiner, J., Alemohammad, S. H., Zhou, S., & Gentine, P. (2018). A global spatially contiguous solar-induced fluorescence (CSIF) dataset using neural networks. Biogeosciences, 15(19), 5779-5800. 10.5194/bg-15-5779-2018.

Zhou, L., Tian, Y., Myneni, R. B., Ciais, P., Saatchi, S., Liu, Y. Y., et al. (2014). Widespread decline of Congo rainforest greenness in the past decade. *Nature*, 508(7498), 86–90. https://doi.org/10.1038/nature13265